X-Ray scattering investigations of subtle ordering in correlated materials

by

Dillon Richard Gardner

B.S. Boston College (2008)

Submitted to the Department of Physics
in partial fulfillment of the requirements for the degree of

Doctor of Philosophy in Physics

at the

MASSACHUSETTS INSTITUTE OF TECHNOLOGY

June 2015

Signature redacted

Author ....
Department of Physics
June 2015

Signature redacted

Certified by....... ....
Young S. Lee
Associate Professor
Thesis Supervisor

Signature redacted

Accepted by ....
Nergis Mavalvala
Associate Department of Physics

X-Ray scattering investigations of subtle ordering in correlated materials

by

Dillon Richard Gardner

Submitted to the Department of Physics
on June 2015, in partial fulfillment of the
requirements for the degree of
Doctor of Philosophy in Physics

Abstract

The interaction of many particles can lead to spectacular new phases of matter whose properties and collective excitations bear little resemblance to the individual particles and interactions. Understanding how the macroscopic state transforms from one phase to another provides key insights into the underlying physics. In this thesis, we study two poorly understood states: the Hidden Order (HO) phase of URu_2Si_2 and the pseudogap of high T_c cuprates.

In the case of URu_2Si_2, the HO phase causes a significant restructuring of the Fermi surface. Thermal conductivity and ultrasound measurements suggest that the lattice degrees of freedom couple strongly to this change. Additionally, torque magnetometry and x-ray diffraction suggest a breaking of C4 rotational symmetry. We directly study the lattice through x-ray scattering. We see no change of the acoustic phonon dispersions or of the phonon lifetimes from the HO transition. Calculations of phonon branch contributions to thermal transport suggest that magnetic excitations are responsible for the increase in thermal conductivity in the HO phase.

For high T_c cuprates, the pseudogap state is not well understood. It is not even clear if it is a true phase transition or if it is a crossover regime. Recent reports of circular dichroism at the copper K-edge in double-layer BSCCO suggest breaking of inversion symmetry in the pseudogap. We perform copper K-edge dichroism measurements on carefully aligned BSCCO. Azimuthal rotations reveal the circular dichroic signal the result of linear bleed through. Polar rotations suggest that the previous reports were likely caused by misalignment.

Thesis Supervisor: Young S. Lee
Title: Associate Professor

Acknowledgments

The work of this thesis couldn't have been accomplished without the help and support of others. I'd like to first thank my adviser, Young Lee, for all his guidance. Young was always engaged with the minutia of the experiments even during midnight phone calls from the beamlines. I am very grateful Young gave me the freedom to explore problems I found of most interest and take full advantage of the wealth of opportunities available at MIT. A final thanks to him for giving me a chance to prove my abilities as a researcher in his group for a year prior to admittance to MIT.

I'd like to thank all of the dedicated research scientists at the National Laboratories: Ayman Said and Bogdan Leu at Sector 30 at APS, Daniel Haskel and Yongseong Choi at Sector 4 at APS, Steve LaMarra and Christie Nelson at X21 at Brookhaven, Hendrik Ohldag at BL13 at SSRL, and all of numerous support staff that make work at the user facilities possible.

Sample growth is a key part of condensed matter research, and a huge thanks to our collaborators.The URu_2Si_2 samples were grown by Graeme Luke and Travis Williams from McMaster. The BSCCO samples were grown by John Tranquada in Brookhaven.

I'd like to thank my fellow graduate students, especially Craig Bonnoit. We shared an office for five years, and Craig introduced me to x-ray scattering and helped me learn how to analyze a lot of the data. Thanks to Robin Chisnell for his cheerful help on the dichroism experiments. I'd also like to thank Harry Han, Joel Helton, Deepak Singh, and Christophe Payen for all the fruitful conversations about these projects.

Thanks to the Boston College physics department. They provided the foundational training needed to get to and get through graduate school. A special thanks to Vidya Madhavan for all of her advice and support over the years. And thanks to Bill Ennis for originally introducing me to the wonders of physics.

Thanks to my friends for all their support and making the last six years fly by. Thanks to the MIT Ultimate community. Joel Brooks, Alisha Schor, Brian Yutko, Axis Sivitz, Brian Munroe, and Matthew Branaham in particular were a huge source

of joy and support. Thanks to my siblings, Cassie and Jared, for being excellent role models and paving the path for me. Thanks to my parents, Mike and Berta, whose love and faith in me habe always been unwavering. Finally, thanks to my partner, Liz Pratt, for all her love and support.

Contents

List of Figures

List of Tables

Chapter 1

Introduction

The interaction of many particles can lead to spectacular new phases of matter whose properties and collective excitations bear little resemblance to the individual particles and interactions. Understanding how the macroscopic state transforms from one phase to another provides key insights into the underlying physics. In the most general case of a phase transition, a high temperature disordered state has a high symmetry, which provides for high entropy to minimize the free energy. Upon lowering the temperature below a critical temperature T_c, the system enters an ordered phase with lower symmetry.

In addition to the broken symmetry, the new phase can be characterized by an order parameter. Along the coexistence line in phase space, by definition, more than one phase can occur in equilibrium. The order parameter is the thermodynamic function that is different between the phases. In the ordered phase, the order parameter has a non-zero correlation function of the order parameter:

$$\lim_{r \to \infty} \langle A^{\dagger}(0) A(r) \rangle \neq 0 \tag{1.1}$$

which is satisfied for $\langle A(r) \rangle \neq 0$

As an example, let's consider the transition from a paramagnetic to ferromagnetic phases. The Hamiltonian for a three dimensional ferromagnetic Heisenberg system can be described with the Hamiltonian:

$$\mathcal{H} = J \sum_{\langle i,j \rangle} \mathbf{S_i} \cdot \mathbf{S_j} \tag{1.2}$$

where $J < 0$ and $\langle i, j \rangle$ denotes nearest-neighbor lattice site pairing. At high temperature, the spin orientations will be pointing in any direction and have $\langle \mathbf{S}(\mathbf{r}) \rangle = 0$ and thus possess three-dimensional rotational symmetry. Above the Curie temperature, T_c regions of the material can have correlations over finite regions and for which $\langle \mathbf{S}(\mathbf{r}) \rangle \neq 0$. Below the T_c, these correlations extend across the entire sample and the spins have a non-zero expectation, $\langle \mathbf{S}(\mathbf{r}) \rangle \neq 0$ and become spontaneously aligned in a specific direction, thereby breaking rotational symmetry. The magnetization, $\mathbf{M} \propto \langle \mathbf{S}(\mathbf{r}) \rangle$ is the order parameter for a ferromagnet.

In condensed matter physics, the interactions between the multiple degrees of freedom in a material lead to a rich array of ordered states. A complete understanding of these states requires understanding broken symmetries and the order parameter. In this thesis, we investigate two unusual states whose complete description remains unknown: the Hidden Order state of $\mathrm{URu_2Si_2}$ and the pseudogap state of the underdoped cuprates.

$\mathrm{URu_2Si_2}$ is a heavy-fermion compound that heavily studied since the foundational work in the mid-1980s. At low temperatures, it undergoes two transitions at $\mathrm{T_0} = 17.5$ K into the Hidden Order (HO) phase, and a superconducting transition at $\mathrm{T}_c =$ 1.4K. Despite three decades of work, the nature of the HO remains a mystery.

Several different experimental have shown strong evidence that the HO phase couples strongly to the lattice. Some diffraction data have shown that for small, extremely clean samples with high RRR, the crystal structure undergoes and orthorhombic distortion in the HO phase.[102] Such a transition breaks C4 rotational symmetry. Thermal conductivity in all crystallographic directions sharply increases upon entering the HO phase. The electronic contributions can be estimated through application of the Wiedemann-Franz law and Hall measurements. This reveals that the charge carriers contribute only a small fraction of the total thermal conductivity. Thus, the change in thermal conductivity is thought to be driven by the lattice. These lattice excitations are phonons, which must then couple strongly to the Hidden Order. [92, 4]

In this work, we attempt to directly measure the affect of the Hidden Order on the lattice. Inelastic scattering is the ideal probe to study bulk excitations. The vast majority of previous scattering work has focused on the magnetic excitations. Previous work on the phonons have been attempted using inelastic neutron scattering, but the magnetic scattering obfuscates the phonon signal. For this reason, inelastic x-ray scattering provide a clean signal of phonon energy and lineshape. This data can then be analyzed to determine directly how the lattice dynamics couple to the HO phase. Additionally, we performed high-resolution diffraction to confirm the reported orthorhombic distortion.

The pseudogap phase of underdoped cuprates has been identified as central piece to the puzzle of high-T_c superconductivity. There has been a long debate about whether or not the pseudogap is a crossover or a distinct phase. A largely overlooked report in 2006 claimed to measure x-ray natural circular dichroism (XNCD) at the copper K-edge in the pseudogap of double layer BSCCO.[54] Such a signal requires the breaking of inversion symmetry, the origin of which has been proposed as an electronic chiral order.[74]

Dichroism is simply a polarization dependent absorption. Circular dichroism has been measured since 1848 when Louis Pasteur showed that a solution of chiral molecules, all with the same handedness, rotate the polarization of linear light. A rotation was seen even when the molecules were randomly oriented. This rotation is due to the fact that the eigenmodes of propagation for chiral molecules are circular light, which have different absorption coefficients depending on handedness.

Circular dichroism is a result of the chirality or angular momentum of the light interacting with the material as both quantities depend on the handedness of the light. When the interaction is dependent upon the angular momentum, this is referred to as Magnetic Circular Dichroism. This effect can be clearly understood in the dipole limit, in which the the electric field is approximately constant over distance of the interaction. For such an interaction, the electric field then rotates in time and is thus the effect is odd under time-reversal symmetry.

Alternatively, the interaction can depend on the chirality of the light, in which case it is dependent upon the rotation of the electric field in space. This effect is called Natural Circular Dichroism and is even under time-reversal symmetry but odd under chiral or inversion symmetry. Such an interaction requires multipole terms beyond the electric dipole term and so in the x-ray regime is significantly weaker than magnetic circular dichroism.

With recent developments in synchrotrons and optics, dichroism measurements with x-rays are now possible. By tuning the energy to an edge of a specific element, absorption is dominated by atomic-like transitions. Because the initial state is a core state, the excitation is localized and element specific. This allows dichroism to be an excellent new bulk probe the local symmetry of specific elements in a crystal.

The rest of this thesis is organized as follows. Chapter 2 provides a more expansive overview into the theories and phenomenology of URu_2Si_2. In Chapter 3, we present our experimental x-ray scattering measurements: diffraction data to measure the crystal structure and inelastic scattering to study the lattice dynamics. Chapter 4 is a more formal discussion of x-ray dichroism with an emphasis on XNCD. In Chapter 5, we present out dichroism study on double layer BSCCO and make general conclusions on sources of error and data misinterpretation of this novel technique.

Chapter 2

The Mysterious Case of URu_2Si_2

2.1 Heavy Fermion Physics

Intermatallic compounds containing $4f$ or $5f$ electron elements display a vast array of interesting and unconventional properties. The starting point for understanding many of these properties is the Kondo lattice model, which expands the Kondo problem of single magnetic impurities to a full lattice. For high temperatures, the f electrons are localized and the system can be thought of as an ordinary metal plus a set of independent localized spins. The magnetic susceptibility follows typical Curie-Weiss behavior. At temperatures below a critical temperature T^*, the f electrons increasingly become delocalized and hybridize with the conduction bands, which quench the local moments. These itinerant electrons form a band with an extremely heavy effective mass and the thermodynamic and transport properties are described by Fermi-liquid theory with heavy quasi-particles. For example, the electronic specific heat coefficient γ is given by

$$\gamma = \frac{2\pi^2 k_B^2}{3} D(\epsilon_F) \tag{2.1}$$

where $D(\epsilon_F)$ is the density of states at the Fermi energy ϵ_F. Because of the heavy band mass, the density of states is typically quite high. Similarly, at low temperatures, the magnetic susceptibility deviates from Curie-Weiss behavior as the f electrons become itinerant. Instead, the susceptibility is dominated by Pauli paramagnetism:

$$\chi_{Pauli} = \mu_B^2 D(\epsilon_F) \tag{2.2}$$

Thus for prototypical heavy fermion materials, the Wilson ratio is still close to unity, as Fermi-liquid theory predicts.

For a single magnetic impurity, the quenched magnetic moment affects resistivity by creating a strong elastic scattering potential, which gives rise to an increasing resistivity at low temperatures and a characteristic resistivity minimum around the temperature at which the quenching occurs. When the same process happens in a heavy fermion material, the strong scattering at each lattice site develops coherence, and the resistivity drops at low-temperatures.

These three affects are hall marks of heavy fermion physics. There are many excellent reviews of the wealth of research in this field, in particular, Piers Coleman's "Heavy Fermions: electrons at the edge of magnetism." [19]

2.2 Thermodynamic properties of URu_2Si_2

The unusual heavy-fermion superconductor was discovered 30 years ago[78, 77, 63]. The crystal is body centered tetragonal, (space group I4/mmm) with lattice constants are $a = 4.1283$ and $c = 9.5742$. The initial work by Palstra et. al reported two transitions in URu_2Si_2 based on peaks in the heat capacity, as shown in Fig. 2-1[77]. The peak at ~1K is a superconducting transition. The second transition at 17.5K into the Hidden Order originally thought to be antiferromagnetic. Later work fit the electronic component of the specific heat to a $C \propto exp(-\delta/k_BT)$ resulted in concluding that a gap of 11meV opened across approximately 40% of Fermi surface below 17.5K.[63]

The magnetic susceptibility is shown in Fig. 2-2. At high temperature, it shows an Ising-like magnetic signal that follows Curie-Weiss behavior until about 150K. The susceptibility is peaked at $\sim$ 60K, which is indicates the coherence temperature for

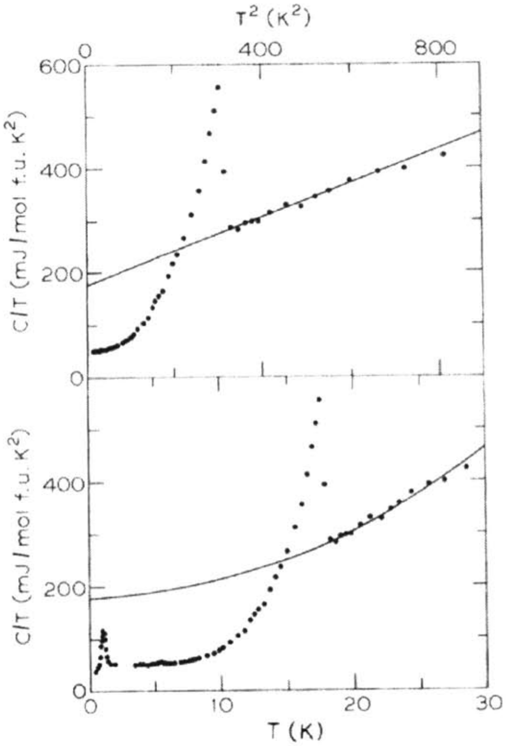

Figure 2-1: Specific heat of URu_2Si_2. The top panel shows C/T versus T^2. The straight line fit's slope gives phonon contribution to C while the intercept extracts γ, the electronic contribution. A high gamma is the signature of heavy fermion physics. In the bottom panel, both the HO and superconducting transitions are apparent as peaks in the specific heat.[77]

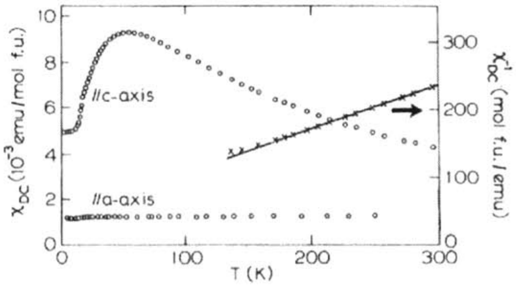

Figure 2-2: Magnetic susceptibility of URu_2Si_2. The linear fit to $1/\chi$ shows Curie-Weiss behavior. Deviations begin around 150K. The anisotropy shows Ising like behavior.[77]

the formation of the heavy Fermi liquid.

2.3 Transport measurements

Resistivity measurements, as shown in Fig. 2-3 show a dramatic downturn around 70K, which is associated with the hybridization of the f electrons of heavy fermion physics. The resistivity then increases at 17.5K followed by a decrease that is well by modeling an energy gap with additional Fermi-liquid behavior. These gaps are estimate to be 90 meV and 68 meV along the c and a axes respectively, which is a rough agreement with specific heat measurements.[78]

Ultrasound measurements show a softening of the C_{11} and the $(C_{11} - C_{12})/2$ modes below ~70K[109]. Comparison with with ultrasound data on $ThRu_2Si_2$ suggest that the $(C_{11} - C_{12})/2$ mode softening is driven by coupling to electronic degrees of freedom.[111] Careful temperature and magnetic field dependencies suggest that this mode couples to electronic changes of the HO phase. This mode is also associated with an orthorhombic strain field and so causes a lattice instability, which is possibly related to symmetry breaking electron band instability due to hybridization of the localized f electrons with the conduction electrons.[113, 110, 112]

Thermal transport measurements show a jump in thermal conductivity in all directions upon entering the HO phase.[4, 92] The electronic contributions to thermal

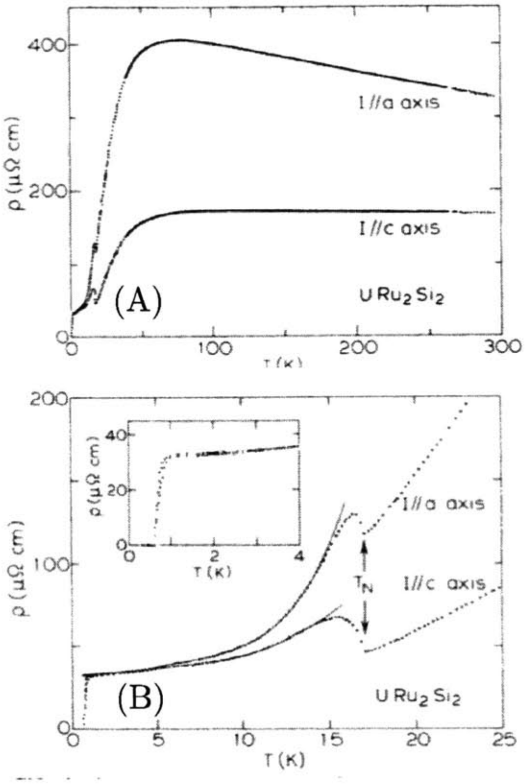

Figure 2-3: Resistivity of URu_2Si_2. The top panel shows a maximum in resistivity around 70K, which is the temperature associated with coherence of the hybridization of the f electrons. At the HO transition, labeled T_N in the lower panel, the jump in resistivity is thought to come from restructuring of the Fermi surface.

conductivity are analyzed via the Hall effect and the application of the Weidemann-Franz law. The HO affect on electronic thermal conductivity consists of two countervailing effects: a reduction of charge carriers due to Fermi surface reconstruction and a drastic decrease in scattering rate. Both of these effects are corroborated through measurements of Nernst and Seebeck coefficients.[5, 84] After accounting for the change in electronic thermal conductivity, there is still significant unexplained increase. Both Behnia et al. and Sharma et al. conclude that this increase is the result of lattice contribution.[4, 92]

2.4 Scattering Experiments

Early neutron scattering measurements show weak antiferromagnetic peaks though they were not long-range ordered[13]. Later experiments showed sample variation of the magnetic moment. Additionally, the entropy forming at T_0, $S = \int_0 (\delta C)/T \mathrm{d}T$ is approximately $0.2 k_B \ln 2$ per formula unit, which if from magnetic ordering, would require a much larger contribution than has ever been seen measured in neutron scattering.

The application of 0.5GPa of pressure leads to an increase of the antiferromagnetic intensity at the $\mathbf{Q_0}$ = (1,0,0). The corresponding ordered moment along the c-axis was $0.4\mu_B$ leading to this phase to be referred to as the Large Moment Antiferromagnet (LMAF) phase.[2]. This ordered phase reduces the symmetry of the cell to simple tetragonal. Follow up Larmour diffraction and careful pressure studies led to the conclusion that measured antiferromagnetic moment in the HO phase is in fact due to puddles of LMAF induced by local stress fields.[73, 10] This is consistent with the sensitivity of sample quality on various measured bulk quantities of the HO phase.[22] It is still unclear whether the measured moment in the HO phase is entirely due to this parasitic moment, or if there is an intrinsic moment. Recently, considerable effort has been devoted to determining a lower bound for an in-plane moment.[23, 87]

Since the initial work, several neutron scattering studies have been performed[13, 105, 106, 104, 49, 107, 85, 9, 12]. Below T_0, there are two distinct gapped longitudinal modes. One with a gap of 1.9 meV is at the commensurate position Q_0 = (0,0,1), which is equivalent to (1,0,0) due to the body centered unit cell. The second gap of 4.5 meV is at the incommensurate position of Q_1 = (1±0.4,0,0). These modes are longitudinal spin fluctuations, unlike traditional antiferromagnetic low-energy spin fluctuation.

Above T_0, the commensurate excitation becomes overdamped and possibly gapless. This is a possible explanation for the large source of entropy change from the HO transition.[106] The incommensurate excitation remains gapped above T_0, but also becomes overdamped.[11]

Significantly less scattering work has been done on phonon excitations. Partly this is due to the difficulty of separating magnetic from lattice scattering mechanisms. There is no evidence of changes to the acoustic branches as a function of temperature though there is perhaps some slight softening of an optic branch. There is no analysis of phonon widths.[15, 11]

2.5 Symmetry breaking

Torque magnetometry measurements have recently been taken as a function of the azimuthal angle ϕ of the in-plane applied magnetic field. For tetragonal crystal symmetry, as well as mirror symmetries present in the $I4/mmm$ space group, $\chi_{aa} = \chi_{bb}$ and $\chi_{ab} = 0$. This mandates that the decomposition of the torque signal should have no contribution that shows less than 4-fold rotational symmetry. However, below T_0, they measured a 2-fold component, which would require a reduction of symmetry including C4 rotational symmetry breaking proposed to be from an electronic nematic order. This has only been seen on some small crystals ($\sim$ 50x50x10μm), possibly due to domains existing in larger samples which provide a signal that averages to zero.[75] Since then, some NMR data have been interpreted to support two-fold anisotropy[50], which has been refuted by other studies.[69]

Most recently, an x-ray diffraction study revealed an orthorhombic lattice distortion. This is seen as the (880) Bragg peak splitting into two different domains. This affect has only been seen on ultra clean samples with RRR ~670.[102] Other studies since on samples with lower RRR have not seen such a distortion.[97]

2.6 Fermi surface measurements

Beyond the indirect evidence of Fermi surface reconstruction, direct measurements through quantum oscillations, ARPES, and STM/STS have been taken. Shubnikov-de Haas measurements as a function of pressure show no significant change when the application of pressure induces a phase transition into the LMAF state. This suggests that the symmetry of the HO state must be reduced to simple tetragonal.[39] This conclusion is also supported by ARPES data which show a heavy band drop below the Fermi surface in the HO state [89] and a restructuring that follows from a folding over Q_0=(001). This also matches DFT calculations of the Fermi surface.[29]

STM/STS show an asymmetric Fano-like lineshape, which is typical for Kondo resonances.[62] They see heavy fermion bands forming well above T_0. Below T_0, STS measures a partial energy gap emerge.[90, 3] Point contact spectroscopy (PCS) measurements, however, see the onset of the gap at higher temperatures (~27 K), suggestive that the STS measurements are dominated by surface physics.[81, 80]

Cyclotron resonance data show an unexpected splitting of the main Fermi surface hole pocket upon rotating the plane of the magnetic field in the plane. This is interpreted as measuring two different domains with mass anisotropy along the (110) and $(1\bar{1}0)$ directions. This is consistent with a nematic Fermi liquid state and the breaking of C4 symmetry.[100, 101]

2.7 Proposed theoretical models

Theory	References
Multipole order	[48, 53, 56, 40, 21]
Incommensurate orbital AFM	[18]
Modulated spin liquid	[83]
Hastatic order	[16, 17, 31]
SDW coupled to induced local moments	[68]
Helicity order	[103]
Chiral density wave	[55]
Hybridization wave	[28]

Table 2.1: List of some proposed theories to explain HO phenomena.

In the 30 years of study, a wide range of theoretical models have been proposed to explain the HO phase. These theories can roughly be divided into those that treat the *f* electrons as localize and those that treat them as itinerant. A whole class of theoretical models lead to higher rank multipole orders. Itinerant theories have proposed numerous unconventional density waves and modulations.

Table 2.1 provides a small subset of the proposed theories to explain the Hidden Order phenomena. Readers who are interested in a more comprehensive background are recommended two excellent review articles by J.A. Mydosh and P.M. Oppeneer.[70, 71]

Chapter 3

Scattering Studies on the Hidden Order Phase of URu_2Si_2

Scattering is an extremely powerful bulk probe. Elastic scattering measures static ordering while inelastic scattering measures excitations. There are numerous excellent references on the details of scattering, though with a stronger focus on neutron scattering.[93, 60, 94]. Here, we present x-ray scattering. Unlike neutrons, which interact with matter via the strong interaction, x-rays interact primarily via the Coulomb force. As a result, atomic structure factor for x-rays is proportional to the number of electrons. Thus, x-ray scattering preferentially sees heavy elements while the neutron scattering cross-section varies in a less systematic way across the periodic table.

In this chapter, we present first elastic scattering measurements on URu_2Si_2 to investigate the crystal structure. Second, we present inelastic scattering measurements of the acoustic phonon excitations.

3.1 Diffraction studies

The crystal symmetry of URu_2Si_2 remains an open question. The high temperature phase is is found to be body centered tetragonal of the $ThCr_2Si_2$ structure (Space Group $I4/mmm$) with $a = 4.1283$ Å and $c = 9.5742$ Å[13] as shown in Fig 3-1 (A).

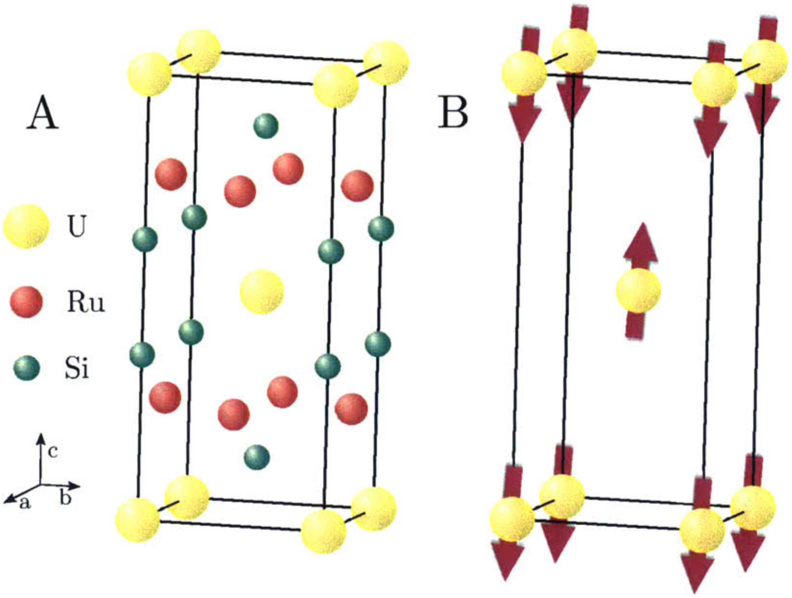

Figure 3-1: Structure of URu_2Si_2. (A) The tetragonal unit cell, with $a = 4.1283$ Å and $c = 9.5742$ Å. (B) The ordering pattern of magnetic movements on the U atoms when in the antiferromagnetic phase.

Under the application of 0.5 GPa, the crystal antiferromagnetically orders, with a moment of $0.4\mu_B$ per Uranium atom. The antiferromagnetic order, shown in Fig 3-1 (B) doubles the primitive cell to a simple tetragonal.

Quantum oscillation measurements show negligible changes upon crossing from the hidden order into the antiferromagnetic phase via application of hydrostatic pressure. This suggest that the electronic structure of the hidden order phase must have the same symmetry as the antiferromagnetic phase[39, 38]. Furthermore, ARPES measurements from show a Fermi surface restructuring that is consistent with a zone folding along $\mathbf{Q_0} = (001)$, which is the antiferromagnetic wave vector[67]. Such a zone folding is necessitated when the symmetry is reduced to simple tetragonal as such a doubling of the unit cell halves the Brillouin zone This makes Q=(001) a good zone center instead of a zone edge. Theoretical calculations of the energy bands match the experimental evidence when modeling the hidden order phase as simple tetragonal[29, 76].

More recently, Okazaki et al. performed torque magentometry measurements to probe χ, the magnetic susceptibility tensor. By applying the magnetic field in the a-b plane and measuring the toque along the c-axis, they measure the in-plane components of the susceptibility. An azimuthal (ϕ) rotation can test the rotational symmetry. Below T_0, the azimuthal dependence includes components that are periodic in 2ϕ, consistent with a non-trivial χ_{ab}. C4 symmetry precludes such a signal, and therefore, Okazaki et al. conclude that the hidden order phase must break C4 symmetry as an "electronic nematic" phase. These results were only seen in small ($\sim$50μm x 50μm x 10μm), which is associated with domain effects[75].

Tonegawa et al. used cyclotron resonance to measure the angle-dependent electron mass of the main Fermi surface sheet. The discovered a splitting of a sharp resonance when the magnetic field is rotated in the a-b plane. They conclude that this splitting is the result of simultaneously measuring two domains, consistent with the nematic picture proposed by Okazaki[100].

Most recently, Tonegawa et al. performed x-ray diffraction. They measure lattice symmetry breaking in which the C4 tetragonal symmetry is reduced to C2 orthorhombic. This was only seen on few samples with high residual resistivity ratio (RRR.) The reasoning for this dependence is unclear[102]. Follow-up diffraction on low RR samples did not see an orthorhombic distortion[97].

Thus it is still unclear the symmetry of the crystal and the electronic structure in the hidden order phase. We attempted to measure the crystal structure via x-ray diffraction to further the investigation into the HO crystal structure.

3.1.1 Details on Orthorhombic distortion

An orthorhombic distortion typically occurs via a small rotation α of one of the tetragonal axis such that $\mathbf{a}_{tet}$ and $\mathbf{b}_{tet}$ are no longer perpendicular. This rotation can occur in four distinct ways, as shown in Fig. 3-2 (A). The new orthorhombic axes can be defined as $\mathbf{a}_{ortho} = \mathbf{a}_{tet} - \mathbf{b}_{tet}$ and $\mathbf{b}_{ortho} = \mathbf{a}_{tet} + \mathbf{b}_{tet}$. These new vectors have length $\sqrt{2}a(1 \pm \frac{\alpha^2}{2})$.

This leads to a doubling of the conventional unit cell. It is important to note, however, that such a distortion does not affect the size of the primitive cell to first order in α and therefore the Brillouin zone. A simple tetragonal cell undergoing such a distortion would become a base-centered orthorhombic cell Bravais lattice. This new unit cell has twice the volume, but also twice the number of lattice points. Similarly, a body-centered tetragonal unit cell under a distortion would have a face-centered orthorhombic cell Bravais lattice. The number of lattice points per cell doubles from two to four. This is distinct from orthorhombic distortions in other systems.

An alternative manner of breaking C4 symmetry would be if the tetragonal axes distorted such that $a_{tet} \neq b_{tet}$. This type of orthorhombic distortion leads to two domain possibilities, shown in Fig. 3-3. This distortion would preserve the mirror symmetry parallel to the a and b axes. Such mirror plane require $\chi_{ab} = 0$, and so this type of distortion is not expected. The resulting diffraction pattern from domains of this type of distortion is distinct from the previous pattern and so a careful diffraction experiment can determine the nature of any distortion. Kernavanois looked for such a distortion and found no evidence for one.[52]

3.1.2 Experimental Method

The diffraction experiment was carried out at the National Synchrotron Light Source at Brookhaven National Laboratory on beamline X21. The characteristics of this diffractometer are shown in Table 3.1.

Energy Range	6 - 16 keV
Monochromater	Si(111) or Ge(111)
Resolution ($\frac{\Delta E}{E}$)	$\sim 2 * 10^{-4}$
Flux	$\sim 2 * 10^{12}$ ph/sec
Spot Size	$\sim$ 1x1 mm^2
Total Angular Acceptance	1 mrad

Table 3.1: X21 Beamline Characteristics

The four-circle diffractometer has a Eularian cradle, as shown in Fig. 3-4, which provides θ, χ, and ϕ angular degrees of freedom. The fourth circle is the 2θ arm, which creates a vertical scattering plane. As the incident x-rays are linearly polarized with **E** horizontal, this creates σ polarized diffraction, which maximizes intensity at

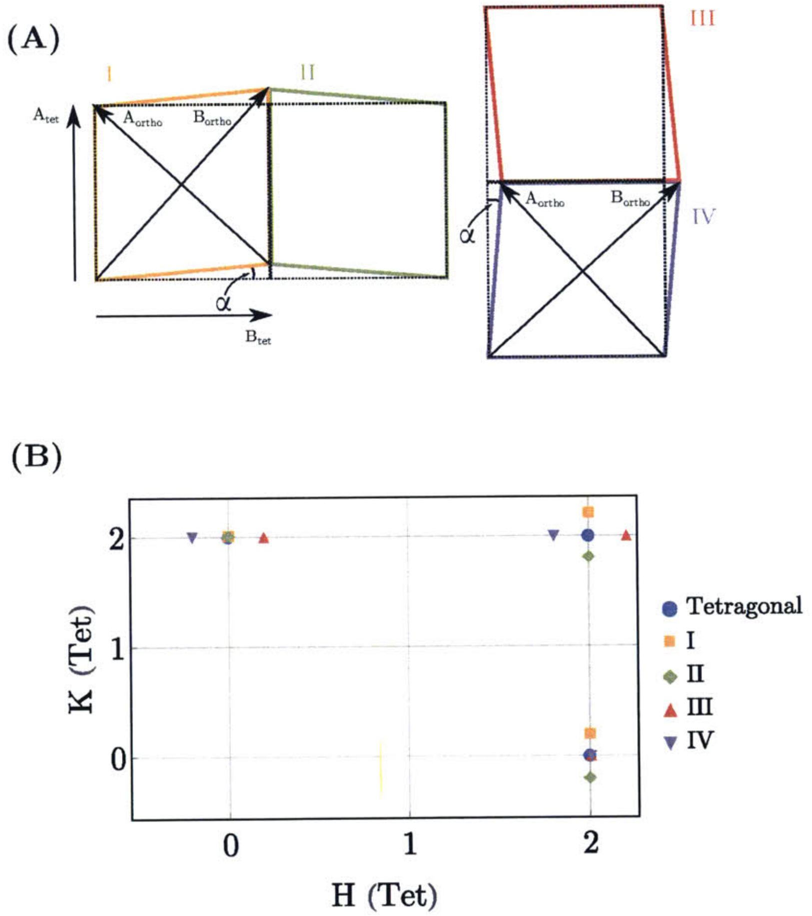

Figure 3-2: An orthorhombic distortion occurring via a rotation of the tetragonal axes. The new orthorhombic unit vectors are $\mathbf{a}_{ortho} = \mathbf{a}_{tet} - \mathbf{b}_{tet}$ and $\mathbf{b}_{ortho} = \mathbf{a}_{tet} + \mathbf{b}_{tet}$. They have length $\sqrt{2}a(1 \pm \frac{\alpha^2}{2})$. (A) The distortion can occur in four distinct ways, leading to possible twining. (B) A reciprocal space map of in plane nuclear Bragg peaks. Each of the four distortion leads to slightly different diffraction pattern.

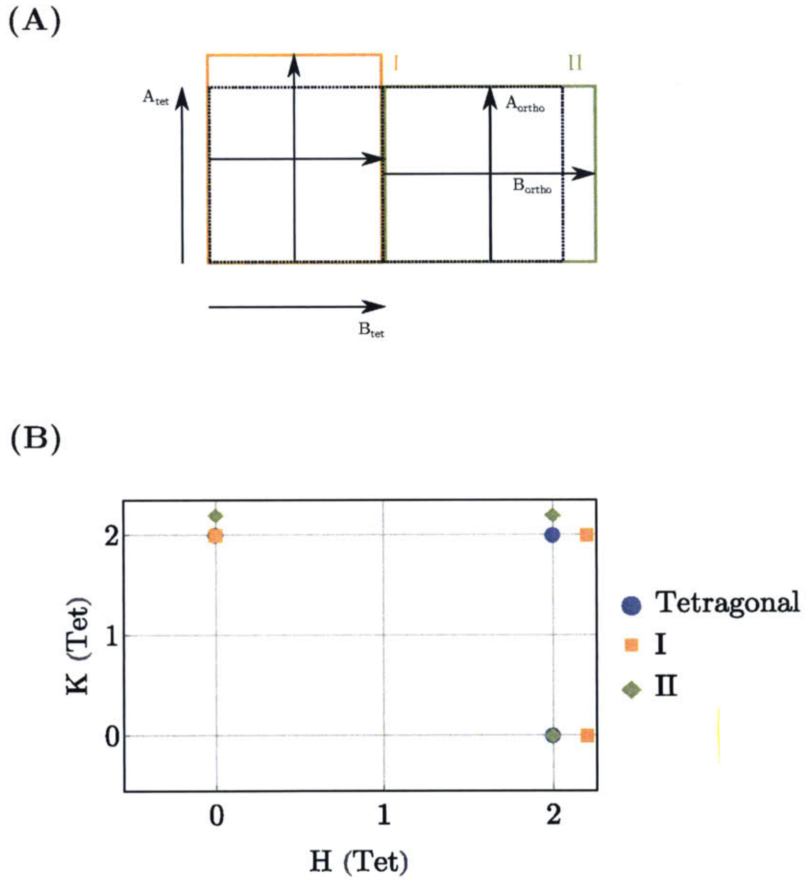

Figure 3-3: An orthorhombic distortion occurring via a stretching/compression of the tetragonal axes. (A) The distortion can occur in two distinct ways, leading to possible twining. (B) A reciprocal space map of in plane nuclear Bragg peaks. Each of the two distortion leads to slightly different diffraction pattern.

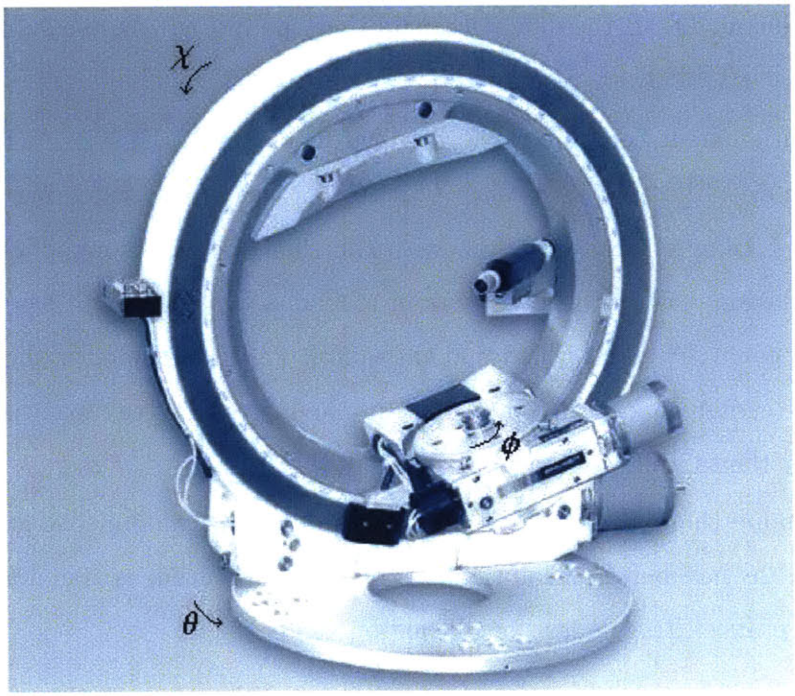

Figure 3-4: Eulerian cradle showing the θ, χ, and ϕ rotational degrees of freedom.

all scattering angles.

Successful diffraction experiments require very precise alignment. To ensure the x-ray beam went through the center of rotation of the goniometer, we mounted a small pin in the Eulerian cradle. Using a specially mounted scope, we manually rotated the χ and ϕ to align the tip of the pin at the center of rotation. We then moved the table vertically to put the center coincident with the beam. This was determined manually using x-ray sensitive photographic paper. We then scanned 2θ motor rotation to determine the zero. Note that the rotations on the Eulerian cradle do not have a uniquely defined zero position.

Diffraction experiments are significantly better in determining differences in the magnitude of $\mathbf{Q}$. This is both from resolution of the diffractometers and quality of sample issues. It is fairly common for crystal samples to have a non-trivial mosaic, which blurs out any small splitting of Bragg peaks from different domains at the same $|\mathbf{Q}|$. Therefore, if the distortion is of the type in Fig. 3-2, (HH0) Bragg peaks will split into different $|\mathbf{Q}|$. If the distortion is of the type in Fig. 3-3, the splitting in $|\mathbf{Q}|$ will be seen at (H00) Bragg peaks.

As we anticipated seeing an orthorhombic distortion of the type in Fig. 3-2, we mounted the crystal in a Displex such that (HHL) was in the scattering plane. The crystal was $\sim$ 1mm x 1mm x 100μm, with the thin direction normal to the c axis. In this orientation, the (00L) peaks were in reflection,while the (HH0) peaks were in transmission geometry. We verified that the sample was in the center of the beam (and therefore the center of rotation) by vertically moving the Displex until photographs revealed that the sample cut the x-ray beam in half.

To determine the optimal design for the experiment, we note that diffraction at higher angle 2θ has better resolution. When the resolution is dominated by the angular acceptance, Bragg's law for diffraction yields:

$$Q = 2k \sin\theta \tag{3.1}$$

$$\Rightarrow \frac{\Delta Q}{Q} = \tan\theta \Delta\theta \tag{3.2}$$

Note that this is the diffraction angle θ, not the rotation angle θ. We therefore want to measure at as high in angle as possible. With $E = 8.58$keV, we could measure the (440) Bragg peak at 163.5 degrees 2θ, which was near the maximum possible in the diffractometer.

To increase our energy resolution, we used a silicon single crystal monochromator. The crystal was polished along the (111) face. Because of geometric constraints of the analyzer 2θ arm, we used the (444) Bragg peak.

All data was collected by scanning the various motors of the diffractometer. Scans of the θ, χ, and ϕ motors probe diffraction at the same $|\mathbf{Q}|$. The χ and ϕ motor rotations change the crystal axes that define the scattering plane. This means that a rotation of these two motors typically does not change the satisfaction of Bragg's Law: if the diffraction condition is satisfied, a rotation of χ and ϕ maintains that diffraction peak. The result, however, will be a diffraction peak at a different position in real space. For this reason, resolution of these motors is determined purely by the geometrics of the diffractometer and is extremely poor.

A the θ rotation moves about $\mathbf{Q}$ within the defined scattering plane. Each Bragg diffraction peak occurs only at a specific location of θ. A scan along θ gives a convolution of the intrinsic resolution of the diffractometer with the mosaic of the crystal. Because of this coupling to the mosaic, such a scan is not the most sensitive to distortions.

A θ-2θ scan measures different values of $|\mathbf{Q}|$ in the same direction in reciprocal space. This results in a convolution of the intrinsic resolution of the diffractometer with the distribution of lattice parameters of the crystal. Because the lattice parameters of a single crystal only varies as the result of strain, the distribution is small. Thus a θ-2θ scan is the most sensitive to a distortion. For a distortion as in Fig. 3-2, a θ-2θ scan at an (HH0) Bragg peak would see peaks from Type I and III orthorhombicity at a different point that Type II and IV.

3.1.3 Data and Analysis

The lattice parameters change slightly as a function of temperature. The HO transition is also associated with a change in lattice parameters. As a result, having correct alignment of the sample changes with temperature.

For this reason, two datasets were collected using two slightly different methods.The first data set includes a realignment at each temperature. This was done by quickly performing a θ-2θ scan and moving the the 2θ value at the maximum intensity. Then we moved the θ motor to the value at the maximum intensity of a quick θ scan. In the second set of data, the alignment done at $T = 22K$ was used for all temperatures. In both datasets, scans were taken first at low temperature and then sequentially raising the temperature of the sample.

The first method provides better alignment for all the data and so should in principle reduce the errors associated with misalignment. The slight rotations between scans, however, can induce slight errors from changes in background scattering and from slightly changing the parts of the sample illuminated by the x-rays. The second set of data reduces these sorts of errors.

The raw data with fits from the first dataset are shown in Fig. 3-5. The second dataset with fits are shown in Fig. 3-6. The error bars are from Poisson counting statistics. In both cases, there are two immediately obvious trends. First, there is a gradual diminishment of the peak intensity as temperature increased. Second, there is a hump-like feature on the right-hand (high-angle) side of the scans that becomes more noticeable at higher temperature.

In order to assess the importance of these trends we fit the data and analyze the fit parameters. The functional form used for the fit the diffraction intensity is

$$\begin{aligned} I(2\theta) = & A_{main}\left(\frac{2w}{\pi(w^2+4(2\theta-2\theta_{max})^2)}\right)+ \\ & A_{small}\left(\frac{2w_{small}}{\pi(w_{small}^2+4(2\theta-2\theta_{small})^2)}\right) \end{aligned} \tag{3.3}$$

The first term is a Lorentzian to fit the primary peak. A Lorentzian is used purely as a phenomenological good fit. The free parameters are A_{main}, w, $2\theta_{max}$ which are the integrated intensity, full width at half maximum, and position of the maximum intensity respectively. The second term is a Lorentzian to fit the intensity from the smaller, hump-like feature. Here, the only free parameter is A_{small}. The parameters w_{small} and $2\theta_{small}$ are fixed for each dataset. They are determined from previous fits with them as free parameters. By reducing the parameter space in this way, the final fits reveal more clearly the information we are after. Namely, any changes to the width of the primary peak, changing intensity to the hump feature, and changing intensity of the primary peak.

The green curve in Figs. 3-5 and 3-6 are the full fit from Eq. 3.3. The red curve is only the first term in Eq. 3.3, which is the primary peak. The gap between these curves provides a visual representation of the amplitude of the hump feature.

The integrated intensity of the main peak is shown in Fig. 3-7 (A). The intensity increases at lower temperature. An orthorhombic distortion should not reduce the total scattering intensity. It is possible that the result of peak splitting from twinning would *reduce* the measured intensity of a single θ-2θ as some of the domains would

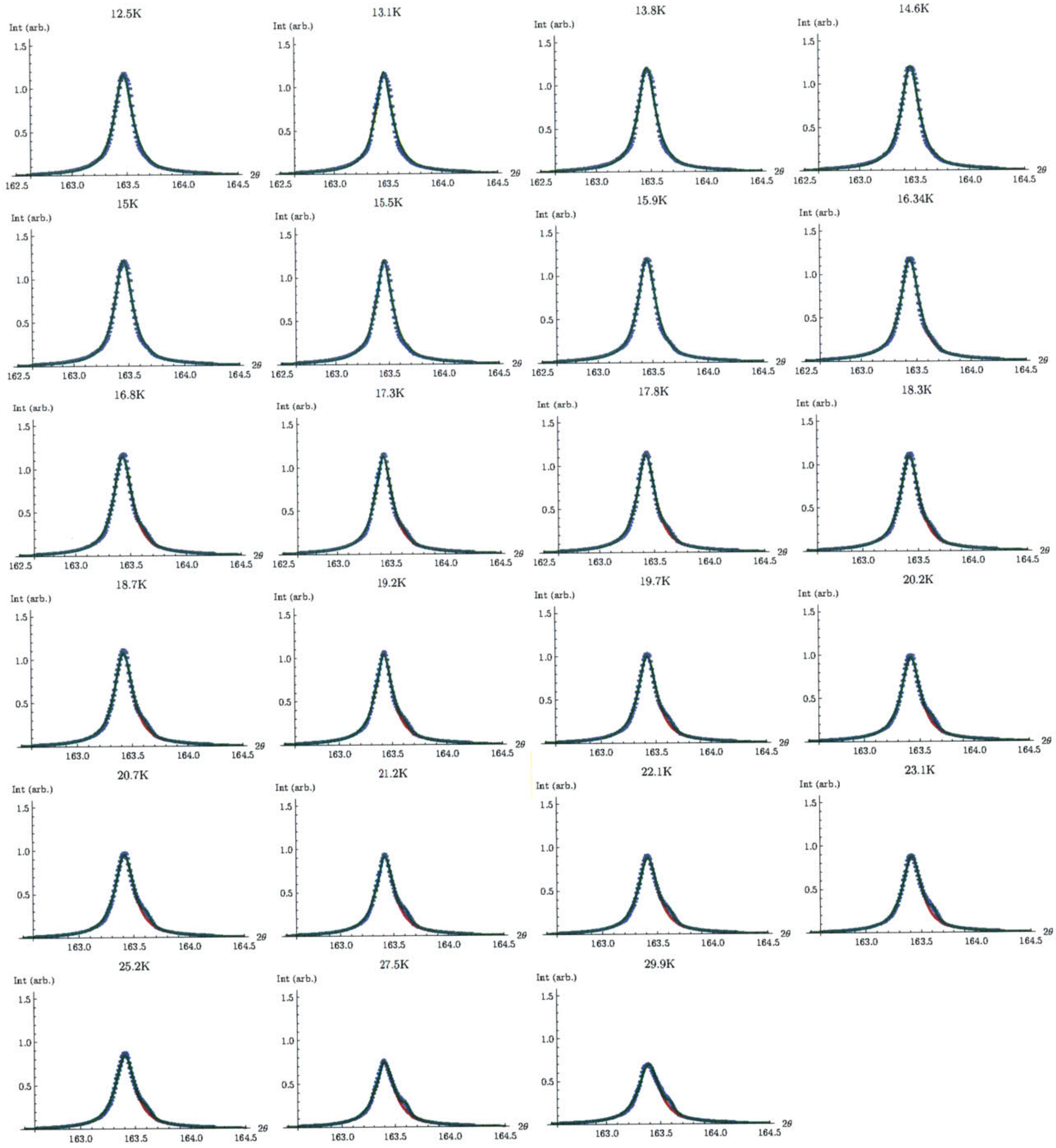

Figure 3-5: θ-2θ diffraction data taken with realignment at each temperature. Fits are discussed in the text

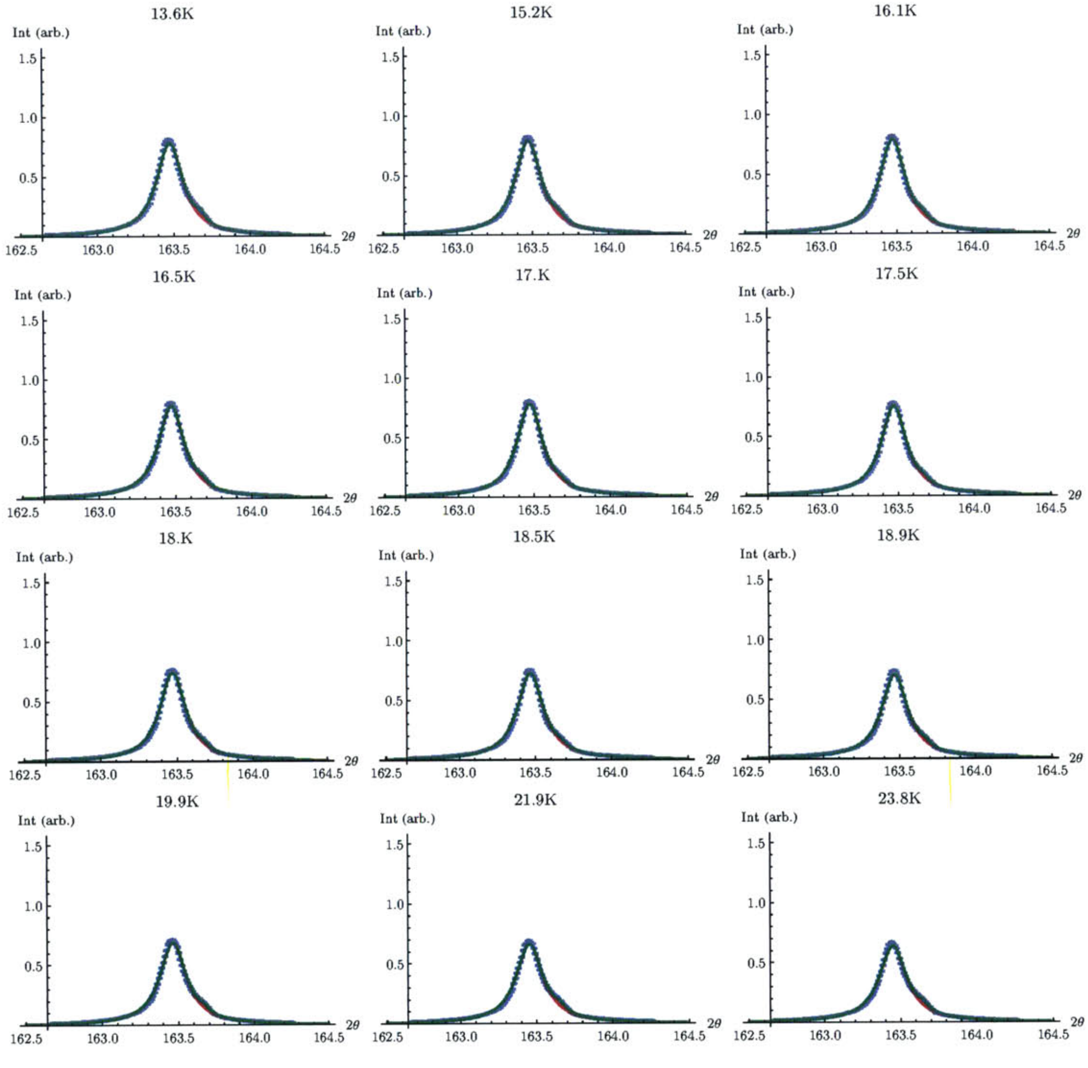

Figure 3-6: θ-2θ diffraction data taken without realignment at each temperature. Fits are discussed in the text

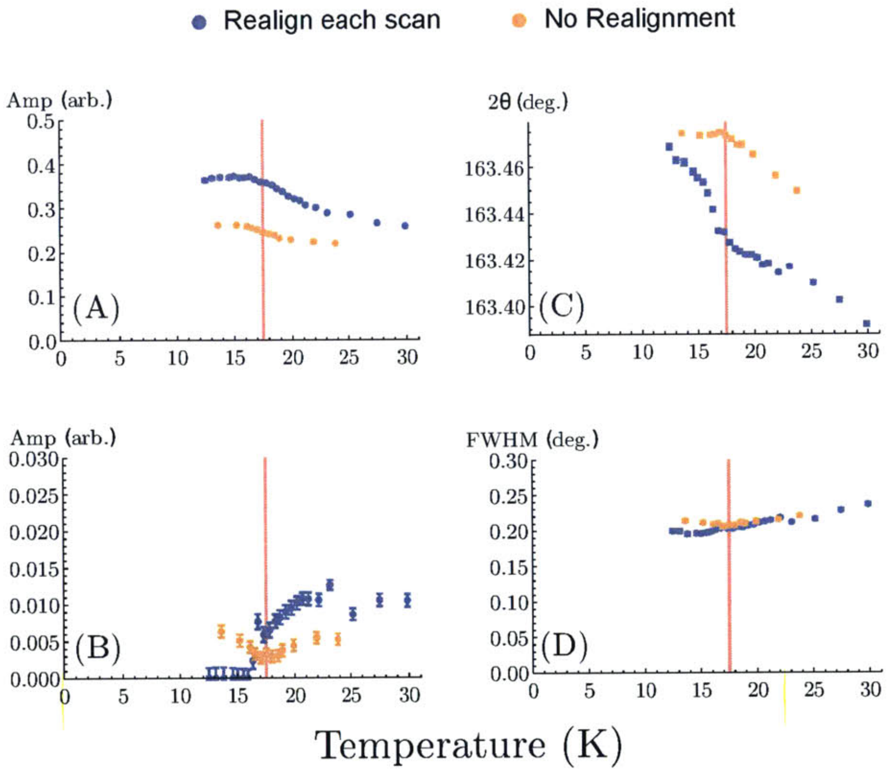

Figure 3-7: Parameters from fits of θ-2θ scans through the (440) Bragg peak to Eq. 3.3 as a function of temperature. (A) A_{main}, the integrated intensity of the main diffraction peak. (B) Integrated intensity of the hump feature. (C) Position of the maximum intensity. (D) Full width at half maximum of the main peak. The red vertical line shows the temperature of the HO transition.

be poorly aligned. This is the opposite of what our data show.

Experimentally, we noticed that the intensity was not particularly reproducible as a function of time. As the experiment went on, returning to the same $\mathbf{Q}$ position could result in different measured intensity. It is our belief that the primary source of changing intensity is not coming intrinsically from the sample, but instead the result of instabilities of the beam line.

The integrated intensity of the small, hump-like peak is shown in Fig. 3-7 (B). In the dataset in which the sample was realigned in each scan, the feature goes almost to zero around the HO transition. That this effect is not seen in the data taken without realignment suggests that this is also not an inherent feature of the HO state. Additionally, the trend of a disappearing peak in the HO phase is also opposite of what would be seen with an orthorhombic distortion.

Fig. 3-7 (C) shows the changing peak maximum. This trend is consistent with changing lattice parameters as a function of temperature. The kink seen right at the HO transition is as expected from thermal expansion[25].

Finally, the FWHM of the primary peak is shown in Fig. 3-7 (D). Under a small orthorhombic distortion, two distinct peaks might not be resolvable. This instead would appear as an increased width. Our data shows no change of the width as a function of temperature.

Tonegawa et al. introduce a dimensionless orthorhombicity parameter $\delta = \frac{b_{ortho}-a_{ortho}}{b_{ortho}+a_{ortho}} = \frac{\sin\theta_1 - \sin\theta_2}{\sin\theta_1 + \sin\theta_2}$, where a_{ortho} and b_{ortho} are the orthorhombic lattice constants and $2\theta_{1,2}$ are the maximum location of two diffraction peaks resulting from twinning. They claim to see an distortion with $\delta \sim 7 * 10^{-5}$.

In order to place bounds on minimal amount of orthorhombicity for which measurements would be sensitive, we note that the data are the convolution between the instrumental resolution and the underlying distribution of lattice parameters. Make the following theee assumption:

1. The orthorhombicity is zero above the hidden order transition

2. All four possible orthorhombic domains are roughly equally populated

The first assumption is necessary to determine the resulting width from the convolution of resolution and lattice parameters. It is well justified if there is any breaking of symmetry upon entering the HO phase. The second assumption is not strictly required, but used in the calculations for ease. Additionally, it is well supported by the toque magnetometry work, which estimates domains to be on the order of $50 \times 50 \times 10\mu$m, which is much less than the beam size of 1x1mm^2[75].

Using these assumptions, we can calculate how orthombic distortions of different sizes should affect our measurements. A distortion of $\delta \sim 6 * 10^{-5}$ should produce an measured FWHM of 0.27, which is significantly more than we ever measured. Thus, we can place an upper bound of any distortion in our measurements at $\delta \sim 6 * 10^{-5}$.

Tonegawa et al. see orthorhombicity only on samples with extremely high residual resistivity ratio (RRR), which is the ratio $\frac{\rho(T=300K)}{\rho(T\rightarrow 0K)}$. Our sample has an RRR of ~ 20, which is significantly worse than the $\sim$ 670 for the sample in which they saw the orthorhombicity and comparable to work in which no distortion was measured.[97] Thus, our work does not contradict previous diffraction.

3.2 Inelastic X-ray scattering

Experimental work on thermal transport and thermal expansion of URu$_2$Si$_2$ suggest that crystal lattice couples strongly to the Hidden Order phase. The majority of previous inelastic scattering data has used neutrons and focused on the magnetic excitations. This work attempts to directly measure the lattice degrees of freedom (phonons). X-rays provide a unique probe in that it is primarily sensitive to the electron cloud in the atomic cores. It is thus strongly sensitive to lattice excitations but not magnetic excitations.

This challenge of taking such measurements with photons is that it require simultaneously the momentum and energy change of ~ 1 Å^{-1} and ~ 1 meV, the orders of magnitude for a phonon. Photons with the requisite momentum are x-rays with energy $\sim$ 10 keV. Thus energy resolution must be $\frac{\Delta E}{E} \sim 10^{-7}$ in order to measure phonon excitations.

3.2.1 Details of the HERIX Spectrometer

These measurements were carried out at Advanced Photon Source (APS) at Argonne National Laboratory. The APS a third generation synchrotron. Electrons are produced from a cathode and accelerated to 450 MeV in a linear accelerator. They then are injected into the booster synchrotron, where electric fields in four radio frequency cavities accelerate the electrons to 7 GeV. These electrons are injected into the storage ring, which is 1104 meters in circumference and has 40 straight sections, referred to as sectors. One of these sectors is used for the injection of electrons. Four are are dedicated to replenishing the energy lost from x-ray emission via 16 radio frequency accelerating cavities. The remaining 35 of these sections are optimized for insertion devices.

Most of the insertion devices are undulatory. These are arrays of permanent magnetics, typically vertically oriented with alternating polarity. As the electron beam passes through, the undulating magnetic field of the array causes the trajectory to oscillate in the horizontal plane. The resulting radiation cones overlap in constructive interference, creating a highly collimated and spectrally narrow x-ray beam.

Our measurements were taken on the HERIX spectrometer at Sector 30. The parameters of this spectrometer are shown in Table 3.2. The critical feature of this spectrometer is the remarkable energy resolution. This is accomplished through a series of monochromators. Each monochromator consists of a pair of crystals, which provide non-dispersive energy selection. In order to achieve the best possible energy resolution, the temperature of each crystal must be tightly controlled in order to obtain as small as possible variation in lattice parameters.

The beam entering the station has a FWHM of 10 keV with an incident flux of $2 * 10^{13}$ photons/sec. The first monochromator is the High Heat Load (HHL) monochromator, which uses the diamond (111) reflection. After leaving the HHL, the beam has a FWHM of $\sim$ 1.6 eV. Because of the intense flux, considerable heat is transferred to these crystals. Diamond is used for its low thermal expansion. The High Heat Load monochromator is water cooled.

Incident Energy	23.7 keV
Energy Resolution	1.5 meV
Momentum Resolution	0.065 Å^{-1}
Energy Transfer Range	-200 - 200 meV
Momentum Transfer Range	0 - 7.5 Å^{-1}
Flux	2*10^{9} photons/sec
Beam Size	35μm$\times$10μm
Number of Detectors	9

Table 3.2: Characteristics of the HERIX spectrometer

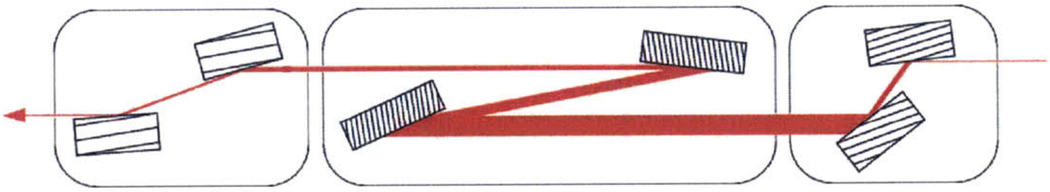

Figure 3-8: Schematic of the high resolution monochromator. Each monochromator crystal is asymmetrically cut. The middle pair does the bulk of the energy discrimination and is carefully maintained at 123K. The other two pairs are at room temperature.

The crown jewel of the monochromation is the high resolution monochromator (HRM), which was designed by Toellner.[98] The HRM consists of three pairs of silicon crystals asymmetrically cut. This is shown schematically in Fig. 3-8. The majority of the energy discrimination is performed by the middle pair. The two monochromatic crystals were formed from opposing surfaces from a cut in a monolithic piece of silicon crystal so they have reciprocal asymmetry parameters. By choosing appropriate asymmetry parameters, the the energy acceptance bandwidth is smaller than the intrinsic bandwidth of the Bragg reflection.

Because slight shifts in temperature affect lattice parameters, the second pair of monochromator crystals must be carefully maintained at 123 K. This is accomplished with a specially designed cryostat in which helium gas is pumped through a heat exchanger immersed in liquid nitrogen. Pulsation dampeners reduce the vibrations from the helium pump.

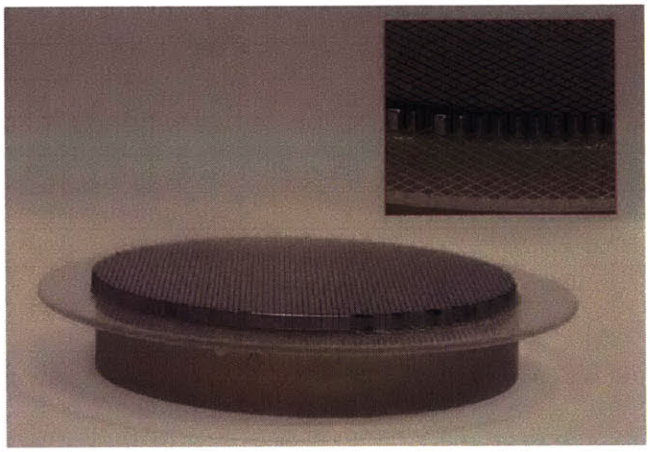

Figure 3-9: Photo of one of the nine analyzers. Each analyzer is curved to increase the angular acceptance. The inset is an enlargement to show an individual pixel. The analyzers are made of silicon and are designed for backscattering of 21.724 keV photons off the (12 12 12) Bragg reflection

High energy resolution from the monochromator is only half of the challenge. The scattered beam travels down a down a nine meter long arm at the end of which are nine analyzers. The analyzers must not only provide excellent energy resolution, but there must also be a wide angular acceptance in order to have sufficient intensity. The analyzer are therefore curved. This required using a two-dimensional bender. The analyzer were designed and made by Ayman Said. An analyzer is shown in Fig. 3-9.

The analyzer is made of silicon. It is designed such that 21.724 keV photons are backscattered of the (12 12 12) Bragg reflection and travel back down the arm to CdTe solid state detectors. The detectors are only 3.5mm below the direct beam. This backscattering approaches the 180 degree limit, which maximizes the energy resolution. A schematic of the whole system is shown in Fig. 3-10.

The spectrometer runs in fixed final energy. Unlike neutron scatter, since the change in energy is so small compared to the energy of the x-rays, there is little distinction in terms of the intensities. Furthermore, since the wave vector also changes by such a small factor over the course of an energy scan, there is no change in the goniometer or 2θ position and no rotation of the resolution function occurs.

One other key experimental difference from neutron spectrometers is that the

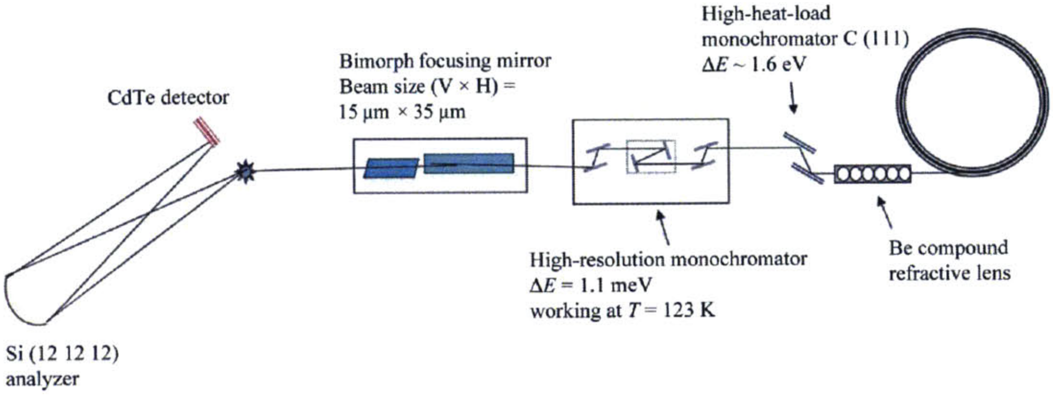

Figure 3-10: Schematic of the HERIX spectrometer (not to scale). The incident energy is controlled by the high resolution monochromator. The distance from the sample to the analyzers is 9090mm. The vertical distance between direct beam and detectors is 3.5mm.

precise nature of the high resolution monochromator does not have an absolute energy definition. Each scan must go through the elastic peak and the zero energy transfer position is determined by fitting. This makes it impossible to take single measurements at precise energies.

Unlike most diffractometers, the scattering plane is horizontal. The x-rays are horizontally polarized, so this results in π polarized scattering (polarization parallel to the scattering plane). This reduces the scattering intensity from σ polarization. But because the experiment is performed at a low value of 2θ, the loss in intensity is small. Certainly much small than the loss due to changing the x-ray polarization. A vertical scattering plane is completely infeasible due to the length of the 2θ arm.

3.2.2 Experimental set-up

Inelastic scattering data were taken over two separate one-week experiments. All the experimental data is from the same URu_2Si_2 single crystal on which the diffraction study was performed. This sample is $\sim$ 1mm x 1mm x 100μm with the thin direction parallel to the c axis.The crystal was mounted attached to a copper post with varnish and placed into a cryostat in a four circle Eulerian goniometer identical to Fig. 3-4.

The sample is sealed inside the cryostat with two beryllium domes. Beryllium is used since the small atomic number leads to a very low electron density and therefore small x-ray scattering cross-section.

The crystal is mounted such that $\chi = 0$, the cryostat is vertical and (H0L) is the scattering plane. A 45 degree rotation of χ puts (HHL) in the scattering plane. Measurements of (H00) and (HH0) Bragg peaks are in transmission. (00L) peaks are in reflection.

APS had concerns about safety from the radiation of the uranium atoms in the sample. To satisfy their concern, we had to create a containment barrier out of Kapton tape. We were unaware of the need for containment until too close to the first experiment start time to design a clever containment. For this reason Kapton was close enough to the center of rotation of the spectrometer to satisfy the geometric scattering conditions. In the second experiment, a better sample holder was designed in which the Kapton was as far away from the center of the spectrometer as possible and still fit within the beryllium dome. A schematic of the sample holders is in Fig. 3-11

3.2.3 Experimental Resolution

For each experiment, the energy resolution was determined by scanning energy through a sample of plexiglass. This provides a different line shape than an energy scan through a Bragg peak. This difference is the result of slight variations in temperature across the analyzer. The changes in temperature result increase in the distribution of final energies accepted by the analyzer. A Bragg peak is nearly a delta-function in **Q** and therefor results in a beam of x-rays incident on only a small part of the analyzer. The elastic scattering from the plexiglass varies only slightly with **Q**, and produces x-rays that illuminate the entire analyzer crystal. This produces a slightly broader peak in an energy scan relative to the Bragg peak. This is shown in Fig. 3-12

When measuring inelastic data, the size of the analyzer corresponds to a breadth of **Q** measured simultaneously. The energy scan through plexiglass is thus the correct measure of energy resolution for inelastic data. This does create a non-trivial

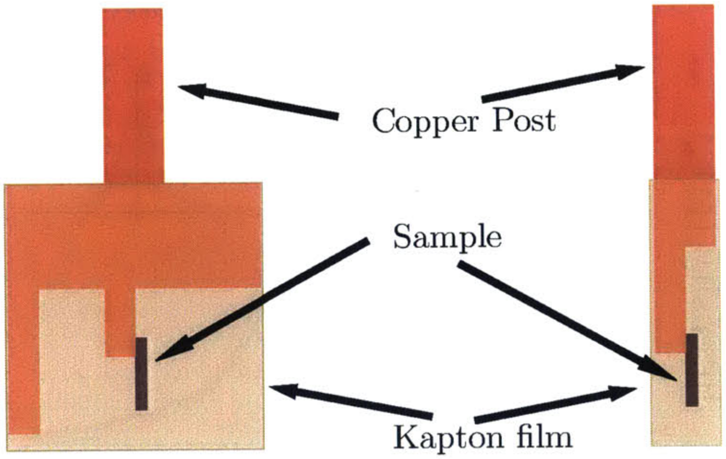

Figure 3-11: Schematic of containment used to satisfy concerns about radiation. We used Kapton tape on our sample holders to meet their requirements. The first experiment used containment as designed on the right. The Kapton tape was close enough to the center of the spectrometer that scattering from the Kapton satisfied geometric requirements to reach the analyzers. The second experiment used the design on the left. Ray tracing showed that the scattering could not satisfy the geometric constraints.

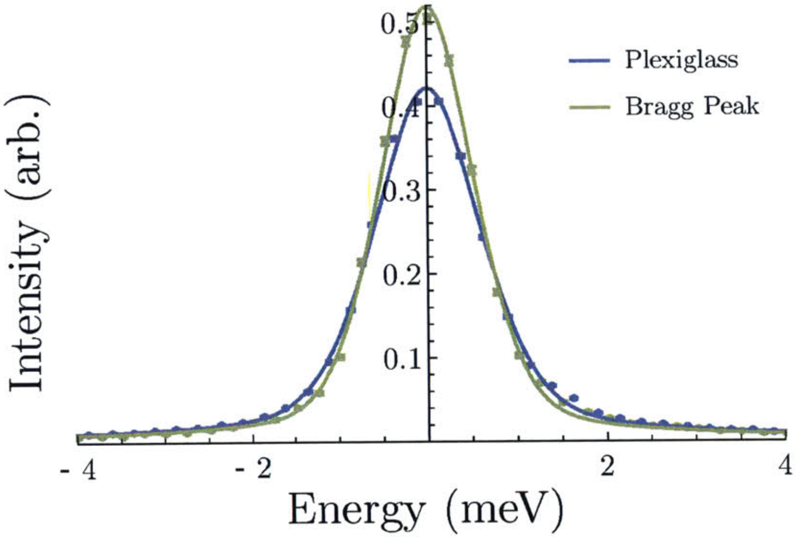

Figure 3-12: Comparison of energy scans through the (220) Bragg peak of URu_2Si_2 and plexiglass. Both scans are fit to a Modified Pseudo-Voigt as described in the text. The Bragg peak is significantly narrow (FWHM ~1.25 meV) than the plexiglass (FWHM ~1.44 meV.) The plexiglass is a better measure of the intrinsic energy resolution of the spectrometer as it includes scattering from the entire analyzer. Data are scaled such that the integrated intensity is equal to unity.

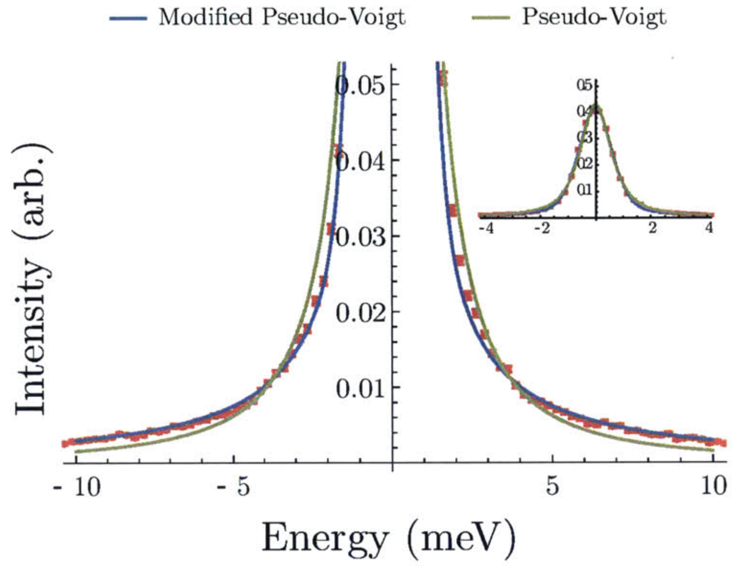

Figure 3-13: Energy scan on plexiglass. Plexiglass provides a better measure of the energy resolution than a scan through the Bragg peak. The lines are fits to a Pseudo-Voigt and a Modified Pseudo-Voigt, as explained in the text. The Modified Pseudo-Voigt provides a better fit of the tails of the resolution function. The inset shows the full intensity. Intensity is scaled such that the integrated intensity of the Modified Pseudo-Voigt line shape is equal to unity.

dependence between the **Q** and energy components of the resolution function. This effect is, however, negligibly small.

When fitting to the energy scan data, we first considered a Pseudo-Voigt, which is a linear combination of a Lorentzian and a Gaussian. This is the line shape commonly used for resolution functions. It is defined as

$$g_{\text{Pseudo-Voigt}}(\omega) = \frac{2\,w\,\eta}{\pi(w^2+4\omega^2)} + \frac{1-\eta}{w}\sqrt{\frac{\ln 2}{\pi}}\,2^{1-\frac{4\omega^2}{w^2}} \tag{3.4}$$

The first term is a Lorentzian and the second is a Gaussian. w is the FWHM and $\eta \in [0,1]$ is the mixing of the two line shapes. This function is normalized such that the integral from $\pm\infty$ is equal to unity.

The Pseudo-Voigt line shape does not well fit the tails of the resolution. For this reason, we introduce a modified Pseudo-Voigt in which the Lorentzian component is raised to the power $^2/_3$

$$
\begin{aligned}
g(\omega) =& \eta \left(\frac{\sqrt{\frac{2\sqrt{2}-1}{\pi}}\,\Gamma\left(\frac{2}{3}\right)}{3\,w^{1/3}\,\Gamma\left(\frac{7}{6}\right)} \right) \left(\frac{w}{w^2 + 4\left(2\sqrt{2}-1\right)x^2} \right)^{2/3} + \\
& \frac{1-\eta}{w}\sqrt{\frac{\ln 2}{\pi}}\,2^{1-\frac{4\omega^2}{w^2}}
\end{aligned}
\tag{3.5}
$$

The first term is the modified Lorentzian. Γ is the gamma function and is needed to ensure that w is still the FWHM and the line shape remains normalized to unity. As shown in Fig. 3-13, this Modified Pseudo-Voigt is a better phenomenological fit to the tail of the resolution as measured on plexiglass.

Because of slight changes in the instrument, the resolution can change slightly over time. In particular, replacing the analyzers has a significant affect on the resolution. For each experimental week, the resolution was measured on plexiglass and fit with the Modified Pseudo-Voigt. We used these fits as the energy component of the resolution function for all data taken during that experimental run.

The **Q** resolution is a result of the divergence of the incident beam combined with the non-zero acceptance angle. The former comes from the convolution of the divergences from the x-rays out of the undulatory and the monochromators. The latter comes primarily from the acceptance angle, determined by the size of the analyzer and the geometric scattering conditions.

We measure the **Q** resolution by scanning along the longitudinal and two transverse directions through each Bragg peak at which we measured phonons. This is done by scanning in **Q**, though such scans are very similar to motor scans. The result of these scans at the (008) Bragg peak are shown in Fig 3-14. Because of how the crystal was aligned, the scan along (0K0) is functionally changing the scattering plane. Thus, the x-rays continue to be Bragg scattered, but in a different direction. Scanning along (H00) is very close to a theta scan and is thus much sharper.

We fit each resolution scan to a pseudo-Voigt. This gives us a model of the momentum components of the resolution function. The resulting FWHM are shown in Table 3.2.3. As discussed later, for phonons measured along a high-symmetry cut,

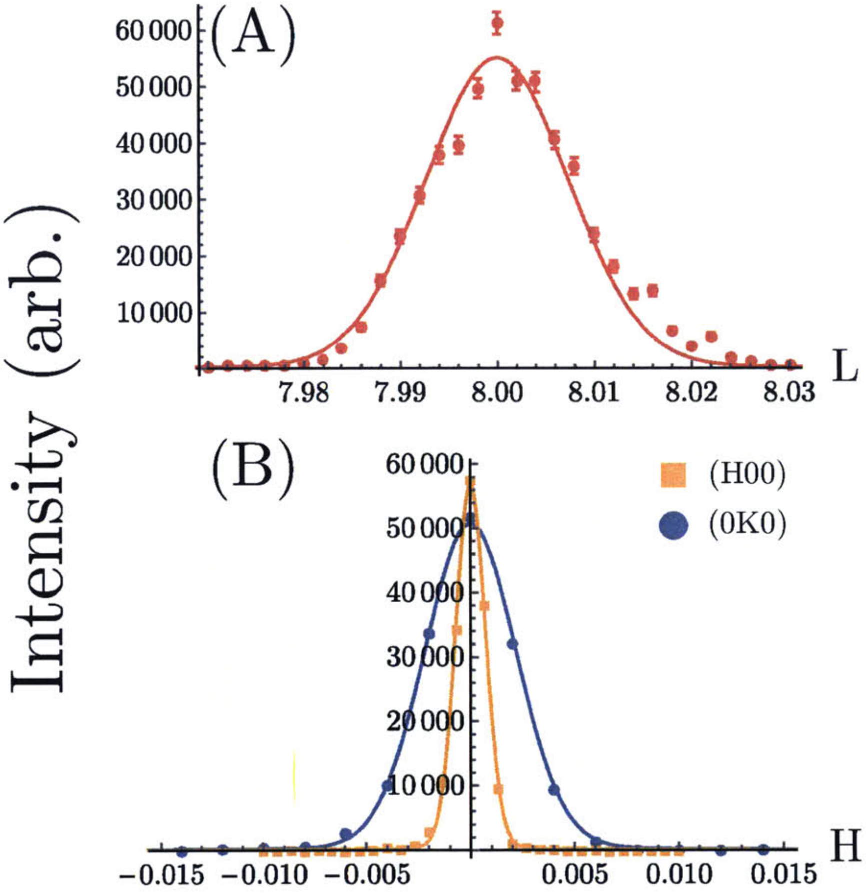

Figure 3-14: **Q** resolution scans measured at the (008) zone center. (A) Scan along (00L). (B) Scans through (H00) and (0K0). Because of how the crystal was aligned, the scan along (0K0) is functionally changing the scattering plane. Thus, the x-rays continue to be Bragg scattered, but in a different direction. Scanning along (H00) is very close to a theta scan and is thus much sharper. All lines are from fits to a pseudo-Voigt

Bragg Peak	Scan Direction	FWHM $Å^{-1}$
(008)	$(00L)$	0.011
(008)	$(H00)$	0.0026
(008)	$(0K0)$	0.0079
(400)	$(H00)$	0.0083
(400)	$(0K0)$	0.013
(400)	$(00L)$	0.0033
(220)	$(HH0)$	0.013
(220)	$(H\bar{H}0)$	0.017
(220)	$(00L)$	0.0025

Table 3.3: FWHM of the **Q** resolution along orthogonal directions at the different zone centers.

the component of the **Q** resolution along the cut direction most strongly affects the measured phonon widths.

3.2.4 Kapton Scattering

Kapton is commonly used in x-ray experimentation. It is a polyimide that is stable across a wide range of temperatures (4 - 673K). It has high mechanical and thermal stability and low outgassing rate, which is necessary for high-vacuum environments. The x-ray cross-section is small and it is relatively insensitive to radiation damage from extended exposure. For these reasons we did not anticipate significant temperature variation in the the scattering from the Kapton film.

This assumption, however, proved incorrect. The initial data showed a very unusual temperature dependence in the elastic ($\hbar\omega = 0$). Additionally, there was significant low-energy quasi-elastic scattering. Because of the temperature dependence and high intensity of the quasi-elastic scattering, we initially interpreted this as coming from the URu_2Si_2.

In the second experiment, we independently measured just Kapton. Data were taken at the same temperature and $|\mathbf{Q}|$ as the majority of the data on URu_2Si_2. As can be seen in the data are shown in Fig. 3-15, there is considerable temperature variation in the inelastic scattering spectra as a function of both $|\mathbf{Q}|$ and temperature.

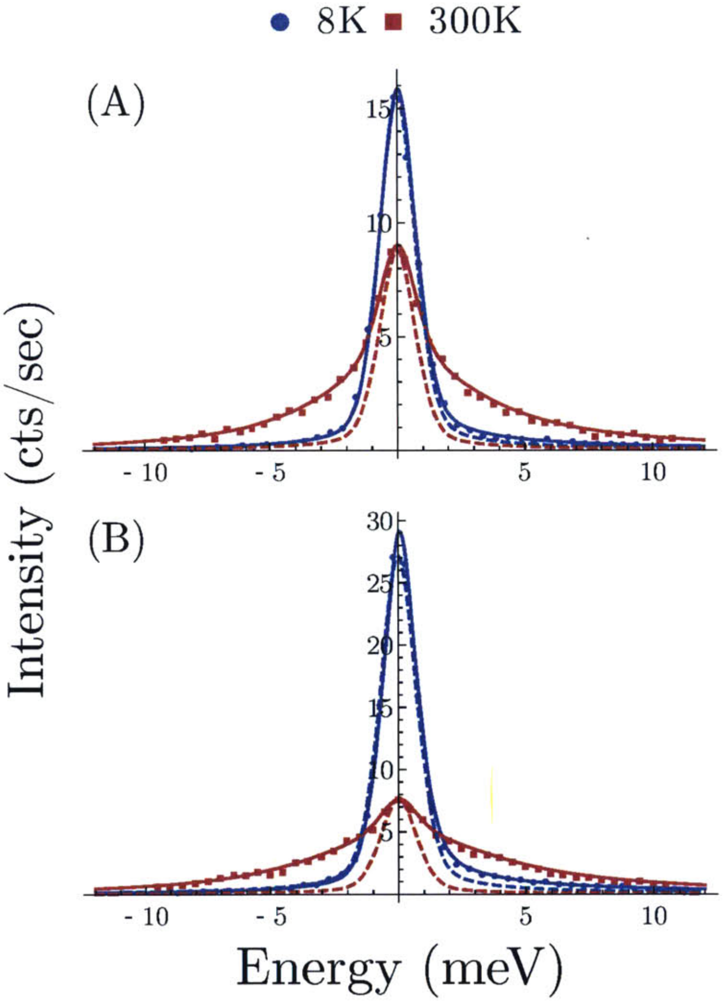

Figure 3-15: Inelastic scattering data from Kapton. (A) Data collected at $|\mathbf{Q}| = 4.3$ Å^{-1}. (B) Data at $|\mathbf{Q}| = 4.3$ Å^{-1}.These are the same $|\mathbf{Q}|$ as the URu$_2$Si$_2$ (220) and (400) Bragg peaks respectively. Solid lines are fits as to Equation 3.6. The dashed line is just the elastic component of the fit.

The data are fit to the to the function

$$I(\mathbf{Q},\omega) = A_{elastic}\, g(\omega) + A_{ODO}\left(\frac{1}{1-e^{-\hbar\omega/k_BT}}\right)\left(\frac{\gamma\,\hbar\omega}{\gamma^2+\hbar\omega^2}\right) \tag{3.6}$$

This function has three free parameters. The first term captures the elastic scattering with only integrated intensity amplitude $A_{elastic}$ as a free parameter. $g(\omega)$ is the energy component of the resolution function measured from plexiglass. The second term is the spectral form resulting from an over damped harmonic oscillator response function. It obeys detailed balance. It has free parameters for the integrated intensity amplitude, $A_{elastic}$, and γ, a measure of the damping.

Fig. 3.6 shows the fit from Eq. 3.6 as a solid line. The dashed line is from a fit to just the resolution function in energy. The gap between the dashed line and the data show the need for the additional term to capture the inelastic scattering from the Kapton tape. The model from Eq. 3.6 well captures this scattering and is used in the analysis of the inelastic scattering data of URu_2Si_2 whenever Kapton scattering is present.

As a final comment about Kapton scattering, we note that there is no data in the literature on extreme temperature of the elastic scattering nor of the strong low-energy inelastic scattering. As high-resolution inelastic x-ray scattering becomes a more common tool, it is important that this source of scattering is either minimized or taken into account to prevent misinterpretation of the signal.

3.2.5 Brillouin Zone Symmetry

Since the scattering cross-section for phonons is proportional to $(\xi\cdot\mathbf{Q})^2$, where ξ is the phonon eigenvector and $\mathbf{Q}$ is the *total* momentum transfer, longitudinal and transverse polarized phonons can be separated along high-symmetry cuts. As discussed in Section 3.1, URu_2Si_2 has body-centered tetragonal symmetry at high temperature. We use this lattice for the scattering experiments. The resulting Brillouin zone is shown in Fig. 3-16

Because of the centering condition, the cell is non-primative. Only points in

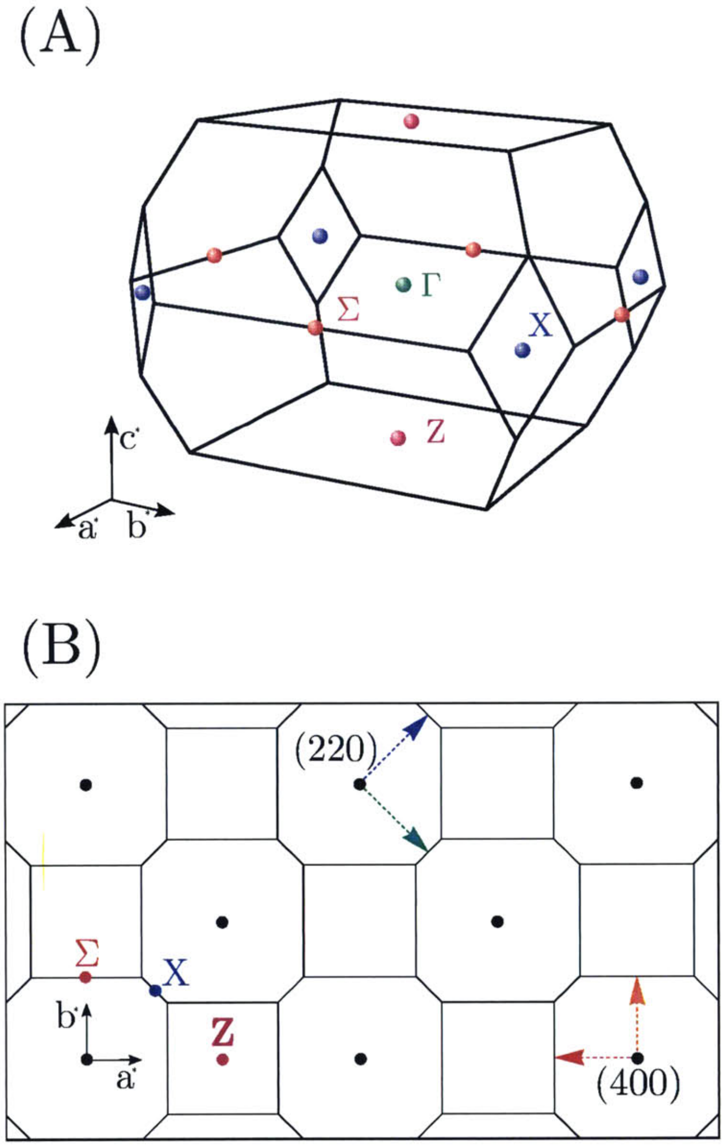

Figure 3-16: (A) The Brillouin zone of URu_2Si_2 assuming a body-centered tetragonal cell. High symmetry points are labeled. (B) A projection of reciprocal space on the (HK0) plane. Structural Bragg peaks are shown in black. (100) is not a zone centered, but rather the *Z* point on the zone edge from the (101) zone center

reciprocal lattice points satisfying $H+K+L = even$ are zone centers. This results in (100) being equivalent to (001) as they are the Z symmetry points from the (000) and (101) zone centers respectively. This is shown in Fig. 3-16(B), which is a projection of reciprocal space onto the (HK0) plane.

Along (ϵ00), the zone boundary is the Σ point at ~(0.6 0 0). This boundary is a edge of two faces, which are defined defined by the equidistances between the zone centers at (000) and either (101) or (10$\bar{1}$). For this reason, Σ depends on the ratio of the crystallographic a and c axes. Along ($\epsilon\epsilon$0), the zone boundary is the X symmetry point, which is the midpoint between (000) and (110). Finally, along (00ϵ), the zone boundary is the Z point, the equidistance between (000) and (002)

Inelastic neutron scattering measures two minima of magnetic excitations. These are commonly referred to as the commensurate and incommensurate excitations. The commensurate excitation is at (100), which is a Z symmetry point. The incommensurate minimum is at (0.6 0 0), which is the Σ point.

The antiferromagnetic phase, which occurs under pressure, reduces the symmetry to simple tetragonal. In this case, all reciprocal lattice points become good zone centers, and the Brillouin zone size is reduced by a factor of 2.

3.2.6 Inelastic scattering fitting procedure

Intensity from a scattering experiment comes from four distinct sources.

1. Elastic scattering. For some scans this includes elastic Kapton scattering. This is $\hbar\omega = 0$ scattering and is resolution limited.

2. Inelastic scattering from Kapton. This was only present during the first experimental run.

3. Phonon scattering. As scans are taken along high-symmetry directions, the three acoustic modes are measured independently. The phonon scattering measured is from the convolution of the resolution with the intrinsic scattering.

4. Background scattering. Unlike neutron scattering, this is extremely small. This

is because there is almost no scattering from the sample holder and different isotopes have the same scattering cross-section. The primary source of background scattering is detector dark counts, which is typically small ($\sim$ 0.01 cts/sec) and therefore negligible. Occasionally, there would be an flat increase in the dark counts from detector charging.

Each scan is then fit to the form

$$\begin{aligned} I(\mathbf{Q},\omega) =& A_{elastic}\, g(\omega) + A_{Kapton}\left(\frac{1}{1-e^{-\hbar\omega/k_BT}}\right)\left(\frac{\gamma\ \hbar\omega}{\gamma^2+\hbar\omega^2}\right) \\ &+ c + I_{phonon} \end{aligned} \tag{3.7}$$

The first term represents the elastic scattering from both the sample and Kapton. $A_{elastic}$ is a free parameter and $g(\omega)$ is the resolution function measured on plexiglass as discussed above. The second term is only present in scans for which the scattering geometry permits the measurement of Kapton scattering. It represents the inelastic Kapton scattering as justified in Section 3.2.4. A_{Kapton} and γ are free parameters. The third term is a constant representing the background. It is typically negligibly small, though in rare cases, the background was elevated due to charging of the detectors.

The final term is the scattering from the phonons. The simplest way to model this scattering is as the response function for a damped harmonic oscillator, which is a Lorentzian

$$I_{phonon} = I_{DHO}(\omega,\omega_0,w) = A_{phonon}\left(\frac{1}{1-e^{-\hbar\omega/k_BT}}\right)\left(\frac{2\omega w}{(\omega^2-\omega_0^2)^2+\omega^2 w^2}\right) \tag{3.8}$$

with free parametersA_{phonon}, the amplitude, $\hbar\omega_0$, the energy of the mode at the measured $\mathbf{Q}$, and w, the width. This form does not take into account the affect of the instrumental resolution, but captures the essential physics of the phonon. It also does not require previous knowledge of the dispersion as a resolution convolved fit does.

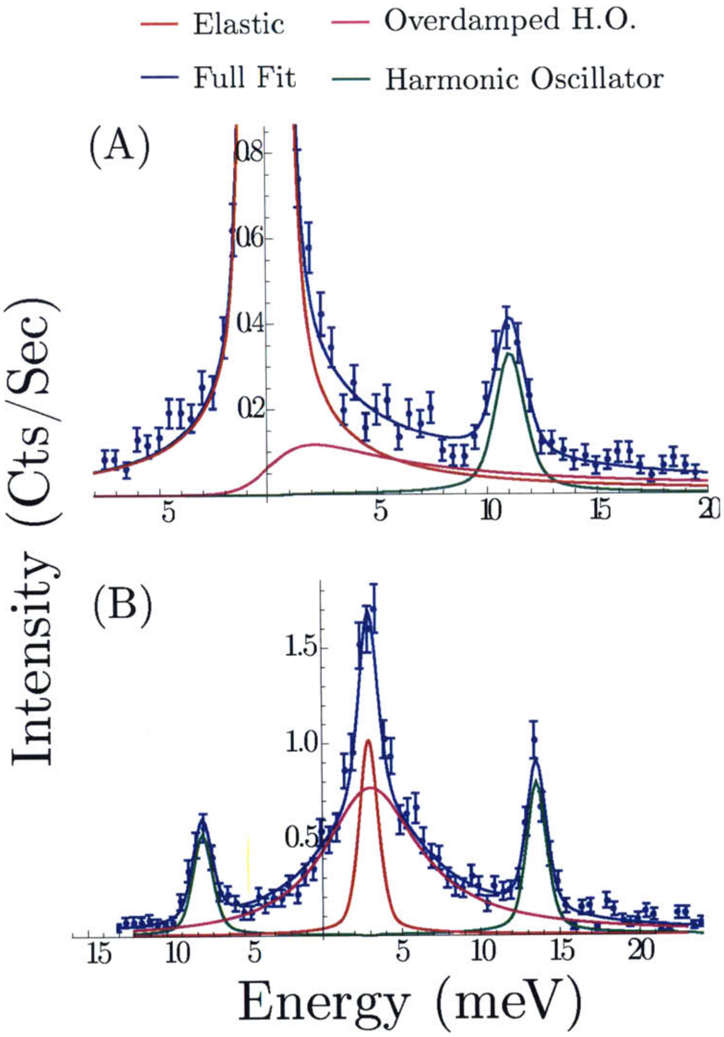

Figure 3-17: Fits showing all of the different terms in the fit function at (A) 8K and (B) 300K for the phonon measured at (3.4 0 0) . This position corresponds to a longitudinal phonon with q=0.6. The blue curve shows the full fit. The red curve is the elastic line. The purple is the over damped oscillator modeling the Kapton scattering. The green curve is the phonon, modeled as a damped harmonic oscillator (Lorentzian) lineshape. There is typically an energy offset that is an effect of the high resolution monochromator.

Figure 3-17 shows the effects of the different components of the fit for the phonon measured at (3.4 0 0). (A) shows the measurement at 8K while (B) shows the measurement at 300K. Due to the scattering cross-section of phonons, the measured phonon is a longitudinally polarized phonon with $q = 0.6$, which corresponds to the zone boundary. This is the location of the incommensurate magnetic excitation seen in neutron scattering.

For each figure, the blue line shows the full fit. The red line just the contribution from the elastic scattering. The pink is the Kapton scattering. And the green is the phonon. Notice that the peak location for the elastic scattering is not centered at $\omega = 0$. This is because the high-resolution monochromator cannot accurately move to a specific energy. It is, however, accurate in scanning through energies. Thus, for each scan, we move from negative energy transfer through positive energy transfer. When fitting, we add an offset parameter. For all subsequent data, we shift the data based on the fit offset so that the elastic peak is at $\omega = 0$.

To extract the more physically relevant phonon lifetime, we can account for the resolution of instrument by fitting to the more complex form:

$$I_{phonon}(\mathbf{Q},\omega) = \int d\tau\, g(\tau)\, b(\lambda)\, A_{phonon} I_{DHO}(\omega, \omega_0(\mathbf{Q}-\lambda), \Gamma) \tag{3.9}$$

The phonon term now includes a convolution. $g(\tau)$ is the measured energy momentum and $b(\lambda)$ are the component of the momentum resolution along the cut direction.I_{DHO} is the functional form for a damped harmonic oscillator given in Eq. 3.8. In order to perform the convolution, fits to just the damp harmonic oscillator response function is used to determine the dispersion.

In principle, the momentum resolution consists of a three dimensional integral. As the modes disperse slowly relative to the FWHM of the q resolution, it is a good approximation to take a series expansion of the mode:

$$\omega(\mathbf{Q}+\epsilon) \approx \omega(\mathbf{Q}) + \mathsf{D}\,\omega(\mathbf{Q}) \cdot \epsilon + \epsilon^{\mathsf{T}}\{\mathsf{D}^2\,\omega(\mathbf{Q})\}\epsilon \tag{3.10}$$

where $\mathsf{D}\,\omega(\mathbf{Q})$ is the gradient and $\mathsf{D}^2\,\omega(\mathbf{Q})$ is the Hessian matrix evaluated at $\mathbf{Q}$. Because all of our data are taken along high symmetry directions, many of these terms are zero. Specifically, in all cuts, the first derivative of the dispersion in all directions orthogonal to the cut are zero. For example, in a cut along $(q00)$, symmetry dictates that $(q\,\epsilon\,0)$ is equal to $(q\,\bar{\epsilon}\,0)$, and $(q\,0\,\epsilon)$ is equal to $(q\,0\,\bar{\epsilon})$. Therefore the gradient is along $(H00)$ and all other terms in the resolution function only contribute to at second order in $\boldsymbol{\epsilon}$. Thus we are well justified to only include the energy and cut direction resolution in our convolution. In fact, the dominant fact is by far the energy convolution. The cut direction momentum resolution convolution is less than 20% the size of the energy resolution convolution.

3.2.7 Inelastic Scattering Results

Figure 3-18 show scans taken at (2+ϵ, 2+ϵ, 0) and (4 -ϵ, 0, 0). This corresponds to measuring the longitudinal dispersion along (ϵ ϵ 0) and (ϵ 0 0). See Figure 3-16 for reference. Data taken at 300K and 8K are shown. The data taken along (4 -ϵ, 0, 0) include scans both with and without the presence of Kapton scattering. All of the data along (2+ϵ, 2+ϵ, 0) have Kapton scattering.

In comparing the 300K and 8K data, there are no measured change in the phonon energies. The phonon intensities diminish, but the fit parameters confirm that this intensity is driven purely by the Bose scaling. At low temperature, the negative energy transfer, which corresponds to measuring phonon annihilation does not measure any phonon excitation, as expected. For this reason the scans were over a smaller energy transfer. At 300K, the difference in intensity at both the negative and positive energy transfer are well fit by the functional form, which obeys detailed balance.

One unexpected feature of the data is the increase in width near the zone center. This effect was seen in the longitudinal modes along all of the high symmetry directions. This effect was temperature independent.

Figure 3-19 shows the result of the fit parameters. It includes fits both with and without accounting for the effect of energy resolution via a convolution. When fitting without an energy convolution, the phonon was modeled simply by the damped

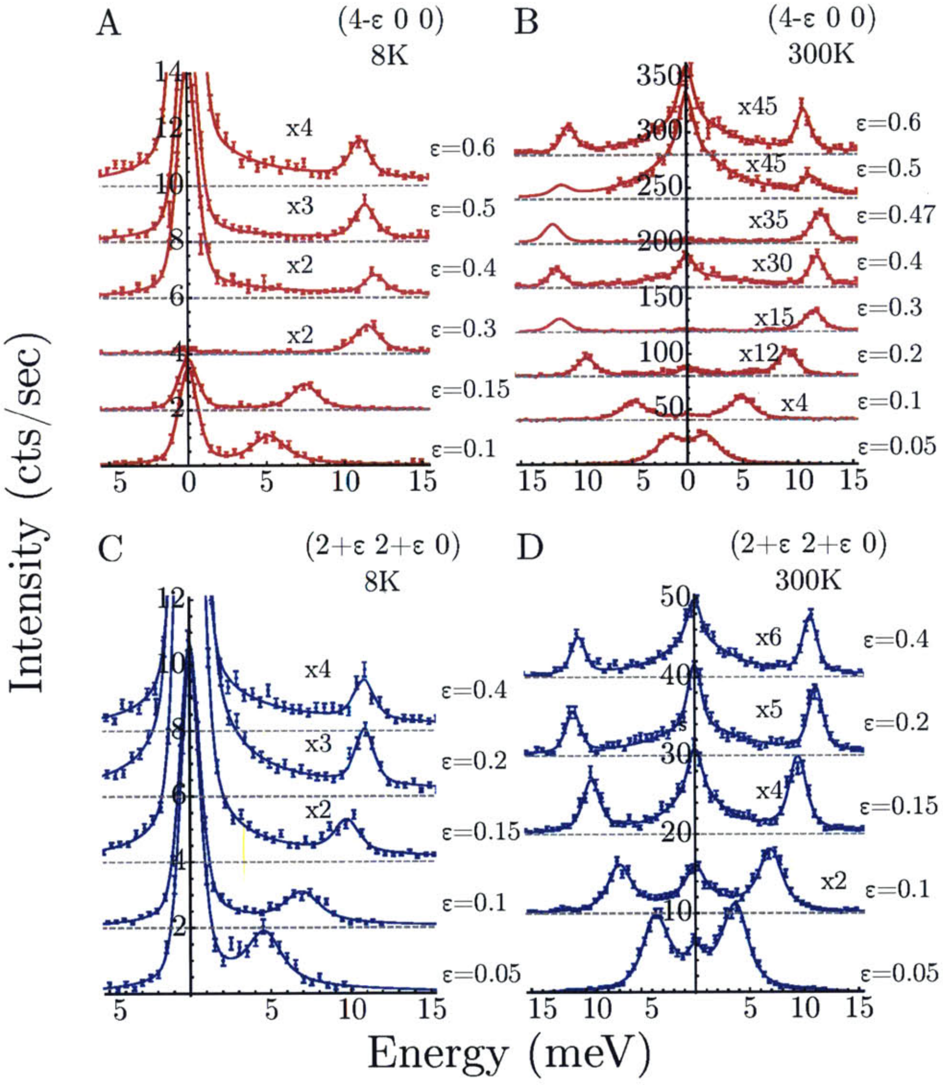

Figure 3-18: Scans of acoustic phonons measured at (4 -ϵ, 0, 0), in (A) and (B), and (2+ϵ, 2+ϵ, 0), in (C), and (D). These modes correspond to longitudinal modes along Γ to Σ and Γ to X respectively. Data are shown at 300K and 8K. Fits are as described in Eq. 3.7 with the phonon modeled as in Eq. 3.8

harmonic oscillator (Lorentzian) line shape. This clearly shows a tendency for the longitudinal modes to increase the measured width and intrinsic line width, Γ, near the zone center. The increased line width comes from a reduced lifetime of the phonon. The origin of the tendency towards increased damping at low **Q** is not well understood, but is interpreted as a coupling to other degrees of freedom. Less data was taken on the transverse modes. Though we do not see any increased width, it is possible the effect exists but is smaller.

Instead of plotting the widths as a function of r.l.u, Fig. 3-20 shows the intrinsic phonon lifetime as a function of mode energy in (A) and |**q**, the norm of the phonon wave vector, in (B). This plot includes all longitudinal acoustic branches with the addition of two transverse modes to show the apparent width dependence. Interestingly, the phonon lifetimes from all branches lie on the same line for both the energy and wave vector, which is in part because the speeds of sound are comparable in all directions.

The commensurate magnetic excitation is a longitudinal mode at $\mathbf{Q_0}$=(001). However, as mentioned previously, there is evidence from Fermi surface measurements that the HO phase is actually simple tetragonal, which makes $\mathbf{Q_0}$ a zone center. In such a case, these magnetic excitations exist at all zone centers, even if the scattering cross-section is small. The phonons near the zone center thus might be able to couple to this degree of freedom. The increased breadth of low **Q** is seen at all temperatures. We note that magnetic scattering at $\mathbf{Q_0}$ is seen above the HO temperature, albeit at lower energy and heavily damped.[9, 11] Thus it is possible the coupling exists at high temperature as well. Alternatively, energy scale for both the phonons that experience broadening and the intrinsic width is close to 2meV. This is the same energy as the commensurate magnetic excitation and of the electronic excitation seen in Raman scattering.[55] Finally, it is possible that the broadening is coming from disorder, though it is unclear why this would preferentially couple to low **Q** modes.

The dispersions are shown in Fig. 3-21. The solid lines are guides to the eye from fits to odd order sine functions. Dashed lines are the speed of sounds calculated from the published elasticity data. For the cuts along Γ to X and Γ to Σ, the lines are

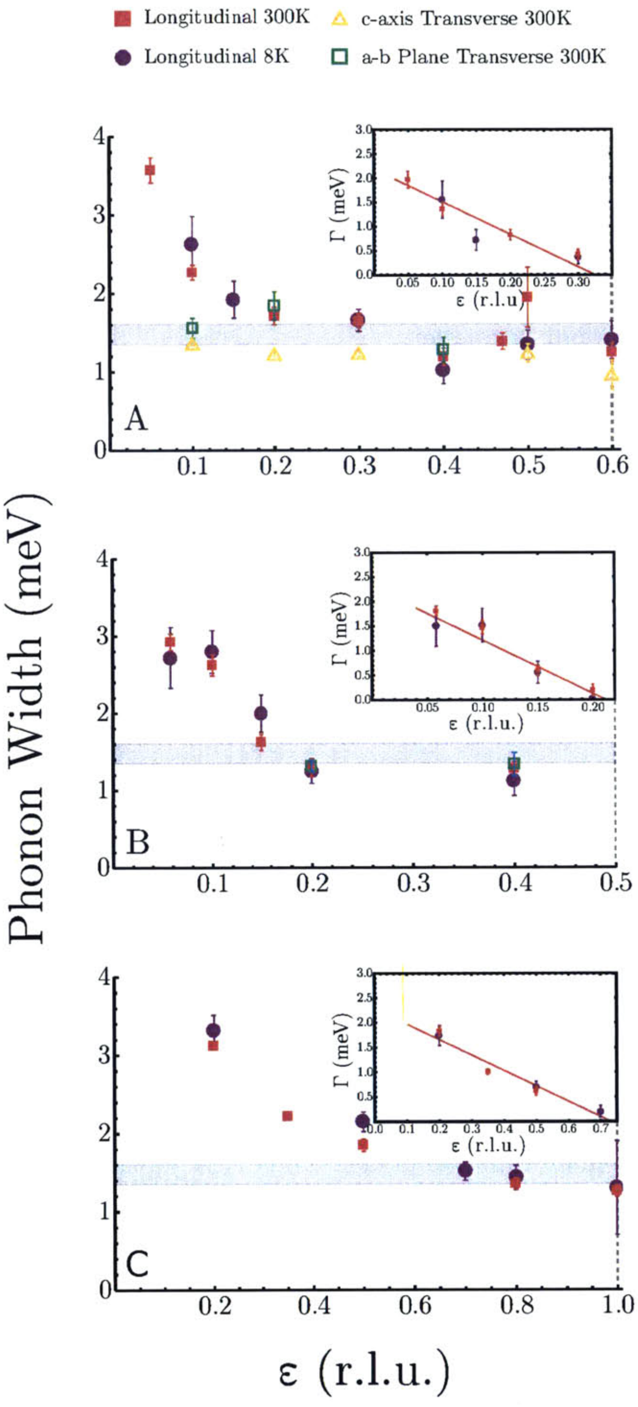

Figure 3-19: The phonon widths of acoustic modes extracted from fits. (A) are from modes along ($\epsilon 00$), (B) from ($\epsilon\epsilon 0$) and (C) for (00ϵ). The main figures are from fits without energy convolution (Eq. 3.8) The inset shows the width from the convolved fit.

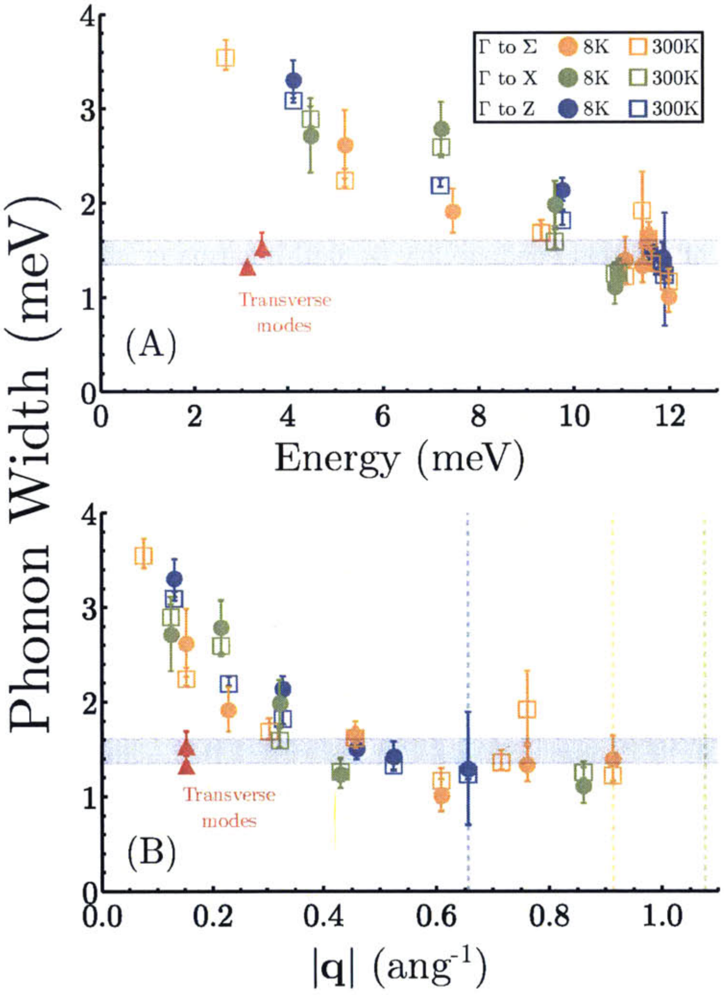

Figure 3-20: The phonon widths from fits to a damped-harmonic oscillator lineshape without convolution (Eq. 3.8) longitudinal acoustic branches from all high-symmetry cuts. (A) shows the width as a function of mode energy. (B) shows the widths as a function of $|\mathbf{q}|$. Dashed lines show the zone edge for each cut. The solid circles are from 8K phonons. The empty squares are from 300K phonons. Two transverse modes are highlight to emphasize the increased width of the longitudinal modes.

generated from the work by Yanagisawa et. al. Along Γ to Z, the data come from Wolfe et al. The shaded blue region denotes the maximal extent of our data for longitudinal modes. We can conclude there are no other longitudinal optical modes in the white region. We see no evidence for change in the dispersion as a function of temperature.

3.2.8 Thermal Conductivity

In the analysis of thermal conductivity by both Sharma et al. and Behnia et al. a large increase in thermal conductivity is seen upon cooling into the HO phase.[4, 92] The increase is seen with thermal current both in-plane and along the c axis. By analyzing the thermal hall conductivity, the conclude that the electronic contribution is extremely small and therefore the lattice contribution must be large and change significantly upon entering the HO phase. It is therefore quite surprising the inelastic x-ray data show no evidence for change in either the phonon dispersion or the linewidths as a function of temperature.

Under the realxation time approximation, the thermal conductivity from an excitation of wave vector $\mathbf{q}$ and branch j can be expressed as

$$\kappa_{\mathbf{q},j} = C_{\mathbf{q},j} v_{\mathbf{q},j} \lambda_{\mathbf{q},j} = C_{\mathbf{q},j} \mathbf{v}^2_{\mathbf{q},j} \tau_{\mathbf{q},j} \tag{3.11}$$

where $C_{\mathbf{q},j}$ is the heat capacity, $\mathbf{v}_{\mathbf{q},j} =$ is the group velocity, $\lambda_{\mathbf{q},j}$ is the mean free path, and $\tau_{\mathbf{q},j}$ is the relaxation time. κ is a rank-2 tensor and here we are calculating the longitudinal component that is parallel to the excitation propagation. Excitations not parallel to the thermal transport direction are reduced by $\cos\theta^2$. For an isotropic excitation, averaging over a sphere leads to a facto of $\frac{1}{3}$. The relaxation time is related to the width of the phonons, Γ as $\tau = \frac{\hbar}{\Gamma}$. [64] This method has successfully been used to calculate thermal conductivity from scattering data [79].

From inspection of Equations 3.11, at temperatures near the HO only acoustic phonons near the zone center have both sufficiently high heat capacity and group

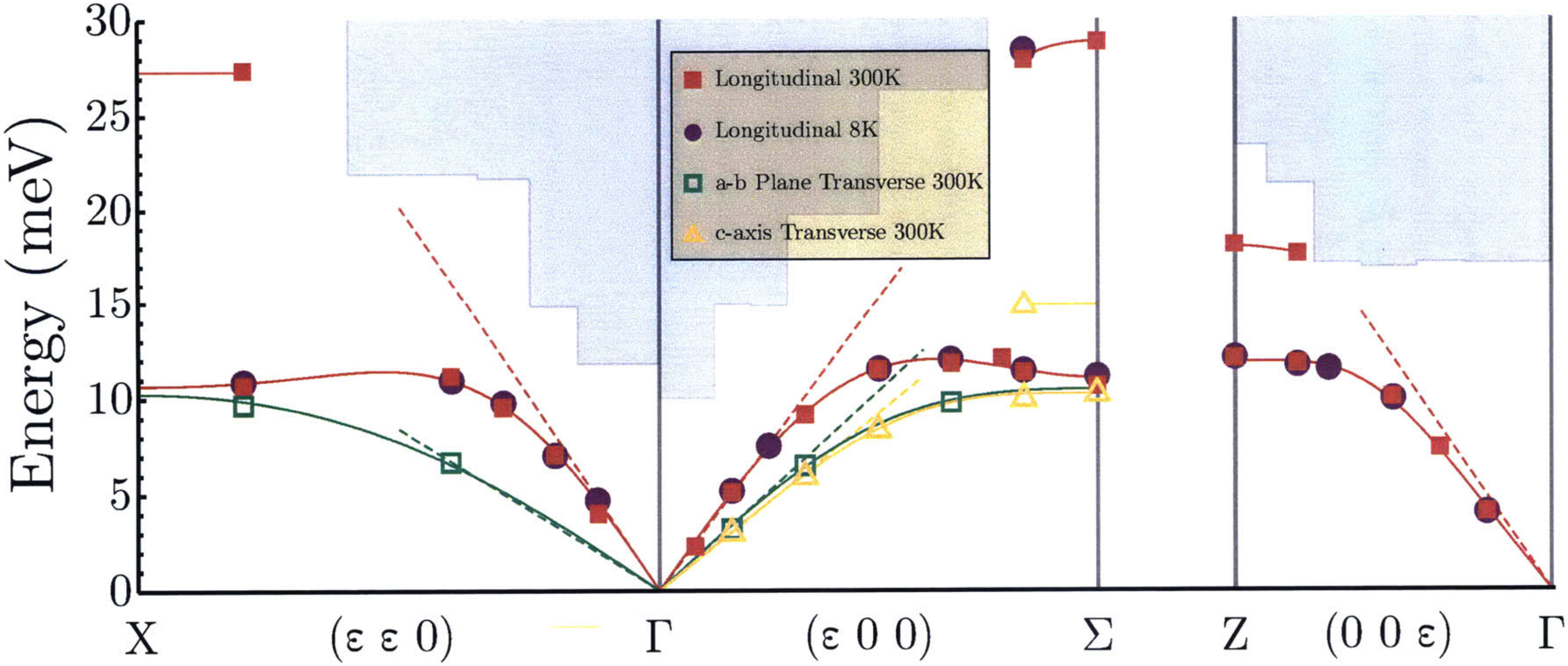

Figure 3-21: (A) The Brillouin zone of URu_2Si_2 assuming a body-centered tetragonal cell. High symmetry points are labeled. (B) A projection of reciprocal space on the (HK0) plane. Structural Bragg peaks are shown in black. (100) is not a zone centered, but rather the *Z* point on the zone edge from the (101) zone center

velocity to contribute significantly to the thermal transport. The acoustic modes away from the zone center have a very small group velocity and so contribute little; the optic modes are too high of energy to be thermally populated and so therefore should also contribute negligibly.

The measured intrinsic line width of the longitudinal branches allow for the direct approximation of their contribution to the thermal transport. To make this calculation, we make the following two assumptions:

1. The dispersion is isotropic. Measured dispersions and widths suggest that the longitudinal modes remain broad at low **q** in all directions and the high-symmetry longitudinal branches are smoothly deformed into each other. Additionally, the speed of sound is highest along the (100) direction, so any errors induced from this approximation would cause the calculation to overestimate the thermal conductivity of the branch.

2. The Brillouin zone can be approximated by a Debye sphere. At low temperature, only low energy modes are thermally populated. These modes are the acoustic modes, which only have high group velocity near the zone center. Thus this approximation is well justified.

Using these assumption we can calculated the contribution from the jth branch as

$$\kappa_{\mathrm{j}} = \int_0^{k_D} \mathrm{d}q \, \frac{1}{(2\pi)^2} \frac{4\pi}{3} k_B \left(\beta\hbar\,\omega_j(q)\right)^2 \frac{\mathrm{e}^{\beta\hbar\,\omega_j(q)}}{\left(\mathrm{e}^{\beta\hbar\,\omega_j(q)} - 1\right)^2} \frac{\partial}{\partial q}\omega_j(q)\lambda \tag{3.12}$$

For the region of of the dispersion near the zone center which the intrinsic line width can be extracted, we use this to calculate the mean free path. For the remainder of the branch, we use the upper bound of 1mm, which represents boundary scattering from sample sizes typical for thermal transport measurements. For thermal transport along **a** at 8K, the longitudinal branch only contributes $\sim 0.2\frac{\mathrm{W}}{\mathrm{K\,m}}$, a negligible amount of the total conductivity. Furthermore, the vast majority of the thermal energy is transported by the modes for which we could not determine the lifetime. This number should therefore be viewed as an extreme upper limit on the longitudinal contribution.

For the transverse modes, we cannot extract an intrinsic line width from any of the modes as they are resolution limited. Therefore, it is impossible to rule out a massive increase in the thermal transport from these modes upon entering the Hidden Order. However, the mean free path lower bound for resolution transverse phonons near the zone center is only ~30 Å. We can calculate an effective mean free path for the entire transverse branches necessary to match the reported thermal conductivity. This effective λ must increase from ~ 1 μm above the HO to ~ 50 μm immediately below it. This change must occur to the mean free path throughout the entire Brillouin zone to account for the increase of thermal conductivity in all measured directions and thus seems an unlikely source for the increase in thermal conductivity.

A more likely explanation is that the known magnetic excitation are the source of the thermal transport increase in the HO phase. Thermal transport from magnetic excitations has been observed in a variety of materials including multiferroics, spin ice, monolayer cuprates, and low-dimensional spin systems.[66, 6, 114, 99, 45]. Inelastic neutron scattering measurements on spin-wave dispersions on $CrSb_2$ have been used to explain the anisotropy in the thermal conductivity.[96]. In URu_2Si_2, neutron scattering data reveal below T_0, there are well-defined magnetic excitations throughout the Brillouin zone. Minima in the excitations occur at $Q_0 = (1\ 0\ 0)$ and $Q_1 = (1.4\ 0\ 0)$ with gaps of 1.7 and 4.2 meV respectively. These modes are dispersive and sharp in all measured directions and are low enough in energy to be thermally active thus should contribute to thermal transport.

Above T_0,the excitation at Q_0 is thought to go gapless but heavily overdamped. The excitation at Q_1 lowers to 2.1 meV, but also becomes heavily damped [13, 105, 106, 49, 107, 12]. Thus the magnetic excitations above T_0 are incapable of carrying appreciable thermal current.

At first it may be tempting to dismiss this transport mechanism under the assumption that the modes are frozen out. It is common view the temperature of the

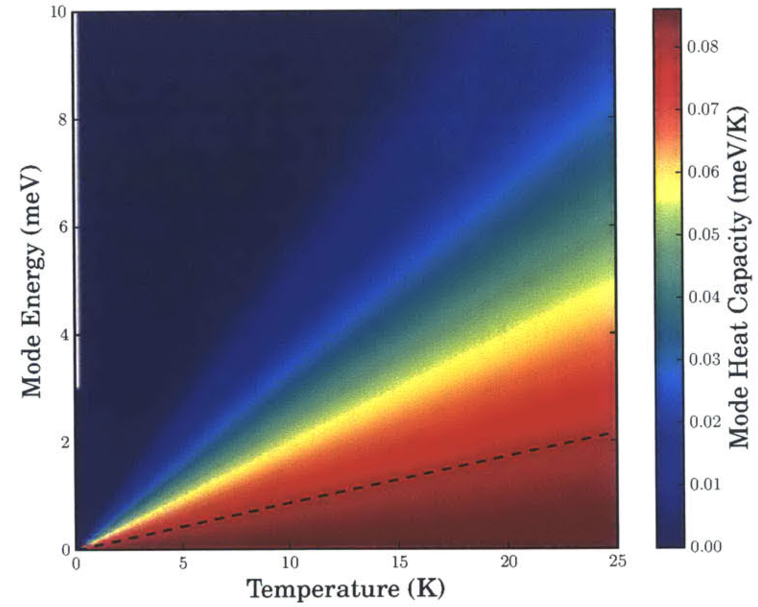

Figure 3-22: Heat capacity for Bosonic excitations as a function of mode energy and temperature. In the high temperature limit, a single mode contribute $k_B = 0.0861$ meV/K

energy of a bosonic excitation as being the rough estimate of when that excitation becomes relevant. Much below this temperature, the modes do not contribute, and much above the temperature, the modes are fully active and contribute k_B to the heat capacity. In fact, the temperature of an excitation is much closer to the when the mode becomes saturated than when it starts contributing appreciably.

This is demonstrated in Fig. 3-22 in which the single mode heat capacity is shown as a function of temperature and mode energy. The dashed black line equivalence between temperature in Kelvin and energy in meV. The magnetic excitations have minima at 1.7 and 4.2 have significant thermal population at 17.5 K and thus are capable of contributing to the thermal conductivity.

3.3 Conclusions

Previous experimental and theoretical inquiries into URu_2Si_2 have suggested the the HO phase strongly couples to the lattice. Fermi surface measurements and calculations suggest a zone folding along $\mathbf{Q_0} = (001)$, which reduces the symmetry of the crystal. Torque magnetometry and x-ray diffraction on small samples with high RRR demonstrate a breaking of C4 symmetry and and orthorhombic distortion. Finally, thermal conductivity studies suggest that the lattice contribution to thermal conductivity increases upon entering the HO phase.

Given the preponderance of evidence pointing to significant changes to the lattice in the HO state, our x-ray scattering measurements show surprisingly little temperature dependence. We see no evidence of an orthorhombic distortion up to $\delta \sim 6 * 10^{-5}$, where $\delta = \frac{b_{ortho} - a_{ortho}}{b_{ortho} + a_{ortho}}$. Because the sample RRR used for the diffraction is low, it is consistent with the literature's claim on the dependence of the distortion on RRR. At this point, there is no understanding on the mechanism through which the distortion can depend on the sample's RRR. This is particularly perplexing as the heat capacity jump upon entering the HO does not depend upon RRR.

The inelastic scattering measurements of the acoustic phonons show no evidence of change upon entering the HO phase. The longitudinal acoustic modes along all high-symmetry directions show an anomalous broadening as $\mathbf{q} \to 0$. The cause of this broadening is not currently understood, but is interpreted as phonons coupling to other degrees of freedom at all temperatures. Due to the similarities of energy scales, it is possible that the coupling is to the 1.9 meV magnetic excitation seen at $\mathbf{Q_0} = (100)$, the 1.6 meV excitation seen in electronic Raman scattering, or disorder.

The low-q acoustic phonons are precisely the modes that are most important for lattice thermal conductivity at low temperature because they are both thermally active and strongly dispersive. The measured phonon widths allow us to model the contribution of the longitudinal modes to thermal conductivity and conclude that they cannot be responsible for the increase the κ upon entering the HO phase, regardless of the exact form of the coupling. Additionally, the lack of change of the dispersion and lineshape of all measured modes strongly suggest the affect of the HO on κ does not come from the lattice. The most plausible explanation is the magnetic excitations drive the change in thermal conductivity.

Chapter 4

Overview of Dichroism

Measurements of dichroism and other optical activity measurements are powerful techniques that, among other information, can shed light on symmetry breaking. Modern synchrotrons make these experiments increasingly common in hard condensed matter. In this chapter, we briefly summarize symmetry and polarization considerations of light and the quantum mechanical descriptions of absorption.

4.1 Parity and Time Reversal Symmetry

Parity (chiral) symmetry and time reversal symmetry are two fundamental discrete symmetries. A good review of quantum mechanical results of these symmetries is presented by Sakuri. Here, we'll discuss how the symmetries affect basic physical quantities.

A *parity transformation* is defined by the replacement

$$\begin{pmatrix} x \\ y \\ z \end{pmatrix} \rightarrow \begin{pmatrix} -x \\ -y \\ -z \end{pmatrix} \tag{4.1}$$

If we introduce a parity operator $\mathcal{P}$, we say that a quantity A that satisfies $\mathcal{P}A = A$ as even, or gerade (g) parity. A quantity B that satisfies $\mathcal{P}B = -B$ has odd, or ungerade (u) parity. $\mathcal{P}$ has eigenvalues ± 1. The parity of basic physical quantities are given in Table 4.1. In reference to the symmetry of crystal lattices, parity symmetry is

Odd	Even
position	time
velocity	angular momentum
force	torque
electric field	magnetic field
helix (handedness)	

Table 4.1: Parity Symmetry: Physical quantities organized by their parity symmetry

referred to as inversion symmetry. Vector quantities that are parity even, such as angular momentum, are sometime referred to as pseudo-vectors. Scalar quantities that are parity odd called pseudo-scalars.

The time reversal operator, $\mathcal{T}$ is defined by the operation

$$t \to -t \tag{4.2}$$

We similarly refer to quantities as time-even that satisfy $\mathcal{T}A = A$ and time-odd that satisfy $\mathcal{T}B = -B$. The eigenvalues for the $\mathcal{T}$ are ± 1. Physical quantities that depend linearly on time or are first derivatives of time must be time-odd while quantities that do not originate from time are time-even. The time-reversal symmetry of basic physical quantities are given in Table 4.2.

Odd	Even
time	position
velocity	force
angular momentum	torque
magnetic field	electric field
	helix (handedness)

Table 4.2: Time Reversal Symmetry: Physical quantities organized by their $\mathcal{T}$ symmetry

4.2 Polarization of Light

Maxwell's equations in free space lead to transverse E&M waves. A wave traveling in the z-direction with wavenumber k and frequency ω can be described by its electric and magnetic field components

$$\mathbf{E}(z,t) = \boldsymbol{\epsilon_p} E_0 e^{i(kz-\omega t)} \tag{4.3}$$

$$\mathbf{B}(z,t) = \frac{1}{c}(\hat{z} \times \boldsymbol{\epsilon_p}) E_0 e^{i(kz-\omega t)} \tag{4.4}$$

Where $\boldsymbol{\epsilon_p}$ is the unit polarization vector, which in general is complex. From here on, light will be denoted and discussed only with reference the electric field component. The magnetic field can always be calculated from the electric field whenever necessary.

The transverse nature of light is ensured by the constraint, $\boldsymbol{\epsilon_p} \cdot \hat{z} = 0$. Thus the full polarization of coherent light requires three quantities. These are typically given by two orthogonal basis functions plus a phase. Linear basis functions can be written conveniently as light polarized along the x and y axes:

$$\mathbf{E}_x(z,t) = \hat{x} E_0 e^{i(kz-\omega t)+i\phi_x} \tag{4.5}$$

$$\mathbf{E}_y(z,t) = \hat{y} E_0 e^{i(kz-\omega t)+i\phi_y} \tag{4.6}$$

Circularly polarized light can be constructed by adding orthogonally polarized linear light with a $\frac{\pi}{2}$ relative phase shift. Mathematically, we do this by define two complex and orthogonal unit vectors

$$\frac{1}{\sqrt{2}}\hat{x} \pm i\hat{y} \tag{4.7}$$

The two different polarizations are referred to as left and right. There are two different conventions for determining which is which. We use the convention in which the handedness is determined with the thumb pointing along the propagation direction and fingers curled along the rotation of the **E**-vector in time. Note that the **E**-vector rotates in the opposite since if looking at a fixed time but moving in space along the propagation direction. Using this convention, the circular basis functions can be written

$$\begin{aligned}\mathbf{E}_{\mathcal{R}}(z,t) &= \boldsymbol{\epsilon_R} E_0 e^{i(kz-\omega t)+i\phi_R} \\ \mathbf{E}_{\mathcal{L}}(z,t) &= \boldsymbol{\epsilon_L} E_0 e^{i(kz-\omega t)+i\phi_L} \\ \text{with } \boldsymbol{\epsilon_R} &= -\frac{1}{\sqrt{2}}(\hat{x}+i\hat{y}) \\ \boldsymbol{\epsilon_L} &= \frac{1}{\sqrt{2}}(\hat{x}-i\hat{y})\end{aligned} \tag{4.8}$$

A coherent wave can be any linear superposition of a given basis with complex weights. In general, this leads to a wave that is neither purely circular or purely linear, but rather an elliptically polarized wave.

$$\begin{aligned}\mathbf{E}_{ell}(z,t) &= \frac{1}{\sqrt{2}}(\hat{x}E_{0x}e^{i(kz-\omega t)} + \hat{y}E_{0y}e^{i(kz-\omega t)}) \\ &\text{or} \\ \mathbf{E}_{ell}(z,t) &= \frac{1}{\sqrt{2}}(\boldsymbol{\epsilon_R}E_{0R}e^{i(kz-\omega t)} + \boldsymbol{\epsilon_L}E_{0L}e^{i(kz-\omega t)})\end{aligned} \tag{4.9}$$

For many experimental purposes, full polarization analysis is unnecessary. It is often sufficient to use the *degree of polarization*, P, which we define as

$$P_{linear} = \frac{|I_x - I_y|}{I_x + I_y} \tag{4.10}$$

$$P_{circular} = \frac{|I_{\mathcal{R}} - I_{\mathcal{L}}|}{I_{\mathcal{R}} + I_{\mathcal{L}}} \tag{4.11}$$

$$P_{linear} = \frac{|E_{0x}^2 - E_{0y}^2|}{E_{0x}^2 + E_{0y}^2} = \frac{2|E_{0R}E_0 y|}{E_0 x^2 + E_0^2 y} \tag{4.12}$$

$$P_{circular} = \frac{|E_{0\mathcal{R}}^2 - E_{0\mathcal{L}}^2|}{E_{0\mathcal{R}}^2 + E_{0\mathcal{L}}^2} = \frac{2|E_{0x}E_{0y}|}{E_0 x^2 + E_0^2 y} \tag{4.13}$$

For coherent light, the degree of linear polarization is related to the degree of circular polarization

$$P^2_{linear} = 1 - P^2_{circular} \tag{4.14}$$

For natural light, which consists of an incoherent superposition of polarization states, the polarization varies rapidly and Eq. 4.12 no longer holds.

A convenient formalism for light is the Poincare sphere and closely related Stokes vector. We start by defining a polarization vector $\mathbf{P} = (S_1, S_2, S_3)$. These parameters are defined as shown in table

$\begin{pmatrix} 1 \\ 0 \\ 0 \end{pmatrix}$	Linearly Polarized (Horizontal)	$\begin{pmatrix} -1 \\ 0 \\ 0 \end{pmatrix}$	Linearly Polarized (Vertical)
$\begin{pmatrix} 0 \\ 1 \\ 0 \end{pmatrix}$	Linearly Polarized (45°)	$\begin{pmatrix} 0 \\ -1 \\ 0 \end{pmatrix}$	Linearly Polarized (−45°)
$\begin{pmatrix} 0 \\ 0 \\ 1 \end{pmatrix}$	Right Handed Circular	$\begin{pmatrix} 0 \\ 0 \\ -1 \end{pmatrix}$	Left Handed Circular

Table 4.3: Polarization Parameterization

The Poincare sphere is a representation of this vector, as shown in Figure 4-1. The poles represent circular polarization. The equatorial plane represents linear polarizations.

The full Stokes vector is the polarization vector with an additional S_0 term equal to the intensity of the light: $\mathbf{S} = (S0, S1, S2, S3)$. For a coherent light source $S_0 = I = \sqrt{S_1^2 + S_2^2 + S_3^2}$.

Optically active materials can change the polarization of transmitted or reflected light. A material for which right and left handed circularly polarized light have different phase velocities, will produce a precession angle ψ across the equatorial plane. A difference in phase velocity of orthogonal linear polarizations create a polar precession angle χ. This effect also occurs in materials the preferential absorb left handed or right handed circularly polarized light. A quarter wave plate is an optical device for which the polarization vector is rotated 90 degrees, making linearly polarized light

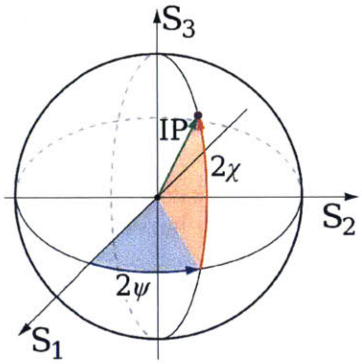

Figure 4-1: In the Poincare sphere, the polarization vector P of length I is decomposed into the three Stokes parameters S_1, S_2, and S_3 plotted as the cartesian coordinates

circular. A half wave plate flips horizontally polarized light to vertical and vice versa.

The angular momentum of an EM wave propagating along z can be calculated as

$$\langle L_z \rangle = \frac{\int E^*(z,t) L_z E(x,t) \mathrm{d}\Omega}{\int E^*(z,t) E(x,t) \mathrm{d}\Omega} \tag{4.15}$$

To evaluate this quantity, we rewrite the circular basis function in terms of the spherical harmonics

$$\mathbf{E}_{\mathcal{R}}(z,t) = \sqrt{\frac{4\pi}{3}} Y_{1,1} E_0 e^{i(kz-\omega t)} \tag{4.16}$$

$$\mathbf{E}_{\mathcal{L}}(z,t) = \sqrt{\frac{4\pi}{3}} Y_{1,-1} E_0 e^{i(kz-\omega t)} \tag{4.17}$$

$$\text{where } Y_{1,\pm 1} = \mp \sqrt{\frac{3}{4\pi}} \frac{1}{\sqrt{2}} \frac{x \pm iy}{r}$$

Spherical harmonics have the properties

$$\int Y^*_{l',m'} Y^*_{l,m} \mathrm{d}\Omega = \delta_{l',l} \delta_{m',m} \tag{4.18}$$

$$\int Y^*_{l',m'} L_z Y^*_{l,m} \mathrm{d}\Omega = \hbar m \delta_{l',l} \delta_{m',m} \tag{4.19}$$

we can see that $\langle L_z \rangle = \pm \hbar m$ for right and left handed circularly polarized light respectively. Furthermore, as linear polarized light can be written as the superposition of left and right circularly polarized light, $\langle L_z \rangle = 0$ for linearly polarized light. The angular momentum of circularly polarized light is important in analyzing circular dichroism, as shall be seen shortly.

The relationship between handedness of circularly polarized light and angular momentum tempts a false equivalence. Importantly, handedness, or *chirality* has different symmetry from angular momentum. Chirality is parity-odd and time-even. It does not, however, change with any proper rotation. On the other hand (no pun intended), angular momentum is parity-even and time-odd.

Experimentally, these difference lead to distinct physical phenomena. For example, the angular momentum coupling of X-rays to a magnetic sample is dependent upon the relative orientation of the angular momentum and magnetic moment. This effect is X-ray Magnetic Circular Dichroism (XMCD) This effect can be thought of as a result of the changing orientation of the **E** field in time while approximating the spatial variation as negligible (i.e. a dipole approximation.) It is *parity-even* and *time-odd* phenomena.

Alternatively, the chirality of circular light can also couple to materials that do not have inversion symmetry such as chiral molecules. The difference in interaction between left handed and right handed circularly polarized light is called X-ray natural circular dichroism (XNCD). Note that this can be observed even in collections of randomly oriented molecules as long as they all have the same handedness. In this case the effect is a result of the spatial rotation in the **E** field. It is *parity-odd* and *time-even* phenomena.

4.3 Quantum Mechanical Description of Absorption

There are various good references outlining the quantum mechanical description of light interacting with matter. Sakuri is the classic quantum mechanics text.[88] Shirani provides an excellent review with emphasis on inelastic neutron scattering.[93] Grosso provides a great overview of in particularly nice notation.[37] Stöhr and Siegmann's book on magnetism have an excellent summary for absorption.[95] Here we follow the notation of Stöhr and Siegmann.

4.3.1 Fermi's Golden Rule

The starting point for a quantum mechanical description of light interacting with matter, both from absorption and scattering, is time-dependent perturbation theory. The time-dependent EM field from light induces transitions from initial state $|i\rangle$ to final state $|f\rangle$. These states contain both the state of the sample and the state of the photon. The original formalism was derived by Kramers and Heisenberg and by Dirac

Up to first order perturbation theory, the transition probability per unit time from a state i to a state f is

$$T_{i,f} = \frac{2\pi}{\hbar} \left|\langle f|\mathcal{H}_{int}|i\rangle\right|^2 \delta(\epsilon_i - \epsilon_f)\rho(\epsilon_f) \tag{4.20}$$

where H_{int} is the interaction Hamiltonion, ϵ is the energy of sample state and photon combined, and $\rho(\epsilon)$ is the density of states per unit energy. The delta function insures energy conservation. The units of $T_{i,f}$ are time^{-1}. This result is commonly referred to as Fermi's Golden Rule.

The total cross-section and differential cross-section are obtained by normalization by incident photon flux Φ_0

$$\sigma = \frac{T_{i,f}}{\Phi_0} \tag{4.21}$$

$$\frac{\mathrm{d}\sigma}{\mathrm{d}\Omega} = \frac{T_{i,f}}{\Phi_0 \mathrm{d}\Omega} \tag{4.22}$$

4.3.2 Absorption under dipolar approximation

For absorption, the interaction Hamiltonian is

$$\mathcal{H}_{int} = \frac{e}{m_e}\mathbf{p} \cdot \mathbf{A} \tag{4.23}$$

where $\mathbf{p}$ is the momentum operator and $\mathbf{A}$ is the vector potential from the EM wave. When inserting this interaction Hamiltonian into Eq. 4.20, in an absorption process, the quantized vector potential annihilation operator acts on the photon part of the initial state and collapses with the phonon component of the final state. For a more thorough mathematical description, see for example Riseborough. [86] The remaining matrix elements have only the sample states and have the general form

$$\mathcal{M} = \langle b|\mathbf{p} \cdot \boldsymbol{\epsilon}\, e^{i\mathbf{k}\cdot\mathbf{r}}|a\rangle \tag{4.24}$$

where the states $|b\rangle$ and $|a\rangle$ are the final and initial state respectively of the sample.

To evaluate these matrix elements for x-ray absorption, we expand the exponential in the limit $\mathbf{k} \cdot \mathbf{r} \ll 1$

$$\mathcal{M} = \langle b|\mathbf{p} \cdot \boldsymbol{\epsilon}\, (1 + i\mathbf{k} \cdot \mathbf{r} + \cdots)|a\rangle \tag{4.25}$$

The lowest order term is the electric dipole term. This is equivalent to the approximation that the electric field does not change over the length of the interaction $\mathbf{r}$. The next higher order term, $i\mathbf{k} \cdot \mathbf{r}$ contains the electric quadruple and magnetic dipole interaction. This will play an important role in XNCD as will be discussed shortly. Successively higher orders in the expansion lead to increasing rank multipole terms.

To evaluate the dipolar term, we note that $[x, \mathcal{H}_0] = i\frac{\hbar}{m_e}\mathbf{p}$ where $\mathcal{H}_0$ is the perturbed Hamiltonian, for which $|b\rangle$ and $|a\rangle$ are eigenstates. We then have the total cross-section for absorption

$$\sigma^{abs} = 4\pi^2 \frac{e^2}{4\pi\epsilon_0 \hbar c} \hbar\omega \left|\langle b|\boldsymbol{\epsilon} \cdot \mathbf{r}|a\rangle\right|^2 \delta\left(\hbar\omega - (E_b - E_a)\right) \rho(E_b) \tag{4.26}$$

Where E_a, b refer to the energy of the unperturbed sample state and $\hbar\omega$ is the photon energy for the transition.

By integrating over final states the X-ray absorption intensity under the dipole approximation is

$$I_{res} = \mathcal{A}\left|\langle b|\boldsymbol{\epsilon}\cdot\mathbf{r}|a\rangle\right|^2 \tag{4.27}$$
$$\text{with } \mathcal{A} = 4\pi^2\frac{e^2}{4\pi\epsilon_0\hbar c}\hbar\omega$$

This is the integrated intensity over the entire absorption edge. It has dimension of length^2×energy.

4.3.3 Dipole Operator and Selection Rules

Now the problem is just to calculate the matrix elements $\langle b|\boldsymbol{\epsilon}\cdot\mathbf{r}|a\rangle$. To do so, recall from Section 4.2 that the polarization of light can be written in terms of spherical harmonics with $l = 1$. For ease of notation we introduce Racah's spherical tensor operators:

$$C^l_m = \sqrt{\frac{4\pi}{2l+1}}Y_{l,m}(\theta,\phi) \qquad\qquad C^l_{-m} = (-1)^m\left(C^l_m\right)^* \tag{4.28}$$

We also introduce the dipole operator $P = \boldsymbol{\epsilon}\cdot\mathbf{r}$. We commonly denote a specific polarization and direction of propagation as P^q_α, where $\alpha = x, y, z$ is the propagation direction relative to the sample, and q denotes the angular momentum of the polarization: 1, 0, or -1. Dipole operator defined by a direction and polarization can be written

$$\frac{P^q_\alpha}{r} = \sum_{p=0,\pm1} e^q_{\alpha,p}\,C^1_p \tag{4.29}$$

The coefficients $e^q_{\alpha,p}$ are in general complex and subject to the constraint $\sum_p |e^q_{\alpha,p}|^2 = 1$. Note that this leaves five parameters: three parameters are needed to determine the polarization and two parameters are needed to determine the direction of propagation. This formalism makes it clear that evaluating the matrix element $\langle b|\boldsymbol{\epsilon}\cdot\mathbf{r}|a\rangle = \langle b|P^q_\alpha|a\rangle$ only consists of terms of the form $\langle b|r\ Y_{1,m}|a\rangle$.

In the single electron approximation, the initial $|a\rangle$ is a core electron wavefuntion.

The final state is a linear combination of core wavefunctions. We describe these as atomic orbitals, the solutions to a central potential:

$$R_{n,l}(r)Y_{1,m_l}(\theta,\phi)\chi_{s,m_s} = |R_{n,l}(r); l, m_l, s, m_s\rangle \tag{4.30}$$

Evaluating the radial part of the matrix element gives

$$\mathcal{R} = \langle R_{n',l'}|r|R_{n,l}\rangle = \int_0^\infty R^*_{n',l'}(r)\, R_{n,l}(r)\, r^3 \mathrm{d}r \tag{4.31}$$

This radial integral rapidly vanishes for any states except those localized on the atomic center. The localization is why the final states can also be treated linear combination of the atomic states of the resonant atom and thus X-ray absorption spectroscopy is element specific and sensitive only the the local properties of the target atom.. Optical spectroscopy, in contrast, does not have localization and the probed states can be extended or itinerant.

The angular part of the transition matrix has elements of the form

$$\mathcal{Y} = \langle l', s', m'_l, m'_s|C_q^{l''}|l, s, m_l, m_s\rangle \tag{4.32}$$

Evaluating these expressions give the following selection rules:

$$\Delta l = \pm l'' \tag{4.33}$$

$$\Delta m_l = q = 0, \pm 1 \tag{4.34}$$

$$\Delta s = 0 \tag{4.35}$$

$$\Delta m_s = 0 \tag{4.36}$$

where the angular momentum of the x-ray photon is $q\hbar$. In the dipole approximation, only matrix elements with $l'' = 1$ exist, so $\Delta l = \pm 1$.

Commonly, the eigenstates of the unperturbed Hamiltonian are not of the form $|l, s, m_l, m_s\rangle$, but rather are in the spin-orbit coupling dominated regime. In this case, the eigenfunctions are of the form $|l, s, j, m_j\rangle$. The selection rules are applied after writing the state out as linear combinations of the $|l, s, m_l, m_s\rangle$ states via the Clebsch-Gordon coefficients.

4.3.4 Summary of Quantum Mechanical Analysis of Absorption

The analysis of absorption begins with perturbation theory and Fermi's Golden Rule. This analysis leads to several key points useful to summarize and keep in mind going forward.

- The resonant x-ray edge occurs when the x-ray energies are tuned such that absorption signal is dominated by atomic like transitions.

- The dipole approximation is sufficient to describe most of absorption phenomena. This approximation is the expansion of $e^{i\mathbf{k}\cdot\mathbf{r}}$. XNCD requires higher order terms in the expansion

- As the initial state is a core orbital, the radial terms in the matrix element rapidly die at distances 0.5 Å^{-1}. For this reason, resonant absorption spectroscopy is highly localized and element specific. The localization means the final states must be combinations of atomic orbitals and not itinerant.

- The angular components of the matrix elements depend on the polarization and direction of the incident x-rays. This give rise to selection rules. Notably, the magnetic quantum number m_l changes by the angular momentum of the incident x-rays

- Commonly, the core states are spin-orbit split. These states are written in terms of combinations of the $|l, s, m_l, m_s\rangle$ states via the Clebsch-Gordon coefficients. The spin-orbit coupling is critical for the existence of XMCD.

4.4 X-ray Natural Circular Dichroism

Magnetic circular dichroism was first measured in the x-ray region by Shütz in 1987.[91] This work, an most subsequent XMCD work, is accomplished through the reversal of the magnetic field. Only with the construction of the helical undulatory at the European Synchrotron Radiation Facility (ESRF) in the mid-90's, did it become possible to measure circular dichroism through changing of helicity of the polarized x-rays.[34] Shortly thereafter, the first XNCD measurements were reported on $Na_3[Nd(dimly)_3]\cdot 2NaBF_4\cdot 6H_2O$.[1] The effect was soon seen in a series of other materials and theoretical calculations on intensities soon followed.[36, 33, 35, 72, 14, 82, 65]. Here we outline some of the key theoretical results of XNCD.

As mentioned above, the interaction Hamiltonian can be expanded into higher multipoles. The transition operator can be then written as a series of multipole contributions:

$$T = \mathbf{E}1 + \mathbf{E}2 + \mathbf{E}3 + \cdots + \mathbf{M}1 + \mathbf{M}2 + \mathbf{M}3 + \cdots \tag{4.37}$$

The only terms that can contribute to the dichroism of circularly polarized light are the combinations that are of opposite parity. The lowest order combinations are the $\mathbf{E}1 \cdot \mathbf{M}1$ and $\mathbf{E}1 \cdot \mathbf{E}2$.

To see this explicitly, take the second order expansion terms of of the interaction Hamiltonian in the absorption cross-section:

$$\sigma^{abs} = 4\pi^2 \frac{e^2}{4\pi\epsilon_0 \hbar c} \hbar\omega \left|\langle b|\boldsymbol{\epsilon}\cdot\mathbf{p} + i(\boldsymbol{\epsilon}\cdot\mathbf{p})(\mathbf{k}\cdot\mathbf{r})|a\rangle\right|^2 \delta\left(\hbar\omega - (E_b - E_a)\right)\rho(E_b) \tag{4.38}$$

the second term in the matrix element can be expanded

$$\begin{aligned}(\boldsymbol{\epsilon}\cdot\mathbf{p})(\mathbf{k}\cdot\mathbf{r}) =& 1/2[(\boldsymbol{\epsilon}\cdot\mathbf{p})(\mathbf{k}\cdot\mathbf{r}) + (\boldsymbol{\epsilon}\cdot\mathbf{r})(\mathbf{k}\cdot\mathbf{p})] + & (4.39)\\ & 1/2[(\boldsymbol{\epsilon}\cdot\mathbf{p})(\mathbf{k}\cdot\mathbf{r}) - (\boldsymbol{\epsilon}\cdot\mathbf{r})(\mathbf{k}\cdot\mathbf{p})] & (4.40)\end{aligned}$$

The first, symmetric, term on the right-hand side is the electric quadrupole. The second, anti-symmetric, term is the magnetic monopole. It is clear that both terms are odd under inversion can contribute to the XNCD at the same order in $\mathbf{k} \cdot \mathbf{r}$.

A key distinguishing feature of the two terms is that the $\mathbf{E1} \cdot \mathbf{M1}$ term is a pseudo scalar quantity and thus the effect persists for randomly oriented samples while the $\mathbf{E1} \cdot \mathrm{E2}$ term will average to zero. The two terms can then be distinguished polar dependency of the dichroic signal. Selection rules for the magnetic dipole transitions forbid excitations from the s orbitals. Therefore at the K edge, $\mathbf{E1} \cdot \mathbf{M1}$ absorption must require s-p orbital mixing and so the intensities are orders of magnitude smaller than expected for $\mathbf{E1} \cdot \mathbf{E2}$.[82] For both terms contributing to XNCD, the dichroism will have the same sign when the sample is rotated 180 degrees. The same type of rotation would invert the sign of XMCD.

When evaluating the matrix elements of the $\mathbf{E1} \cdot \mathrm{E2}$, it is useful to again express the the expansion of the interaction Hamiltonian in terms of the Racah spherical tensors. This leads to matrix elements of the form

$$\langle f|rC^1_m|g\rangle\langle g|r^2C^2_m|f\rangle \tag{4.41}$$

Similarly as with the dipole approximation, the angular components can be calculated an lead to selection rules, including that Δl is equal the orbital value of the Racah tensor. Since the initial states are well approximated by core orbitals, the intermediate state must a hybridization of orbitals of different azimuthal quantum number. For K-edge dichroism, XNCD will probe $\mathbf{E1} \cdot \mathrm{E2}$ interference of an intermediate state of hybridized p and d orbitals.

Chapter 5

Dichroism measurements of symmetry in the pseudo gap state of BSCCO

5.1 Introduction

The parent compound for high-T_c are Mott insulators. Doping these materials lead to the phase diagram shown in Fig. 5-1. A large area of research is in understanding the pseudogap regime that occurs in the underdoped region. This phase is visible through spin susceptibility detected by the Knight shift and c-axis conductivity. One key question is whether this is a true separate phase or a crossover region. If it is a distinct phase, how do we understand the order. Lee, Nagaosa and Wen wrote a good overview of this rich field.[58]

Recently, a series of experimental observations suggest the pseudogap is a distinct phase, which we will briefly summarize. Polarized neutron diffraction has shown novel magnetic order in the pseudogap that preserves translational symmetry in bilayer YBCO[30], monolayer HBCO [59], and bilayer BSCCO [24]. X-ray scattering, combined with STM and ARPES suggest that the pseudogap is characterized by a charge density wave, the wave vector of which depends on doping in BSCCO[108, 20],

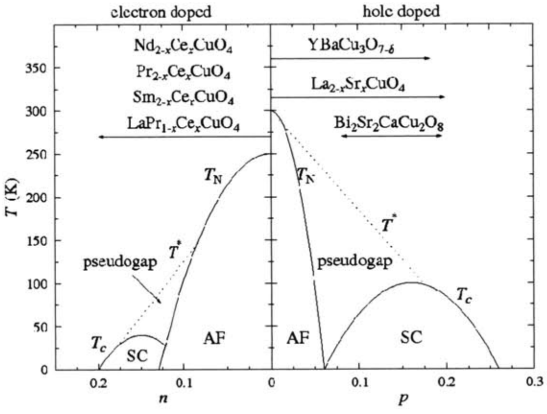

Figure 5-1: Phase diagram for high T_c superconductors

and YBCO. [57] The polar Kerr effect has been measured in BSCCO[41], though considerable confusion and debate exists about the interpretation of this and whether or not it necessitates the breaking of time-reversal symmetry.[47, 32, 46, 51] Inelastic x-ray scattering has seen a violation of detailed balance in phonons, which necessitate the breaking of both inversion and time reversal symmetry breaking.[8] Birefringence and dichroism have been measured in YBCO in the THz regime, which necessitate the loss of both C4 rotation and mirror symmetries in the electronic structure.[61]

Finally, circular dichroism as the copper K-edge has been reported in $Bi_2CaCu_2O_{8+x}$ (Bi-2212).[54] This has been interpreted as x-ray natural circular dichroism (XNCD), which breaks inversion symmetry but not time-reversal. This work remains controversial. Di Matteo and Norman point out that glide plane symmetries must also be broken for there to be a non-zero signal. Additionally, the possibility of linear contamination in the x-rays was not ruled out by measuring the azimuthal dependence of the dichroism.[26] If the dichroic signal is real, polar dependency can be used to match various theoretical models of ordering.[74] In this work, we further investigate dichrosim at the copper K-edge of Bi-2212.

The crystal structure of Bi-2212 is shown in Fig. 5-2. Most of the literature treats the crystal as tetragonal, such that the copper-copper nearest neighbors are along $\mathbf{a}_{tet}$ and $\mathbf{b}_{tet}$. We will however use the crystallographically correct orthorhombic

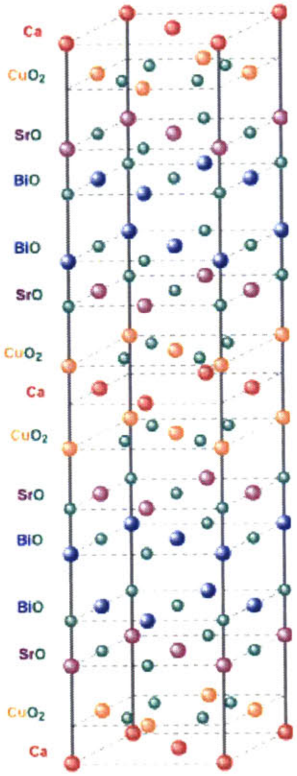

Figure 5-2: The unit cell of Bi-2212. This cell is the orthorhombic unit cell, with a=5.402 Å and b=5.404 Å. There is an incommensurate modulation with reciprocal lattice vector $\mathbf{q_{sl}} = \pm 0.22\mathbf{b}^* \pm \mathbf{c}^*$.

notation, for which the in-plane orthorhombic axes are 45 degrees rotated from the tetragonal axes and the unit cell is doubled. The Cu-Cu direction is then the $\mathbf{a}+\mathbf{b}$ direction. The crystal has a superlattice modulation which it thought to be driven by the mismatch of the bond lengths between the Bi-O layer and the Cu-O layer. This creates a buckling that modulates with wave vector $\mathbf{q_{sl}} = \pm 0.22\mathbf{b}^* \pm \mathbf{c}^*$.

5.2 Experimental Details

We present measurements at the copper K-edge of Bi-2212. Due to selection rules as discussed above, the linear dichroism at the K-edge comes from core 1s primarily probing the unoccupied p orbitals. The lowest order contributing terms of circular dichroism are $\mathbf{E1} \cdot \mathbf{E}2$ interference terms, which arise from intermediate states of

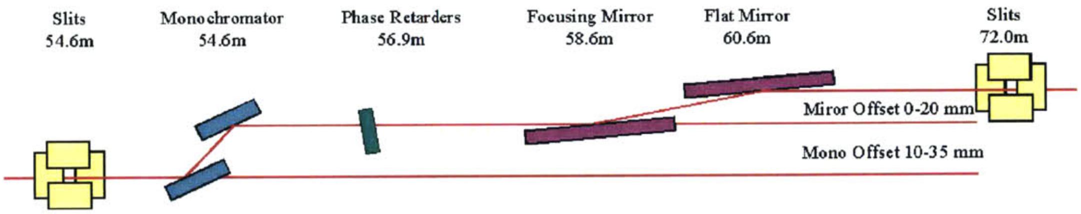

Figure 5-3: Schematic of the upstream optics. The beam travels through the white-beam slits, followed by a double-bounce Si(111) monochromator. The phase retarders are diamond. The first mirror is a toroidal focusing mirror, the second is a flat mirror. After the entrance slits, the beam enters the experimental hutch.

hybridized p and d orbitals.

The measurements were taken at Sector 4 ID-D at the Advanced Photon Source at Argonne National Laboratory. A schematic of the beamline is shown in Fig. 5-3. The undulators creates primarily horizontally polarized light. The further vertically shifted from the center of the beam, the more the polarization differs from purely horizontal. Upon entering the beamline, the x-rays go through a first set of slits, which reduces the size of the beam and reduces the variance in polarization. The monochromator is double-bounce, which allows for non-dispersive energy selection. The monochromator crystals are Si(111). The second crystal is detuned by 3 arc-seconds, which reduces the $\lambda/3$ contamination as the Si(333) reflection, which also satisfies the Bragg condition, has a sharper Darwin width. This is also true for all higher order reflections. The detuning reduces the measured beam intensity by about 30%. After the monochromator, the x-rays hit diamond phase retarders, which are used to control polarization. The details of these is discussed later.

After passing through the phase retarders, the beam hits two mirrors. The first is an adjustable palladium coated toroidal focusing mirror. The second is a flat silicon mirror. The beam has a 3.1 mradian incident angle, which corresponds to $E_{critical} = 9.876$ keV. Below this energy, the reflectivity is very near 1. Above, and it starts dropping rapidly. This mirror provides additional harmonic suppression. The beam then goes through a set of entrance slits, which clean up the bream.

After the entrance slit, the x-rays enter the experimental hutch. A schematic of

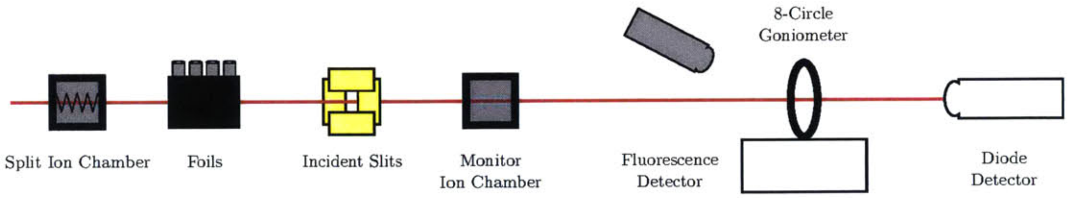

Figure 5-4: Schematic of the elements inside the experimental hutch.

the beam path is shown in Fig. 5-4. The beam first passes through through a split ion chamber, which is hooked up to a feedback loop that adjusts the mirrors to maintain the vertical beam position. Then there are a series of foils that are used to control the number of x-rays hitting the detectors. If the flux is too high, the detectors can experience saturation and non-linearities. Using the foils increases the relative amount of higher harmonics as lower energy x-rays are more strongly absorbed. Then the beam goes through the incident slits, the final slits, which are used to control the beam shape. Next is an ion-chamber, which is used as the monitor.

Finally, the beam hits the sample, which is mounted in a cryostat on an Huber 8-circle goniometer. The photodiode detector measures the x-rays that are transmitted through the sample. In addition, there is a fluorescence detector, which is energy resolved.

All K-edge dichroism measurements were taken on an underdoped sample of Bi2212 with $T_c = 82K$ and $T^* \sim 200K$. The sample, shown in Fig. 5-5 is 19 μm thick. Diffraction revealed the sample is monodomain in terms of the superlattice modulation.

5.3 Changing polarization

The x-rays coming out of the synchrotron are always horizontally linearly polarized (**E** in the horizontal plane.) To control the polarization, we use a phase retarder. In the x-ray regime, this is accomplished via effects derivable from dynamical diffraction theory, as originally proposed by Belyakov and Demetrienko[27]. Just off of Bragg scattering, dynamical diffraction theory shows that there is a difference in the index

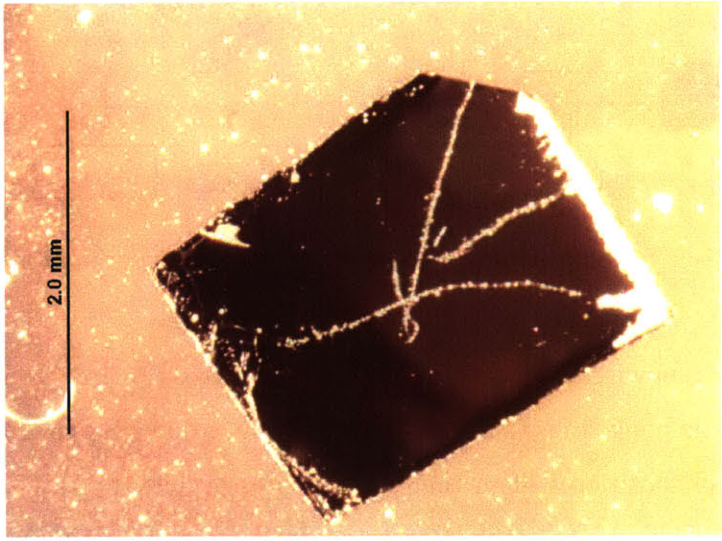

Figure 5-5: Photo of Bi2212 sample. T_c = 82K and $T^* \sim 200K$.

of refraction for π versus σ polarized light. This difference changes quickly around the Bragg peak and stabilizes into a broad plateau. For a given angular offset from the Bragg condition, the phase difference between π and σ light is determined by the thickness of the crystal.[44, 43, 42]

If the Bragg reflection occurs at 45 degrees to the polarization vector, the difference in the indices of refraction induces a polar type of rotation about the Poincare sphere. When the thickness of the crystal is such that the plateau corresponds to a phase difference between the two axes of $\pi/4$, the phase retarder is referred to as a 1/4 wave plate.

Figure 5-6 shows how a phase retarder can induces circular polarization from linear incident light. Figure 5-6 (B) shows schematically the different indices of refraction causing a fast and slow axis. The incident x-ray are directed into the page and the red line denotes the incident polarization.The offset determines which axis is fast, and which is slow.

Figure 5-6 (A) shows theoretical calculations made by Daniel Haskel for a 180μm silicon crystal, which is a quarter wave plate for energies near the Cu K edge. The phase difference caused by a small offset from the (111) Bragg reflection for 8.995 keV,

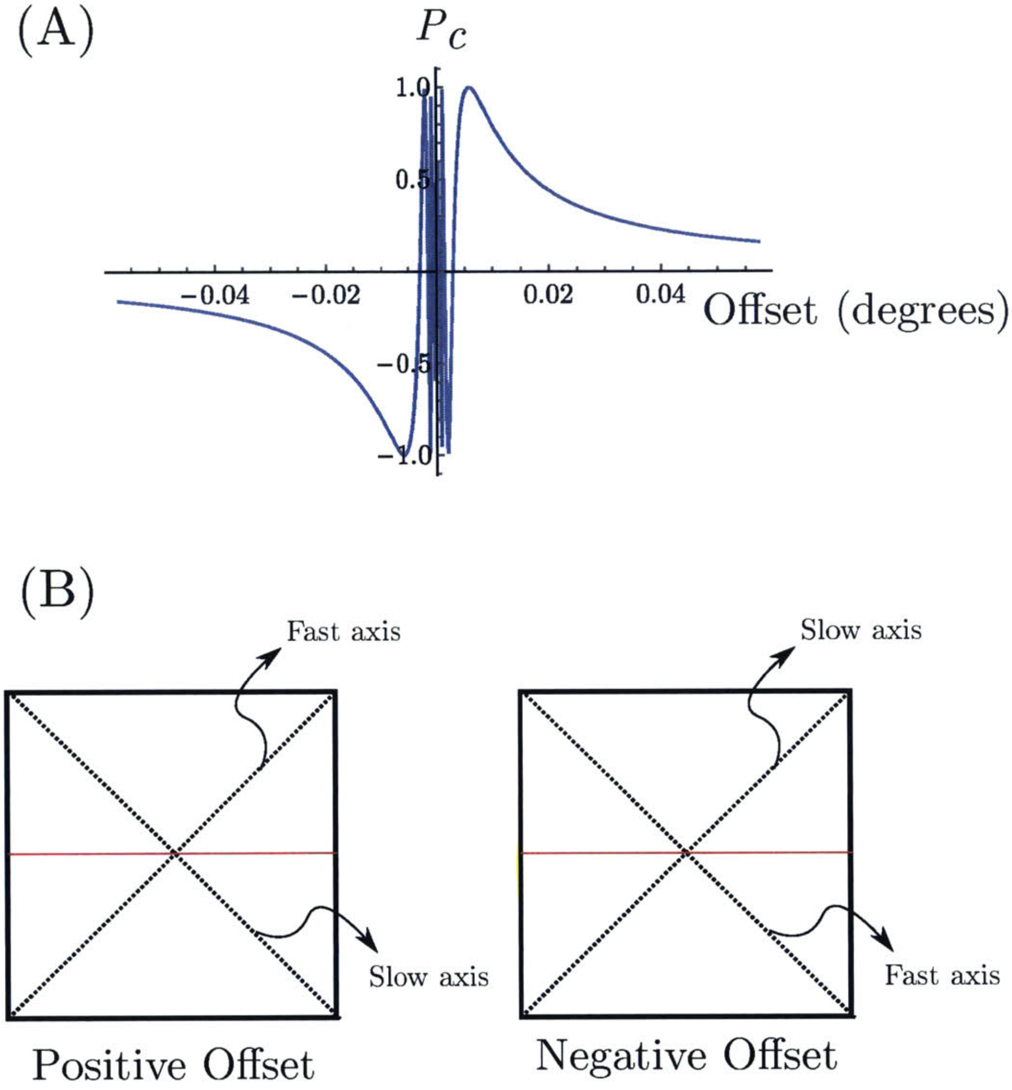

Figure 5-6: (A) Calculations made by Daniel Haskel of the theoretical degree of circular polarization as a function of offset in microns from the (111) Bragg peak of 180μm silicon. The sign P_c reflects the helicity of the circularly polarized light. (B) Schematic showing the relationship between the indices of refraction. The red line represents the linear polarization of the incident x-rays, which are directed into the page.

which is the Cu K edge in BSCCO, is calculated and transformed into the degree of circular polarization, P_c (see Eq. 4.12.) In principle, the offset should be rotational. However, due to the small nature of the angular offset, this is accomplished by making sub-micron adjustments in location using piezos. Theoretically, an offset of 0.057 degrees would yield perfect circular polarization. Because of divergence of the beam, however, the true polarization varies from the theoretical calculation.[7] Additionally, because of the rapidity with which the polarization changes below this value and the difficulty of achieving such consistent fine control of the piezos, we go above this value to 0.080 degrees to achieve a high degree of polarization with stability about small misalignments and divergences. Driving an oscillation between ±0.080 degrees with a square wave would produce x-rays alternating between left and right handed helicity with P_c of approximately 0.91.

It would be possible to obtain vertical polarization with a single phase retarder that is twice as thick. Instead, we do so with two 1/4 wave plates like described above. This is done because it allows for both rapid switching between vertical and horizontal polarization and provides for more similar intensities between the two polarizations.

In terms of a Poincare sphere, vertical polarization can be obtained by making two identical polar rotations of 90 degrees. Each rotation, by itself, would turn a horizontally polarized beam to circularly polarized. Combined, they switch the polarization all the way to vertical. When the same two phase retarders rotate in opposite directions, the beam remains horizontally polarized (e.g. the first phase plate turns horizontal polarized to circular, and the second rotates it back.) Thus rapid switching can be achieved through the same procedure of driving one phase plate while the other is stationary.

For our measurements of linear dichroism, we used a phase plate that had not been well characterized before. In order to do quick checks of the polarization, we used two diode detectors placed after the phase plates. The one diode is horizontally to the side of the beam; the other is directly below. A small piece of aluminum is placed into the beam. The x-rays induce Thompson scattering. Horizontally polarized light will preferentially induces vertical scattering and thus the vertical diode will see more

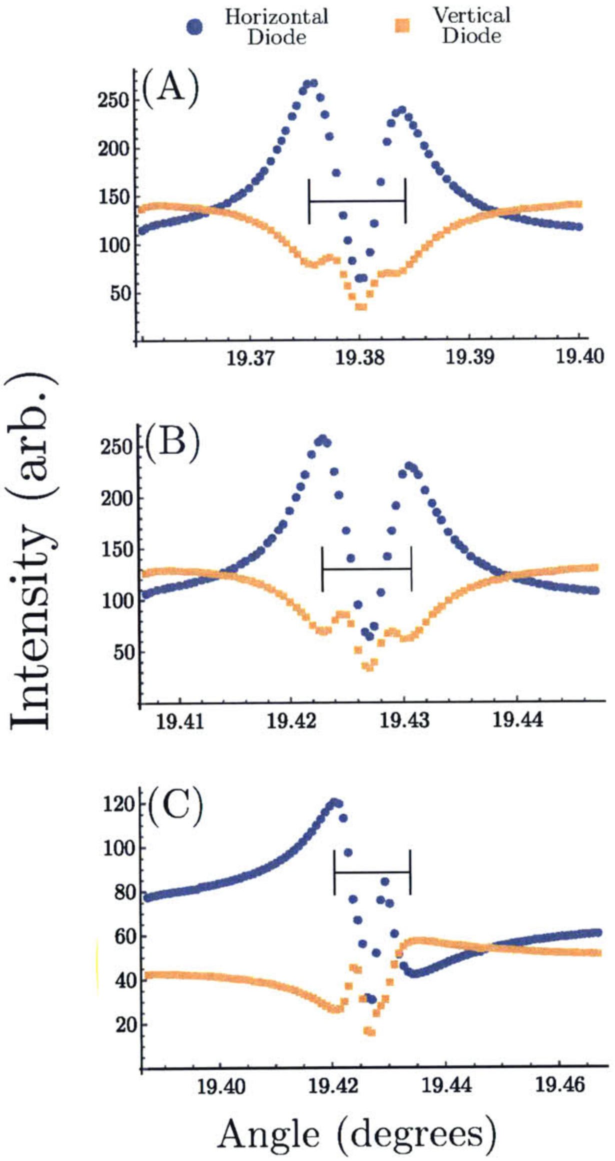

Figure 5-7: Measurement of the Thompson scattering from aluminum as the phase plates theta angles are scanned. The horizontal (vertical) diode measures maximal intensity when x-rays are vertically (horizontally) polarized. In (A) and (B), each of the two phase plates are individually scanned. The width between the two vertical polarization peaks (horizontal polarization minima), as shown in the black bar, is approximately the same as the angular offset from the Bragg condition to obtain circular polarization. In (C), the first phase plate produces circularly polarized x-rays and the second phase plate is scanned. The black bar shows the amplitude of oscillation necessary to obtain vertical and horizontal polarization.

intensity. Similarly, vertically polarized light will preferentially induce horizontal scattering and thus the horizontal diode will see more.

The result of these calibration scans are shown in Fig. 5-7. When the horizontal (vertical) diode has maximal intensity, the light is predominantly vertically (horizontally) polarized. Fig. 5-7(A) and (B), are theta scans of individual phase plates. The center (minima) of each scan is when the phase plate satisfies Bragg scattering. The width between the two vertical polarization peaks (horizontal polarization minima) is approximately the same as the angular offset from the Bragg condition to obtain circular polarization. In Fig. 5-7(C) the first phase plate is set to produce circular polarization while the theta angle of the second phase plate was scanned. Piezo crystals were set to oscillate at the width between maximally vertical and maximally horizontal for linear dichroism scans.

5.4 Normalization and Signal Intensity

Absoprtion process leads to attenuation of the x-rays as defined by

$$I = I_0 \, \mathrm{e}^{-\mu t} \tag{5.1}$$

where I is the final intensity, I_0 is the initial intensity, μ is the absorption coefficient, ant t is the thickness. Experimentally, we measure the initial intensity through a monitor, which is a thin solid-state detector and the final intensity, a thick solid state detector. To determine the absorption coefficient, we have

$$\mu t = \log\left(\frac{I_0}{I}\right) = \log\left(\frac{monitor}{detector}\right) + cons. \tag{5.2}$$

where the constant contains all the non-physically relevant quantities such as differences in gains and detector efficiencies. The left hand side of the equation includes the thickness of the sample. Though this can be measured, a more standard way to display the data is to scale and normalize the data.

To normalize the data, we follow the standard procedure for dichroism measurements, which is shown in Fig. 5-8. The exact energy of the absorption edge is defined as the maximum of the first derivative. For elemental copper, this is 8.979 keV. For BSCCO, we measured the edge to by 8.995. This sort of edge shift is typical for copper in oxide materials.

The pre-edge and post-edge regions are fit to a line. The pre-edge absorption is the absorption from all other process in this energy region other than the copper K-edge. The post-edge region consists of absorption processes that include K-edge excitations, but the excited electron is no longer probing unoccupied atomic orbitals of the copper atoms. This is shown in Fig. 5-8(B) The difference between these two fits at the edge is scaled so that the edge jump to 1. This scaling is equivalent to what the measured data would be if the sample thickness was $1/\mu$ at the edge. All presented absorption data has the pre-edge fit subtracted off and scaled. The final result of this normalization procedure is shown in Fig. 5-8(C).

In principle, absorption data for a known thickness can be used to determine the absorption cross-section as $\sigma \equiv \mu\rho t$. However, in practice, determining the absolute intensity is quite challenging. The biggest difficulty is accurately fitting and extrapolating the pre and post edge regions. By performing this over a series of absorption scans, we see variance over the scale factor for the edge jump on the order of 10%. Thus all numerical values in our absorption are only correct within that systematic error on the normalization. All of our data are normalized identically and so can be directly compared.

The most physically relevant expression of the dichroism is

$$\Delta\mu(\omega) = \frac{\mu_+(\omega) - \mu_-(\omega)}{\int_{Edge} \mu_+(\omega) + \mu_-(\omega) \mathrm{d}\omega} \tag{5.3}$$

where the integral in the denominator is over the entire edge. This form necessary to apply sum rules to the dichroic signal. Conventionally, it is shown as

$$\Delta\mu(\omega) = \frac{\mu_+(\omega) - \mu_-(\omega)}{\mu_+(\omega_{edge}) + \mu_-(\omega_{edge})} \tag{5.4}$$

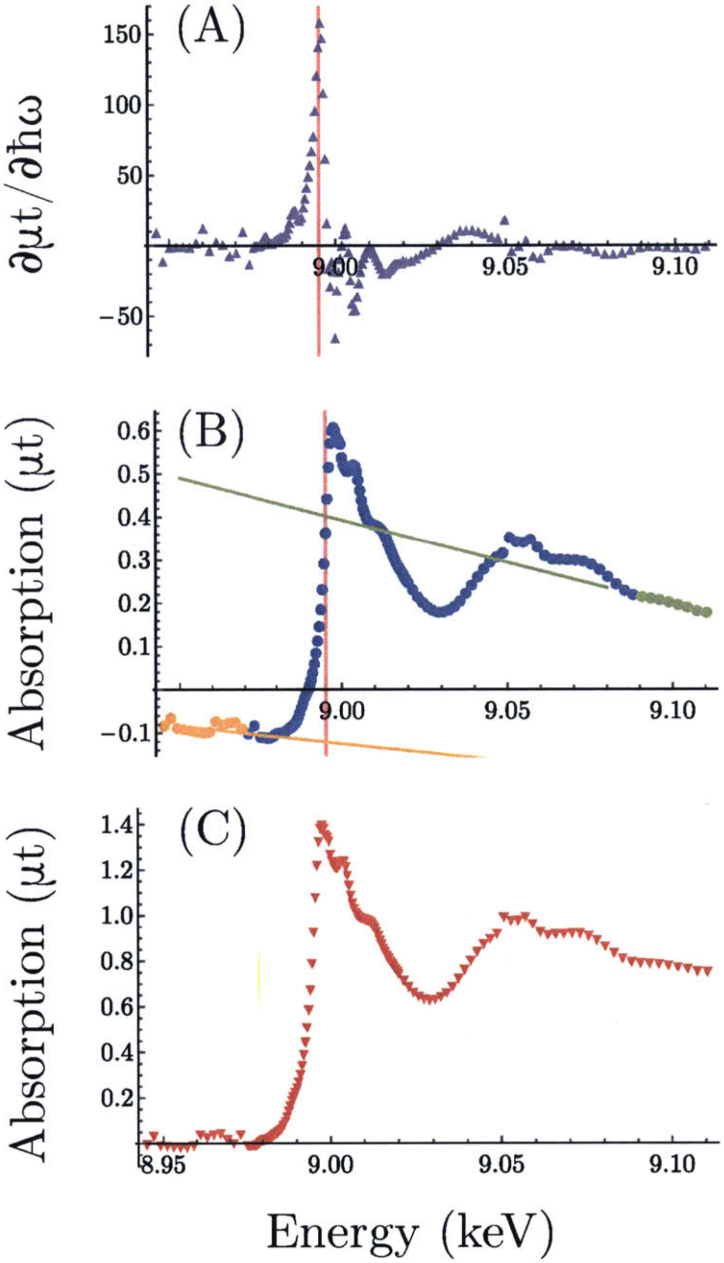

Figure 5-8: Demonstration of the normalization procedure. (A) shows the numerically calculated derivative from the absorption data. The edge is defined as the maximum of the first derivative, as shown in solid red line. (B) shows the raw absorption data with linear fits to the pre-edge and post-edge regions. The difference between these extrapolated fits at the edge defines the edge jump. The data are scaled so this jump is equal to unity. The final absorption, shown in figure (C) is the raw data, minus the extrapolation of the pre-edge and scaled.

where the denominator denotes the edge jump. Since we have normalized this to be 1, the denominator is exactly unity. We follow convention and show our dichroism as

$$\Delta\mu t_{Dichroism} = (\mu_+ - \mu_-)t \tag{5.5}$$

5.5 K Edge Circular Dichroism Results

For circular dichroism measurements, the single phase plate was driven with a 13.1 MHz square wave. The log of x-ray detector and monitor was fed into a lock-in amplifier. Fig. 5-9 shows a representative scan for incident x-rays parallel to the c axes. The red data shows the average signal, which corresponds to the absorption. The blue show the signal that oscillated at 13.1 MHz and is the dichroic signal. Both the dichroism and absorption have been normalized. The error bars are from estimates of statistical fluctuations from counting statistics only and, for the dichroic signal are roughly the size of the markers. For the absorption, the statistical fluctuate are negligibly small as count rates were thousands of counts per second.

Before the copper edge there is no dichroic signal. Slightly below 8.99 keV is a small positive bump, followed by a small dip. Right near at the edge is a large positive peak and a negative valley. In the post-edge region, the features were not as reproducible and are obscured by changing backgrounds, which are not fully characterized. The one anamolously high point at 9.017 is likely from Bragg scattering of an optical element or detector.

Fig. 5-10 shows a schematic of the alignment of the crystal relative to the laboratory frame. In order to eliminate the possibility that the signal we measured was truly circular dichorism, it was necessary to measure the dependence of the signal on rotation about the c axis. To be precise with our orientation, we aligned the crystal with diffraction. We introduce the ψ to denote the azimuthal angle for rotations that preserve the x-rays incident along the c axis. We defined $\psi = 0$ when the crystal a axis is horizontal in the lab frame and the b axis is vertical. ψ then denotes the angle between the crystal a axis and the laboratory x axis such that $\psi = 90$ corresponds

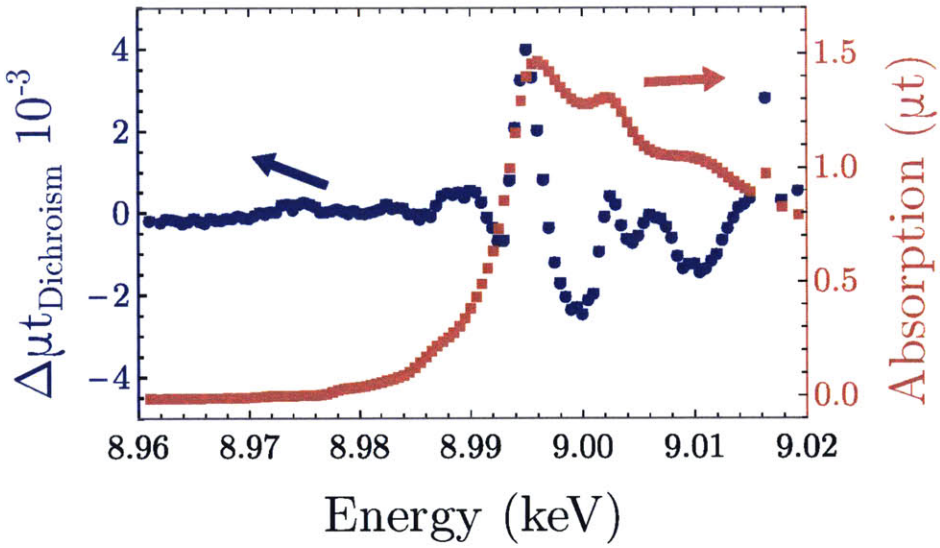

Figure 5-9: Plot of a typical dichroism scan taken with a lock-in amplifier. The phase retarders are driven with 13.1 Hz square wave. The absorption, shown in red on the right scale, is the time averaged over each energy step. The dichroism is measured from the lock-in amplifier and is shown in blue on the left scale. The most conspicuous feature of the dichroism is small down turn at 8.993, a sharp positive peak at 8.995 keV, and a negative peak just below 9.00 keV. Statistical errors from counting statistics are small relative to the point size.

to a 90 degree rotation about the c axis, placing a vertical and b horizontal.

Additionally, we can measure the polar dependence of the signal. Such a rotation is accomplished by a θ motor rotation, which rotates about the horizontal axis. For polar scans, the incident x-rays are no longer along the c axis.

In Fig. 5-11, the dichroic signal at $\psi = 45$ and $\psi = 90$ are compared. As Bi-2212 is orthorhombic, any structural linear dichroism is expected to be maximal $\psi = 90$, which directly compares the absorption along the orthorhombic directions. As light polarized along the (110) or $(1\bar{1}0)$ directions can be equally decomposed to light along the a and b axes, the linear dichroism at $\psi = 45$ is expected to be minimal. As shown in the figure, the is almost no dichroic signal at $\psi = 45$, which is suggests the signal seen at $\psi = 90$ is linear in origin.

In order to confirm the linear origin of the signal, we mapped out the full azimuthal rotational dependency. To asses the intensity of the signal, we created an integrated intensity measure, defined as

$$I_{integrated} = -\int_{8.992}^{8.9975} \Delta\mu t(\hbar\omega)\, d\omega + \int_{8.9975}^{9.003} \Delta\mu t(\hbar\omega)\, d\omega \tag{5.6}$$

This is accomplished in arbitrary units by summing the data points in the integration regions. Because the regions are the same size, the measure is invariant to a constant background. Fig 5-12(A) shows the regions of integration. Fig 5-12(B) shows the intensity measure of dichroism as a function of azimuthal angle. Errors are from counting statistics only. The curve is a fit to $cos(2\psi)$, which is the expected dependency for linear dichroism. The success of this fit is indicative of linear dichroism.

For $\psi = 45$ at 30K, there is a small bump at 8.995keV, which is possibly from XNCD. The azimuthal dependence of a mixture of XNCD and linear dichroism should follow a sinusoidal plus constant dependency. A fit to such a model to the integration data does not lead to a constant value that is statistically significant from zero, which demonstrates that there is no XNCD signal on top of the linear dichroism.

Additionally, to test whether this signal is from truly circular dichroism, we investigate the signal as a function of temperature, shown in Fig. 5-13. At both 60K,

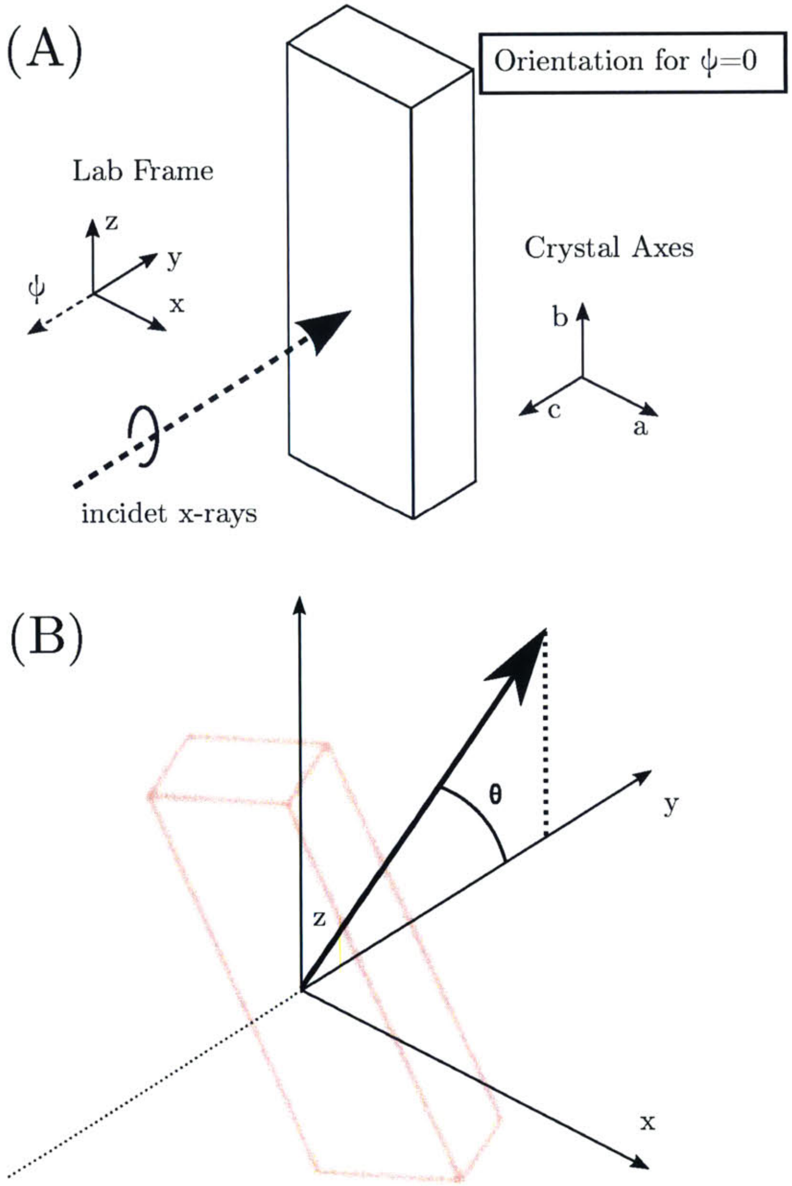

Figure 5-10: The majority of measurements were taken with the x-rays injected parallel to the crystallographic c-axis. (A) shows this schematically. The laboratory axes are such that the x-rays propagate along the laboratory y-axis. When the crystal is aligned with ψ=0, the crystallographic b-axis is along the laboratory z. The ψ rotation axis is along negative y, such that when ψ=90, the a-axis is along laboratory z. (B) shows what is meant by a polar rotation, for which the x-rays are no longer parallel to the c-axis.

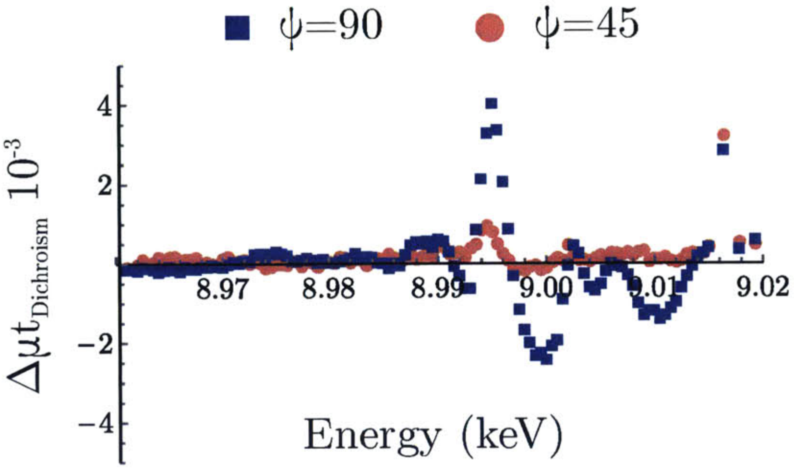

Figure 5-11: Comparison plot of $\psi = 45$ and ψ=90 dichroism. The rotational dependence of the peaks in the dichroic signal precludes a difference between absorption of left and right-handed circularly polarized light as being the source.

which is still below T_c, and 100K, which is still below T^*, it is possible the same bump exists, but it the affect is clearly small relative to the statistical and systematic noise. From this data as well as the azimuthal data, there is no evidence for XNCD. It is possible it exists, but could only be measured with improved signal-to-noise.

5.6 K Edge Linear Dichroism

In addition to the data with circularly polarized light, we studied the linear dichroism. Unlike for the circular measurements, we did not do a full diffraction alignment. We only aligned the c axis by finding (00L) diffraction peaks. This allows us to guarantee the x-rays are incident parallel to c, but the in-plane alignment is done by eye, estimated to e accurate to ± 3 degrees. For all measurements, we present normalized dichroism measurement of vertically polarized light minus horizontally polarized light. The orientation is the same as defined in Fig. 5-10. Thus, at $\psi = 0$, the linear dichroism is measuring the difference in absorption between (100) and (010); at $\psi = 45$ it is the difference between (110) and $(1\bar{1}0)$.

Fig 5-14 shows the dichroism at 30K for linear x-rays incident along the c axis,

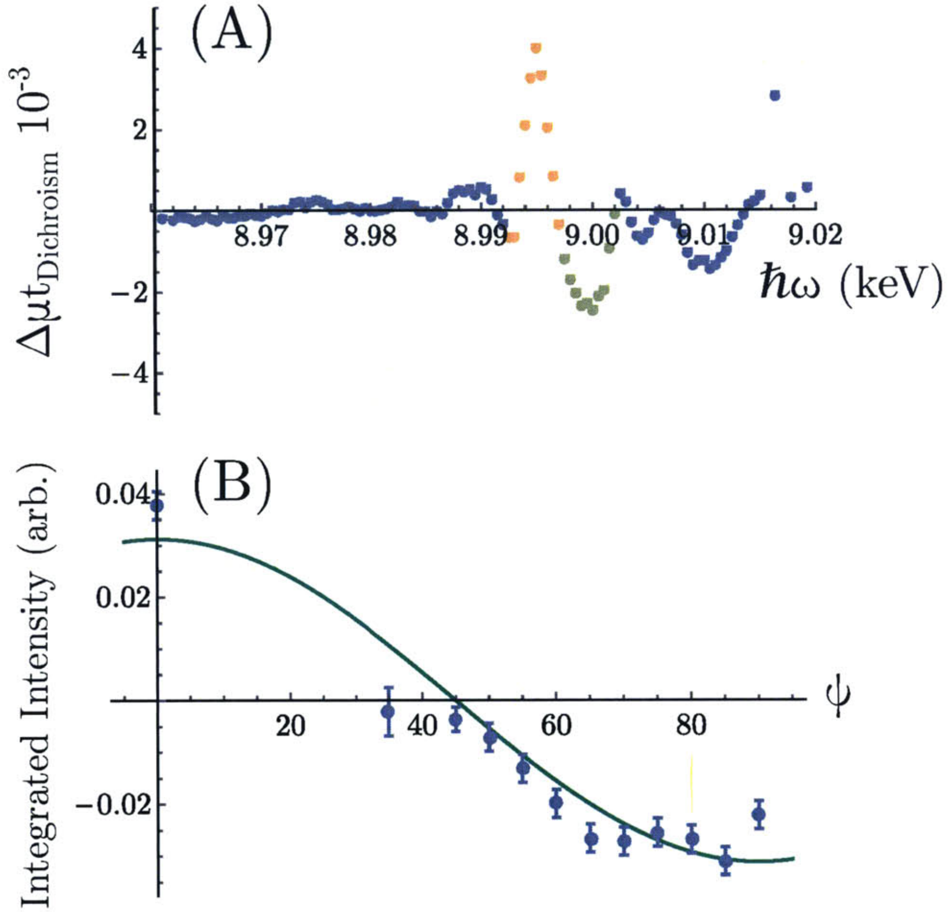

Figure 5-12: To systematically investigate the azimuthal dependence, we created a integrated measure of the two key peak features. In (A), the dichroism is shown when the azimuthal angle ψ is equal to 90 degrees. The two peaks are highlighted in orange and green. The integrated measure come from the sum of the data points in each region, with the orange data counting negatively. The azimuthal dependence of the integration are shown in (B). The green line is a fit to $\cos 2\psi$.

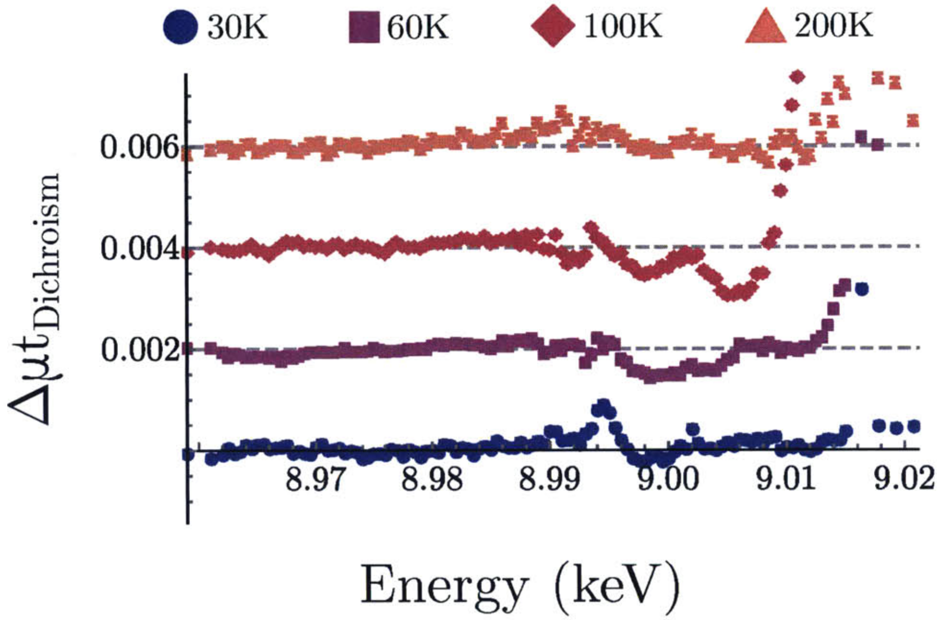

Figure 5-13: Temperature dependence of $\psi = 45$ circular dichroism. Different temperatures are vertically offset for clarity. In the 30K scan, there is a slight bump at 8.995keV. It is possible this is from truly circular dichroism. However, it does not appear at any other temperatures, even those below T_c and T^*. If there is any circular dichroism, it is small relative to our statistical and systematic noise.

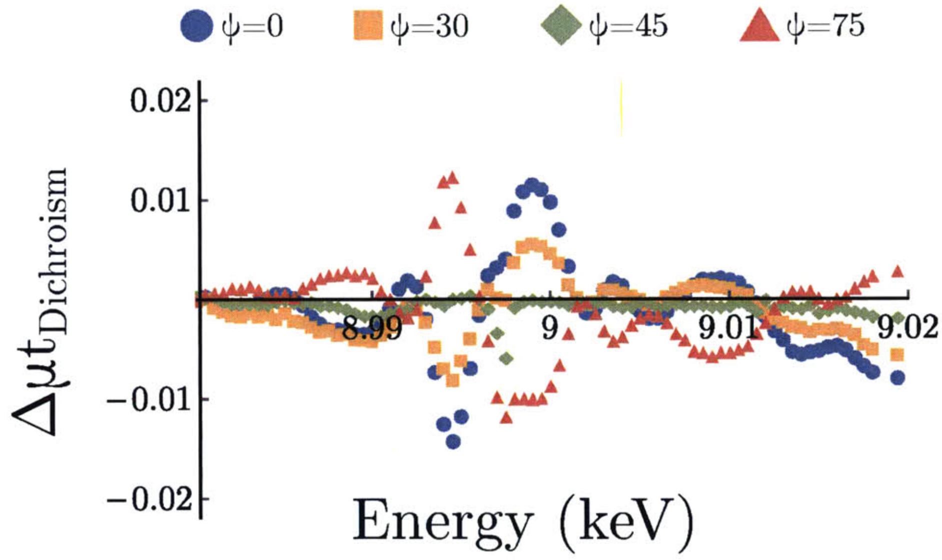

Figure 5-14: Linear dichroism measurements at 30K for several different angles (degrees). The flipping of sign of the sign of the two peaks at 8.99 and 8.995 keV at $\psi = 45$ is as expected for linear dichroism.

for several different azimuthal angles. The location and shape of the main peaks, at 8.995keV and 8.999keV is the same as seen with circularly polarized light. This clearly shows that the signal is driven by linear bleed-through. The azimuthal dependence appears to follow the expected behavior for linear dichroism: it decreases near zero at $\psi = 45$ and the data for $\psi > 45$ is opposite in sign from data for $\psi < 45$.

More quantitatively, the azimuthal dependence can be studied by using the integrated intensity measure defined in Eq. 5.6. This is shown in Fig. 5-15. The error in the integrated intensity comes from the estimate of x-ray count fluctuations only. The integrated intensity is fit to cosine function with an amplitude and offset. The data match the fit line remarkably well. The error on the offset is really driven by the lack of precision in alignment, which we estimate to be $\sim$3 degrees. Within this error, the offset is zero.

This is a significant distinction from what is seen in THz spectroscopy on YBCO, which sees birefringence and dichroism that is about 10 degrees offset from the symmetry axes and necessitates a breaking of C4 and mirror symmetries. The polarization rotation angle is maximal when the electric field is about 35 degrees rotated from the Cu-O bond direction. Multiple coexisting effects along different high-symmetry directions are likely the cause of the maximal signal being off a symmetry direction. The real part of the rotation angle with electric field angle ϕ is related to the dichroism between $\phi \pm 45$. Therefore the maximum dichroism is seen 10 degrees rotated from the Cu-O bond. [61] We see dichroism maximally exactly along the orthorhombic a and b axes, which is 45 degrees rotated from the Cu-O bonds. Beyond the specifics of the material, there are key physical differences to the experimental measurements. First, K-edge dichroism a local probe and copper specific. Second, it sensitive only of the unoccupied states and predominantly only the p states as the excited election comes from the copper 1s core states. THz spectroscopy is sensitive to affects in both the itinerant valence and conduction bands of all orbitals from all the elements in the system.

To determine if the linear dichroism is related to the pseudogap, we investigate the temperature dependence of the signal. Fig. 5-16 shows the dichroism at various

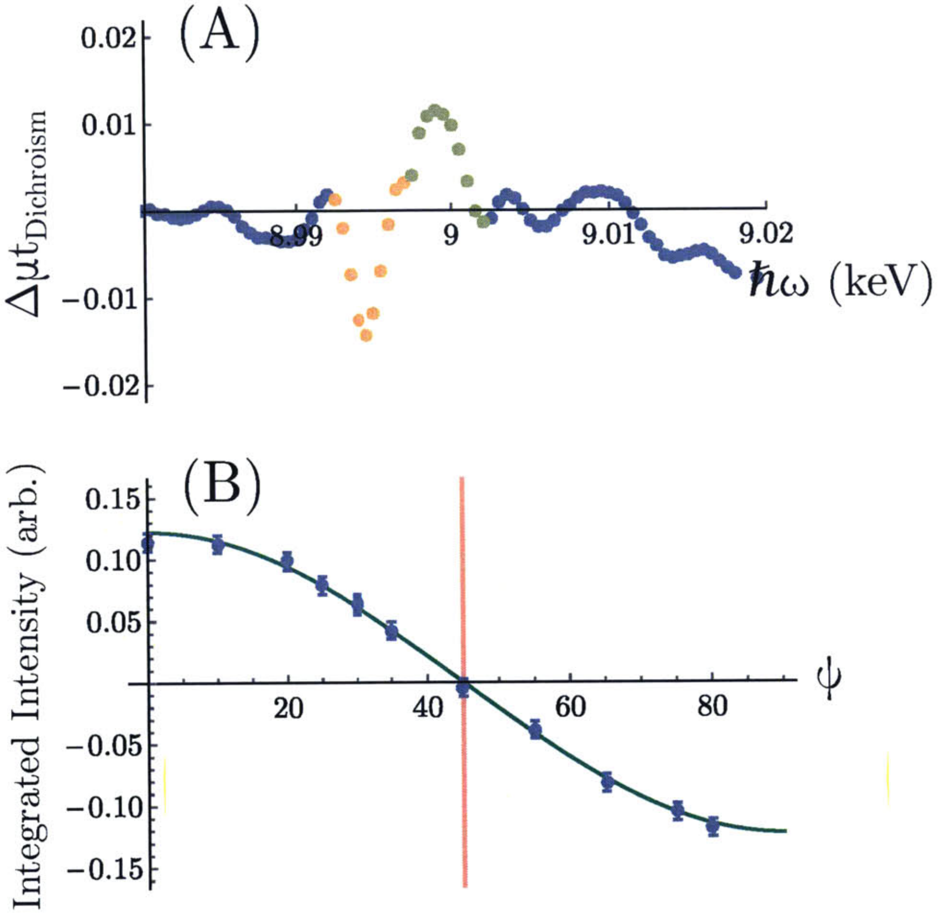

Figure 5-15: In (A), the dichroism is shown when the azimuthal angle ψ is equal to 0 degrees.The integration regions highlighted in green and orange are the same as in Fig. 5-12. The azimuthal dependence of the integration are shown in (B). The green line is a fit to $\cos 2(\psi - \psi_0)$. The fit value of ψ_0 is 0.07±0.67. As the crystal was not fully diffraction-aligned, the true error bar is from the ability to align the crystal by eye, and is likely ~3 degrees

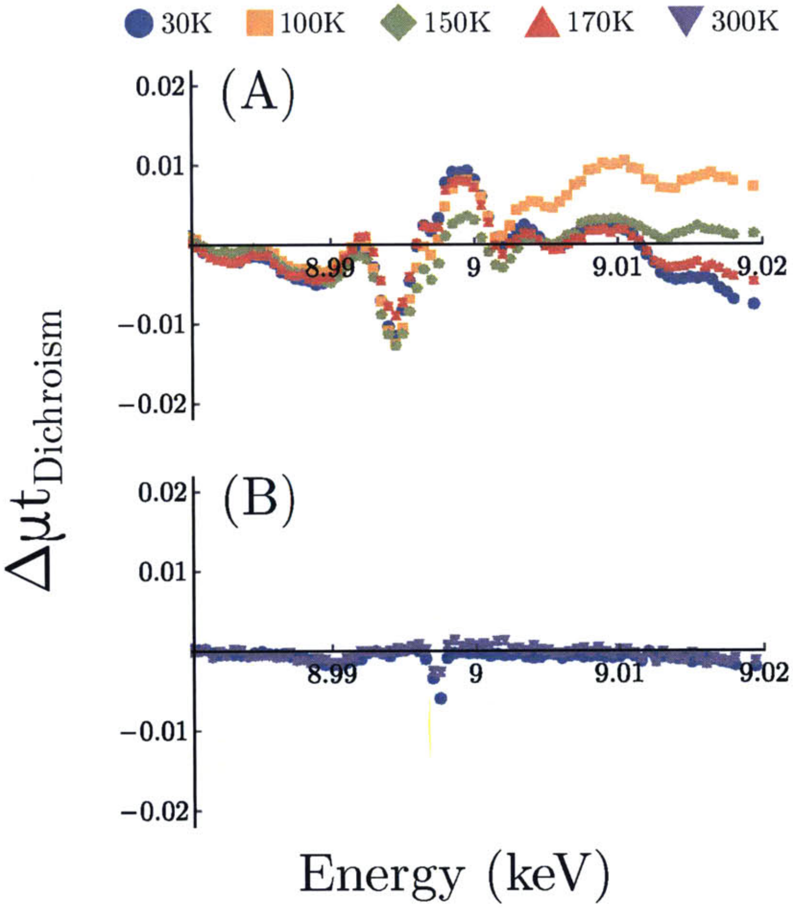

Figure 5-16: Temperature dependence for in plane dichroism at (A) ψ=20 degrees and (B) ψ=45 degrees. The main peaks at 8.995 and 8.999 keV show very little temperature dependence.

temperatures at (A) $\psi = 20$ and (B) $\psi = 0$. As seen in the raw data, there does not appear to be any significant change as a function of temperature at these orientations.

A more thorough temperature investigation was performed at $\psi = 0$, which is where the maximal signal is seen. The data are shown in Fig. 5-17. For each scan, the pre-edge region is fit to a constant background and subtracted off. The primary dip and peak features, highlighted in orange and green, are seen at all temperatures.

Using the same integrated intensity measure as before, we can try to investigate the signal more quantitatively. This is shown in the blue data in Fig. 5-18(B). This simple measure shows a scattershot of temperature dependence. In fact, the dominant affect is actually the correlation with when the data were taken: earlier data had a higher integrated intensity than later data. This suggests that there was a systematic change to the background as a function of time. The changing background is apparent in the data in Fig. 5-17. The next level correction is to add a linear term to the background. This is accomplished by creating a line connecting the data point right before the orange integration regions starts to the data point right after the green integration region ends. This is shown in red in (A). The integrated intensity after accounting for this changing linear term is shown in yellow in (B).

After accounting for a changing linear background, it appears that there might be a slight decrease in integrated intensity as a function of temperature. At this point, however, the data are insufficient to make any firm conclusions. Follow-up measurements are needed. In particular, it would be very useful to compare the intensity at each temperature at $\psi = 0$ and $\psi = 90$ as the true signal should be inverted while the background intensity would change only from small changes in the region of the sample irradiated by x-rays.

The intensity of the in-plane linear dichroism is surprisingly high. Though the crystal is orthorhombic, and so linear dichroism is expected, the local environment around the copper atoms is typically thought of and treated as tetragonal at the copper sites. Our measurements show significant deviation from tetragonal symmetry. Because our signal is maximal precisely at $\psi = 0$, we see no evidence for breaking of mirror symmetries.

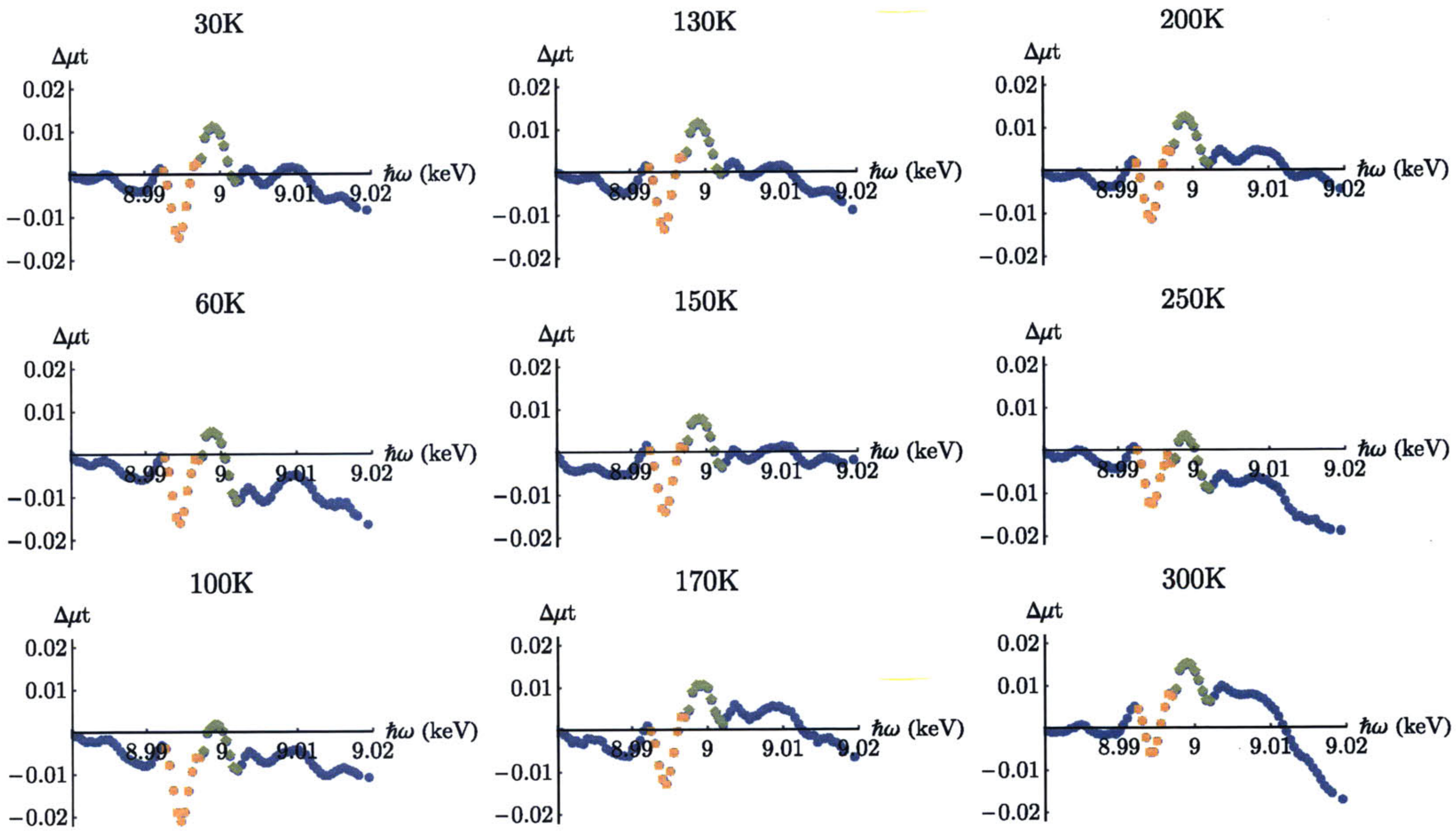

Figure 5-17: Linear dichroism from all temperatures at ψ=0. Data have a constant background fit from the pre-edge region subtracted. The integrated regions are shown in orange and green. The raw data suggest additional background terms, especially a linear component at the integration region. These additional background terms do not seem to have a clear temperature dependence.

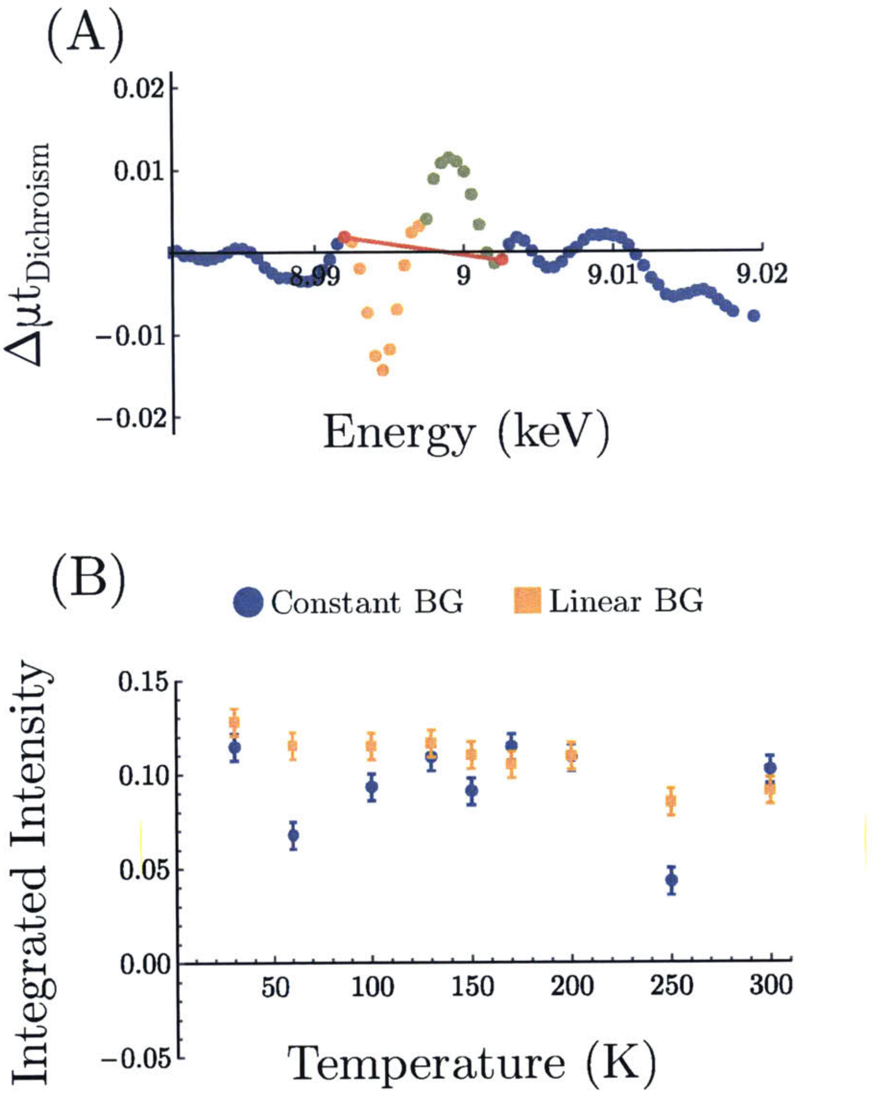

Figure 5-18: Temperature dependence for in plane dichroism evaluated ψ=0. Due to clear variations of the background, we evaluated the integrated intensity for a constant background and a linear background. (A) shows the integrated regions in orange any green. The red line is a linear interpolation from the first data points outside the integration region. (B) shows the integrated intensity as a function of temperature. Errors are from statistical fluctuations from count rates only and do not include estimates for the changing background.

5.7 Polar tilt data

In addition to measuring the dichroism with x-rays incident along the c axis, we can introduce a polar tilt. This is done at $\psi = 45$ degrees so there is no signal from the in-plane dichroism discussed above. These measurements were taken with both circularly and linearly polarized x-rays.

Linear dichroism between the c axis and the in-plane direction should scale as

$$I_{Dichroism}(\theta) = I_0 \sin^2(\theta) \tag{5.7}$$

where θ is the polar tilt and I_0 is the full dichroism measured for x-rays incident on $(1\bar{1}0)$ and linear polarizations along (001) and (110).

Some theoretical models predict non-trivial XNCD, but due to symmetries of the crystal other than inversion, the signal is precisely zero for x-rays incident along the c axis.[26] For circularly polarized x-rays, the scaling seems close to accurate. This suggests that the signal seen is the result of linear bleed through and not intrinsic circular dichroism. This conclusion is bolstered from the similarities in the raw data dichroism location for circularly and linearly polarized x-rays. The scaling for the linear x-rays matches very well. It should be noted that the polar tilt changes the effective thickness of the sample. Thus, the normalization must be done independently for each polar tilt. This is likely the dominant affect that reduces the precision of the scaling.

Finally, it is useful to compare the polar tilt data to the previous experimental data from Kubota et al.[54] This data scaled is plotted on top of the data in Fig. 5-19(B). The location and width of the peak seen are fairly similar. The additional structure we measure for linearly polarized x-rays is likely due to our increased signal to noise as well as slight differences in normalized intensities in the pre-edge region from measuring in transmission as opposed fluorescence, which was used by Kubota.

In order for the Kubota data to be approximately the same intensity as our scaled data with circularly polarized x-rays, we had to scale it by a factor of 525. This scale factor the same as $1/\sin^2(2.5)$. Thus, we would have measured very similar signal

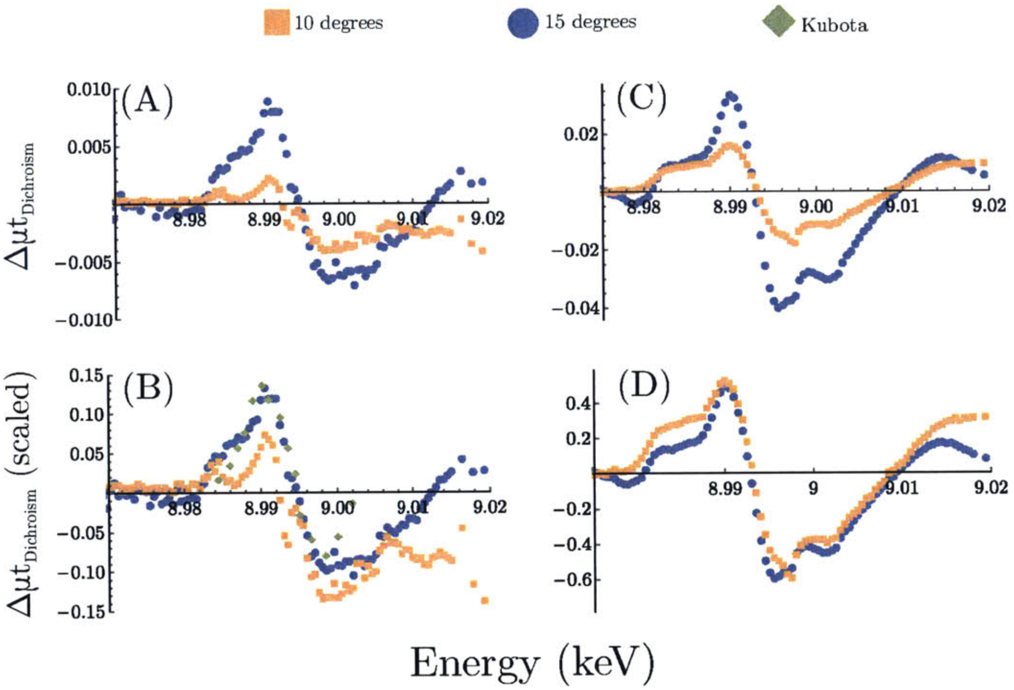

Figure 5-19: Dichroism from a polar rotation. Data is taken with $\psi = 45$, so there is no in-plane dichotic signal. (A) and (B) are data from circularly polarized x-rays. (C) and (D) are with linearly polarized x-rays. In figures (A) and (C), the dichroism is shown with a constant pre-edge background subtracted. In figures (B) and (D), the data are scaled by dividing by $\sin^2(\theta)$, where θ is the polar rotation angle. This is the geometric scaling expected for dichroism between the c axis and the in-plane (110). On the same plots is the peak from the work by Kubota et al.[54] The Kubota data is scaled to match intensities. The multiplicative factor to match the intensity of circularly polarized data is consistent with the intensity we would measure with a ~2.5 degree polar misalignment.

as reported by Kubota if we had a 2.5 degree misalignment. This fact, combined with the lack of any detectable XNCD signal suggests that misalignment is likely the source of reported XNCD.

5.8 Intensity and Polarization Control

It is clear from above that the measured dichroism when using circularly polarized x-rays comes from imperfect polarization and significant linear bleed-through. In Fig. 5-20 we plot the dichroic signal from both circular and linearly polarized x-rays.For linearly polarized x-rays, the data are taken at $\chi = 90$. For comparison with circularly polarized x-rays, we chose to use $\chi = 0$ data instead of $\chi = 90$ because the counting time was long here. The circularly polarized dichroism was inverted, to account for the different orientation, and scaled by a factor of 4. The scale factor is a measure of the linear bleed-through compared to the degree of linear polarization switching. This factor is remarkably low and suggests that polarization control using phase plates leads to significant systematic errors and spurious conclusions from incomplete polarization.

5.9 Conclusions

From our investigation of copper K-edge dichroism in the pseudogap of Bi-2212, we discovered no evidence of the XNCD signal. Using circularly polarized x-rays to measure the dichroism under a polar tilt, such that the x-rays were incident off the c axis, we obtained a signal that had the same peak locations and shape as the reported XNCD signal reported by Kubota et al.[54] We showed that this signal is in fact the result of linear x-ray bleed through. As a result, we were able to determine that an angular misalignment of only ~2.5 degrees would have given us a signal of comparable magnitude to the previously observed data, which was thought to be XNCD. We therefore conclude that a misalignment is the most likely source of their signal. We do not, however, see any temperature dependence to this dichroism. This is

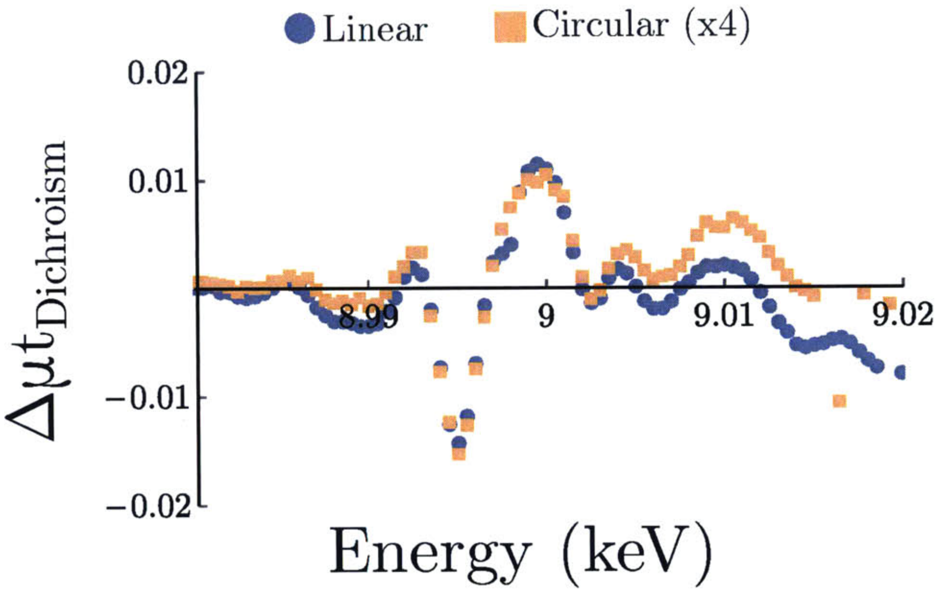

Figure 5-20: Comparison of data taken with linear polarized and circularly polarized x-rays. The blue circles show the data taken with linearly polarized x-rays at ψ=0. The yellow squares show the data with circularly polarized x-rays at ψ=90, scaled by a factor of 4. This scan is also inverted for ease of comparison of the intensities. The scale factor of 4 demonstrates that even with significant effort and care to maximize the degree of polarization in circular dichroism measurements, significant linear dichroism is measured.

in disagreement with the work by Kubota et al. We hypothesize that their alignment coincidentally changed as they swept in temperature that gave a specious result.

We also measure a strong in-plane linear dichroism. This necessitates significant deviation from local tetragonal symmetry at the copper atoms. Because the signal is maximal when the **E** field is exactly along the orthorhombic a and b axes, there is no evidence for breaking of mirror symmetries, as is necessitate by the THz dichroism measured in YBCO.[61] Additionally, the THz measurements sees maximal dichroism near the Cu-O bond, while the K-edge linear dichroism is maximal 45 degrees rotated from these bonds.

Finally, we compared the intensities of linear dichroism measured with x-rays with a high degree of linear polarization and with a high degree of circular polarization. The resulting signals were only different by a factor of 4. This suggests that current technology makes the removal of linear affects when measuring circular dichroism challenging. Therefore, it is vital that any investigation of XNCD ensure that the existence of any signal is seen at all azimuthal angles. If XNCD and linear dichroism are simultaneously present, the azimuthal dependence should be sinusoidal with a constant offset. A more promising alternative way to eliminate the possibility of linear affects would be to look for XNCD in the pseudogap of truly tetragonal crystals.

Bibliography

[1] Lucilla Alagna, Tommaso Prosperi, Stefano Turchini, José Goulon, Andrei Rogalev, Chantal Goulon-Ginet, Calogero R Natoli, Robert D Peacock, and Brian Stewart. X-ray natural circular dichroism. *Physical Review Letters*, 80(21):4799, 1998.

[2] H Amitsuka, M Sato, N Metoki, M Yokoyama, K Kuwahara, T Sakakibara, H Morimoto, S Kawarazaki, Y Miyako, and J A Mydosh. Effect of pressure on tiny antiferromagnetic moment in the heavy-electron compound URu2Si2. *Physical Review Letters*, 83(24):5114, 1999.

[3] P Aynajian, T Keller, L Boeri, S M Shapiro, K Habicht, and B Keimer. Energy Gaps and Kohn Anomalies in Elemental Superconductors. *Science*, 319(5869):1509–1512, March 2008.

[4] K Behnia, R Bel, Y Kasahara, Y Nakajima, H Jin, H Aubin, K Izawa, Y Matsuda, J Flouquet, Y Haga, Y Onuki, and P Lejay. Thermal Transport in the Hidden-Order State of URu2Si2. *Physical Review Letters*, 94(15):156405, April 2005.

[5] Romain Bel, Hao Jin, Kamran Behnia, Jacques Flouquet, and Pascal Lejay. Thermoelectricity of URu2Si2: Giant Nernst effect in the hidden-order state. *Physical Review B*, 70(22):220501, December 2004.

[6] K Berggold, T Lorenz, J Baier, M Kriener, D Senff, H Roth, A Severing, H Hartmann, A Freimuth, S Barilo, and F Nakamura. Magnetic heat transport in R2CuO4 (R=La, Pr, Nd, Sm, Eu, and Gd). *Physical Review B*, 73(10):104430, March 2006.

[7] R Boada, M A Laguna-Marco, and J A Gallastegui. X-ray magnetic circular dichroism measurements using an X-ray phase retarder on the BM25 A-SpLine beamline at the ESRF. *Journal of synchrotron …*, 2010.

[8] C J Bonnoit, D R Gardner, R Chisnell, A H Said, Y Okada, T Kondo, T Takeuchi, H Ikuta, D E Moncton, and Y S Lee. Probing electronic order via coupling to low energy phonons in superconducting $\mathrm{Bi_2Sr_{2-x}La_xCuO_{6+\delta}}$. *arXiv.org*, February 2012.

[9] Frédéric Bourdarot, Elena Hassinger, Stéphane Raymond, Dai Aoki, Valentin Taufour, Louis-Pierre Regnault, and Jacques Flouquet. Precise Study of the Resonance at Q0=(1,0,0) in URu2Si2. *Journal of the Physical Society of Japan*, 79(6):064719, June 2010.

[10] Frédéric Bourdarot, Nicolas Martin, Stéphane Raymond, Louis-Pierre Regnault, Dai Aoki, Valentin Taufour, and Jacques Flouquet. Magnetic properties of URu_2Si_2 under uniaxial stress by neutron scattering. *Physical Review B*, 84(18):184430, November 2011.

[11] Frédéric Bourdarot, Stéphane Raymond, and Louis-Pierre Regnault. Neutron scattering studies on URu 2Si 2. *Philosophical Magazine*, 94(32-33):3702–3722, November 2014.

[12] Frédéric Bourdarot, Stéphane Raymond, and Louis-Pierre Regnault. Neutron scattering studies on URu2Si2. *arXiv.org*, July 2014.

[13] C Broholm, H Lin, P T Matthews, T E Mason, WJL Buyers, M F Collins, A A Menovsky, J A Mydosh, and J K Kjems. Magnetic excitations in the heavy-fermion superconductor URu_2Si_2. *Physical Review B*, 43(16):12809, 1991.

[14] C Brouder, C R Natoli, P Sainctavit, and J Goulon. Theory of X-ray natural circular dichroism. *Journal of synchrotron ...*, 1999.

[15] Nicholas P Butch, Michael E Manley, Jason R Jeffries, Marc Janoschek, Kevin Huang, M Brian Maple, Ayman H Said, Bogdan M Leu, and Jeffrey W Lynn. Symmetry and correlations underlying hidden order in URu2Si2. *Physical Review B*, 91(3):035128, January 2015.

[16] Premala Chandra, Piers Coleman, and Rebecca Flint. Hastatic order in the heavy-fermion compound URu2Si2. *Nature*, 493(7434):621–626, January 2013.

[17] Premala Chandra, Piers Coleman, and Rebecca Flint. Hastatic Order in URu2Si2 : Hybridization with a Twist. *arXiv.org*, January 2015.

[18] Premi Chandra, P Coleman, J A Mydosh, and V Tripathi. Hidden orbital order in the heavy fermion metal URu2Si2. *Nature*, 417(6891):831–834, 2002.

[19] Piers Coleman. *Handbook of Magnetism and Advanced Magnetic Materials: Heavy Fermions: electrons at the edge of magnetism*, volume 1. John Wiley and Sons, 2007.

[20] R Comin, A Frano, M M Yee, Y Yoshida, and H Eisaki. Charge order driven by Fermi-arc instability in $Bi_2Sr_{2-x}La_xCuO_{6+\delta}$. *Science*, 2014.

[21] Francesco Cricchio, Fredrik Bultmark, Oscar Grånäs, and Lars Nordström. Itinerant Magnetic Multipole Moments of Rank Five as the Hidden Order in URu2Si2. *Physical Review Letters*, 103(10):107202, September 2009.

[22] Tatsuma D Matsuda, Elena Hassinger, Dai Aoki, Valentin Taufour, Georg Knebel, Naoyuki Tateiwa, Etsuji Yamamoto, Yoshinori Haga, Yoshichika Ōnuki, Zachary Fisk, and Jacques Flouquet. Details of Sample Dependence and Transport Properties of URu 2Si 2. *Journal of the Physical Society of Japan*, 80(11):114710, November 2011.

[23] P Das, R E Baumbach, K Huang, M B Maple, Y Zhao, J S Helton, J W Lynn, E D Bauer, and M Janoschek. Absence of a static in-plane magnetic moment in the 'hidden-order' phase of URu 2Si 2. *New Journal of Physics*, 15(5):053031, May 2013.

[24] S De Almeida-Didry, Y Sidis, V Balédent, F Giovannelli, I Monot-Laffez, and P Bourges. Evidence for intra-unit-cell magnetic order in Bi 2Sr 2CaCu 2O 8+δ. *Physical Review B*, 86(2):020504, July 2012.

[25] A de Visser, F E Kayzel, A A Menovsky, and J J M Franse. Thermal expansion and specific heat of monocrystalline URu2Si2. *Physical Review B*, 34(11):8168–8171, December 1986.

[26] S Di Matteo and M Norman. X-ray dichroism and the pseudogap phase of cuprates. *Physical Review B*, 76(1):014510, July 2007.

[27] V A Belyakov Dmitrienko and V E. Polarization phenomena in x-ray optics. *Sov. Phys. Usp*, 32(8):697, August 1989.

[28] Yonatan Dubi and Alexander V Balatsky. Hybridization Wave as the "Hidden Order" in URu2Si2. *Physical Review Letters*, 106(8):086401, February 2011.

[29] S Elgazzar, J Rusz, M Amft, P M Oppeneer, and J A Mydosh. Hidden order in URu2Si2 originates from Fermi surface gapping induced by dynamic symmetry breaking. *Nature Materials*, 8(4):337–341, February 2009.

[30] B Fauqué, Y Sidis, V Hinkov, S Pailhès, C T Lin, X Chaud, and P Bourges. Magnetic Order in the Pseudogap Phase of High-T$_C$ Superconductors. *Physical Review Letters*, 96(19):197001, May 2006.

[31] Rebecca Flint, Premala Chandra, and Piers Coleman. Hidden and Hastatic Orders in URu2Si2. *arXiv.org*, March 2014.

[32] Alexander D Fried. Relationship of time-reversal symmetry breaking to optical Kerr rotation. *Physical Review B*, 90(12):121112, 2014.

[33] J Goulon, Ch Goulon-Ginet, A Rogalev, V Gotte, Ch Brouder, and C Malgrange. X-ray dichroism in biaxial gyrotropic media: Differential absorption and fluorescence excitation spectra. *The European Physical Journal B-Condensed Matter and Complex Systems*, 12(3):373–385, 1999.

[34] J Goulon, A Rogalev, and C Gauthier. Instrumentation developments for X-ray linear and circular dichroism at the ESRF beamline ID12A. *Journal of synchrotron ...*, 1998.

[35] José Goulon, Chantal Goulon-Ginet, Andrei Rogalev, Gisele Benayoun, Christian Brouder, and Calogero R Natoli. X-ray natural circular dichroism and chiral-EXAFS in gyrotropic crystals. *Journal of synchrotron radiation*, 7(3):182–188, 2000.

[36] José Goulon, Chantal Goulon-Ginet, Andrei Rogalev, Vincent Gotte, Cécile Malgrange, Christian Brouder, and Calogero R Natoli. X-ray natural circular dichroism in a uniaxial gyrotropic single crystal of LiIO3. *The Journal of Chemical Physics*, 108(15):6394, 1998.

[37] Giuseppe Grosso and Giuseppe Patori Parravicini. *Solid State Physics.* Academic Press, 2000.

[38] E Hassinger, G Knebel, K Izawa, P Lejay, B Salce, and J Flouquet. Temperature-pressure phase diagram of URu2Si2 from resistivity measurements and ac calorimetry: Hidden order and Fermi-surface nesting. *Physical Review B*, 77(11):115117, March 2008.

[39] E Hassinger, G Knebel, T D Matsuda, Dai Aoki, V Taufour, and Jacques Flouquet. Similarity of the Fermi Surface in the Hidden Order State and in the Antiferromagnetic State of URu_2Si_2. *Physical Review Letters*, 105(21):216409, 2010.

[40] Kristjan Haule and Gabriel Kotliar. Arrested Kondo effect and hidden order in URu2Si2. *Nature Physics*, 5(11):796–799, September 2009.

[41] R H He, M Hashimoto, H Karapetyan, J D Koralek, J P Hinton, J P Testaud, V Nathan, Y Yoshida, H Yao, K Tanaka, W Meevasana, R G Moore, D H Lu, S K Mo, M Ishikado, H Eisaki, Z Hussain, T P Devereaux, S A Kivelson, J Orenstein, A Kapitulnik, and Z X Shen. From a Single-Band Metal to a High-Temperature Superconductor via Two Thermal Phase Transitions. *Science*, 331(6024):1579–1583, March 2011.

[42] Keiichi Hirano, Tetsuya Ishikawa, and Seishi Kikuta. Perfect crystal X-ray phase retarders. *Nuclear Instruments and Methods in Physics Research Section A: Accelerators, Spectrometers, Detectors and Associated Equipment*, 336(1):343–353, 1993.

[43] Keiichi Hirano, Tetsuya Ishikawa, Satoshi Koreeda, Katsuhiro Fuchigami, Kiyoshi Kanzaki, and Seishi Kikuta. Switching of photon helicities in the hard X-ray region with a perfect crystal phase retarder. *Japanese journal of applied physics*, 31(8B):L1209, 1992.

[44] Keiichi Hirano, Koichi Izumi, Tetsuya Ishikawa, Shoichi Annaka, and Seishi Kikuta. An X-ray phase plate using Bragg-case diffraction. *Japanese journal of applied physics*, 30(3A):L407, 1991.

[45] M Hofmann, T Lorenz, K Berggold, M Grüninger, A Freimuth, G S Uhrig, and E Brück. Evidence for a large magnetic heat current in insulating layered cuprates. *Physical Review B*, 67(18):184502, May 2003.

[46] P Hosur, A Kapitulnik, S A Kivelson, and J Orenstein. Erratum: Kerr effect as evidence of gyrotropic order in the cuprates [Phys. Rev. B 87, 115116 (2013)]. *Physical Review B*, 2015.

[47] Pavan Hosur, A Kapitulnik, S A Kivelson, J Orenstein, and S Raghu. Kerr effect as evidence of gyrotropic order in the cuprates. *Physical Review B*, 87(11):115116, March 2013.

[48] Hiroaki Ikeda, Michi-To Suzuki, Ryotaro Arita, Tetsuya Takimoto, Takasada Shibauchi, and Yuji Matsuda. Emergent rank-5 nematic order in URu2Si2. *Nature Physics*, 8(7):528–533, June 2012.

[49] J A Janik, H D Zhou, Y J Jo, L Balicas, G J MacDougall, G M Luke, J D Garrett, K J McClellan, E D Bauer, and J L Sarrao. Itinerant spin excitations near the hidden order transition in URu2Si2. *Journal of Physics: Condensed Matter*, 21(19):192202, 2009.

[50] S Kambe, Y Tokunaga, H Sakai, T D Matsuda, Y Haga, Z Fisk, and R E Walstedt. NMR Study of In-Plane Twofold Ordering in URu_2Si_2. *Physical Review Letters*, 110(24):246406, June 2013.

[51] Aharon Kapitulnik. Notes on constraints for the observation of Polar Kerr Effect in complex materials. *Physica B: Condensed Matter*, 460(C):151–158, March 2015.

[52] N Kernavanois, P Dalmas de Réotier, A Yaouanc, J-P Sanchez, K D Liß, and P Lejay. Investigation of the crystal structure of URu 2 Si 2 by high-resolution X-ray diffraction. *Physica B: Condensed Matter*, 259:648–649, 1999.

[53] Annamária Kiss and Patrik Fazekas. Group theory and octupolar order in URu2Si2. *Physical Review B*, 71(5):054415, February 2005.

[54] Masato Kubota, Kanta Ono, Yasuaki Oohara, and Hiroshi Eisaki. X-ray Optical Activity in Underdoped Bi-Based High- TcSuperconductor. *Journal of the Physical Society of Japan*, 75(5):053706, May 2006.

[55] H H Kung, R E Baumbach, E D Bauer, V K Thorsmolle, W L Zhang, K Haule, J A Mydosh, and G Blumberg. Chirality density wave of the "hidden order" phase in URu2Si2. *Science*, 347(6228):1339–1342, March 2015.

[56] Hiroaki Kusunose and Hisatomo Harima. On the Hidden Order in URu_2Si_2 – Antiferro Hexadecapole Order and Its Consequences. *Journal of the Physical Society of Japan*, 80(8):084702, July 2011.

[57] M Le Tacon, A Bosak, S M Souliou, G Dellea, T Loew, R Heid, K P Bohnen, G Ghiringhelli, M Krisch, and B Keimer. Inelastic X-ray scattering in YBa2Cu3O6. 6 reveals giant phonon anomalies and elastic central peak due to charge-density-wave formation. *Nature Physics*, 10(1):52–58, 2014.

[58] Patrick A Lee, Naoto Nagaosa, and Xiao-Gang Wen. Doping a Mott insulator: Physics of high-temperature superconductivity. *Reviews of Modern Physics*, 78(1):17–85, January 2006.

[59] Y Li, V Balédent, N Barišić, Y Cho, B Fauqué, Y Sidis, G Yu, X Zhao, P Bourges, and M Greven. Unusual magnetic order in the pseudogap region of the superconductor HgBa2CuO4+δ. *Nature*, 455(7211):372–375, September 2008.

[60] Stephen W. Lovesey. *Theory of Neutron Scattering from Condensed Matter.* Oxford Science Publications, 1986.

[61] Y Lubashevsky, LiDong Pan, T Kirzhner, G Koren, and N P Armitage. Optical Birefringence and Dichroism of Cuprate Superconductors in the THz Regime. *Physical Review Letters*, 112(14):147001, April 2014.

[62] V Madhavan. Tunneling into a Single Magnetic Atom: Spectroscopic Evidence of the Kondo Resonance. *Science*, 280(5363):567–569, April 1998.

[63] M B Maple, J W Chen, Y Dalichaouch, T Kohara, C Rossel, M S Torikachvili, M W McElfresh, and J D Thompson. Partially gapped Fermi surface in the heavy-electron superconductor URu 2 Si 2. *Physical Review Letters*, 56(2):185, 1986.

[64] A A Maradudin and A E Fein. Scattering of neutrons by an anharmonic crystal. *Physical Review*, 128(6):2589, 1962.

[65] Ivan Marri and Paolo Carra. Scattering operators for E1-E2 x-ray resonant diffraction. *Physical Review B*, 69(11):113101, March 2004.

[66] Yoshiharu Matsuoka, Takayuki Kawamata, Koki Naruse, Masumi Ohno, Yoichi Nishiwaki, Tetsuya Kato, Takahiko Sasaki, and Yoji Koike. Observation of the Thermal Conductivity due to Spins in the One-Dimensional Antiferromagnetic Ising-Like Spin System ACo X3(A= Rb, Cs; X= Cl, Br). *Journal of the Physical Society of Japan*, 83(6):064603, June 2014.

[67] Jian-Qiao Meng, Peter M Oppeneer, John A Mydosh, Peter S Riseborough, Krzysztof Gofryk, John J Joyce, Eric D Bauer, Yinwan Li, and Tomasz Durakiewicz. Imaging the Three-Dimensional Fermi-Surface Pairing near the

Hidden-Order Transition in URu_2Si_2 Using Angle-Resolved Photoemission Spectroscopy. *Physical Review Letters*, 111(12):127002, September 2013.

[68] V P Mineev and M E Zhitomirsky. Interplay between spin-density wave and induced local moments in URu2Si2. *Physical Review B*, 72(1):014432, July 2005.

[69] Takeshi Mito, Midori Hattori, Gaku Motoyama, Yoshio Sakai, Takehide Koyama, Koichi Ueda, Takao Kohara, Makoto Yokoyama, and Hiroshi Amitsuka. Investigation of Local Symmetries in the Hidden-Order Phase of URu 2Si 2. *Journal of the Physical Society of Japan*, 82(12):123704, December 2013.

[70] J A Mydosh and P M Oppeneer. Colloquium: Hidden order, superconductivity, and magnetism: The unsolved case of URu_2Si_2. *Reviews of Modern Physics*, 83(4):1301–1322, November 2011.

[71] J A Mydosh and P M Oppeneer. Hidden order behaviour in URu 2Si 2(A critical review of the status of hidden order in 2014). *Philosophical Magazine*, 94(32-33):3642–3662, November 2014.

[72] C R Natoli, C Brouder, P Sainctavit, J Goulon, C Goulon-Ginet, and A Rogalev. Calculation of X-ray natural circular dichroism. *The European Physical Journal B-Condensed Matter and Complex Systems*, 4(1):1–11, July 1998.

[73] P G Niklowitz, C Pfleiderer, T Keller, M Vojta, Y-K Huang, and J A Mydosh. Parasitic Small-Moment Antiferromagnetism and Nonlinear Coupling of Hidden Order and Antiferromagnetism in URu_2Si_2 Observed by Larmor Diffraction. *Physical Review Letters*, 104(10):106406, 2010.

[74] M R Norman. X-ray natural dichroism and chiral order in underdoped cuprates. *Physical Review B*, 87(18):180506, May 2013.

[75] R Okazaki, T Shibauchi, H J Shi, Y Haga, T D Matsuda, E Yamamoto, Y Onuki, H Ikeda, and Y Matsuda. Rotational Symmetry Breaking in the Hidden-Order Phase of URu2Si2. *Science*, 331(6016):439–442, January 2011.

[76] P M Oppeneer, J Rusz, S Elgazzar, M T Suzuki, T Durakiewicz, and J A Mydosh. Electronic structure theory of the hidden-order material URu_2Si_2. *Physical Review B*, 82(20):205103, November 2010.

[77] TTM Palstra, A A Menovsky, J van den Berg, A J Dirkmaat, P H Kes, G J Nieuwenhuys, and J A Mydosh. Superconducting and Magnetic Transitions in the Heavy-Fermion System URu_2Si_2. *Physical Review Letters*, 55(24):2727–2730, 1985.

[78] TTM Palstra, A A Menovsky, and J A Mydosh. Anisotropic electrical resistivity of the magnetic heavy-fermion superconductor URu 2 Si 2. *Physical Review B*, 33(9):6527, 1986.

[79] Judy Pang, William Buyers, Aleksandr Chernatynskiy, Mark Lumsden, Bennett Larson, and Simon Phillpot. Phonon Lifetime Investigation of Anharmonicity and Thermal Conductivity of UO2 by Neutron Scattering and Theory. *Physical Review Letters*, 110(15):157401, April 2013.

[80] W K Park, S M Narasiwodeyar, E D Bauer, P H Tobash, R E Baumbach, F Ronning, J L Sarrao, J D Thompson, and L H Greene. Hidden order and hybridization gap in URu2Si2 via quasiparticle scattering spectroscopy. *Philosophical Magazine*, 94(32-33):3737–3746, November 2014.

[81] W K Park, P H Tobash, F Ronning, E D Bauer, J L Sarrao, J D Thompson, and L H Greene. Observation of the Hybridization Gap and Fano Resonance in the Kondo Lattice $\mathrm{URu_2Si_2}$. *Physical Review Letters*, 108(24):246403, June 2012.

[82] Robert D Peacock and Brian Stewart. Natural Circular Dichroism in X-ray Spectroscopy. *The Journal of Physical Chemistry B*, 105(2):351–360, January 2001.

[83] C Pépin, M R Norman, S Burdin, and A Ferraz. Modulated Spin Liquid: A New Paradigm for URu2Si2. *Physical Review Letters*, 106(10):106601, March 2011.

[84] Alexandre Pourret, Alexandra Palacio-Morales, Steffen Kramer, Liam Malone, Marc Nardone, Dai Aoki, Georg Knebel, and Jacques Flouquet. Fermi Surface Reconstruction inside the Hidden Order Phase of URu2Si2 Probed by Thermoelectric Measurements. *Journal of the Physical Society of Japan*, 82(3):034706, March 2013.

[85] E Ressouche, R Ballou, F Bourdarot, D Aoki, V Simonet, M T Fernandez-Diaz, A Stunault, and J Flouquet. Hidden Order in $\mathrm{URu_2Si_2}$ Unveiled. *Physical Review Letters*, 109(6):067202, August 2012.

[86] Peter S. Riseborough. Advanced quantum mechanics. https://math.temple.edu/ prisebor/Advanced.pdf.

[87] K A Ross, L Harriger, Z Yamani, W J L Buyers, J D Garrett, A A Menovsky, J A Mydosh, and C L Broholm. Strict limit on in-plane ordered magnetic dipole moment in URu2Si2. *Physical Review B*, 89(15):155122, April 2014.

[88] J. J. Sakurai. *Modern Quantum Mechanics.* Addison Wesley Longman, 1994.

[89] Andrés F Santander-Syro, Markus Klein, Florin L Boariu, Andreas Nuber, Pascal Lejay, and Friedrich Reinert. Fermi-surface instability at the 'hidden-order' transition of URu2Si2. *Nature Physics*, 5(9):637–641, July 2009.

[90] A R Schmidt, M H Hamidian, P Wahl, F Meier, A V Balatsky, J D Garrett, T J Williams, G M Luke, and J C Davis. Imaging the Fano lattice to 'hidden order' transition in URu2Si2. *Nature*, 465(7298):570–576, March 2010.

[91] G Schütz, W Wagner, W Wilhelm, P Kienle, R Zeller, R Frahm, and G Materlik. Absorption of circularly polarized x rays in iron. *Physical Review Letters*, 58(7):737, 1987.

[92] P Sharma, N Harrison, M Jaime, Y Oh, K Kim, C Batista, H Amitsuka, and J Mydosh. Phonon Thermal Transport of URu2Si2: Broken Translational Symmetry and Strong-Coupling of the "Hidden Order" to the Lattice. *Physical Review Letters*, 97(15):156401, October 2006.

[93] Gen Shirane, Stephen M. Shapiro, and John M. Tranquada. *Neutron Scattering with a Triple-Axis Spectrometer: Basic Techniques.* Cambridge University Press, 2002.

[94] G. L. Squires. *Introduction to the Theory of Thermal Neutron Scattering.* Cambridge University Press, 3 edition, 2012.

[95] J. Stöhr and H.C. Siegmann. *Magnetism.* Springer, 2006.

[96] M B Stone, M D Lumsden, S E Nagler, D J Singh, J He, B C Sales, and D Mandrus. Quasi-One-Dimensional Magnons in an Intermetallic Marcasite. *Physical Review Letters*, 108(16):167202, April 2012.

[97] C Tabata, T Inami, S Michimura, M Yokoyama, H Hidaka, T Yanagisawa, and H Amitsuka. X-ray backscattering study of crystal lattice distortion in hidden order of URu 2Si 2. *Philosophical Magazine*, 94(32-33):3691–3701, November 2014.

[98] T S Toellner, A Alatas, and A H Said. Six-reflection meV-monochromator for synchrotron radiation. *J. Synchrotron Rad (2011). 18, 605-611 [doi:10.1107/S0909049511017535]*, pages 1–7, May 2011.

[99] W H Toews, Songtian S Zhang, K A Ross, H A Dabkowska, B D Gaulin, and R W Hill. Thermal Conductivity of $Ho_2Ti_2O_7$ along the [111] Direction. *Physical Review Letters*, 110(21):217209, May 2013.

[100] S Tonegawa, K Hashimoto, K Ikada, Y H Lin, H Shishido, Y Haga, T D Matsuda, E Yamamoto, Y Onuki, H Ikeda, Y Matsuda, and T Shibauchi. Cyclotron Resonance in the Hidden-Order Phase of URu_2Si_2. *Physical Review Letters*, 109(3):036401, July 2012.

[101] S Tonegawa, K Hashimoto, K Ikada, Y Tsuruhara, Y H Lin, H Shishido, Y Haga, T D Matsuda, E Yamamoto, and Y Onuki. Cyclotron resonance study of quasiparticle mass and scattering rate in the hidden-order and superconducting phases of URu 2 Si 2. *Physical Review B*, 88(24):245131, 2013.

[102] S Tonegawa, S Kasahara, T Fukuda, K Sugimoto, N Yasuda, Y Tsuruhara, D Watanabe, Y Mizukami, Y Haga, T D Matsuda, E Yamamoto, Y Onuki, H Ikeda, Y Matsuda, and T Shibauchi. Direct observation of lattice symmetry

breaking at the hidden-order transition in URu2Si2. *Nature Communications*, 5:1–7, June 2014.

[103] C M Varma and Lijun Zhu. Helicity Order: Hidden Order Parameter in URu2Si2. *Physical Review Letters*, 96(3):036405, January 2006.

[104] A Villaume, F Bourdarot, E Hassinger, S Raymond, V Taufour, D Aoki, and J Flouquet. Signature of hidden order in heavy fermion superconductor URu2Si2: Resonance at the wave vector Q0=(1,0,0). *Physical Review B*, 78(1):012504, July 2008.

[105] C Wiebe, G Luke, Z Yamani, A Menovsky, and W Buyers. Search for hidden orbital currents and observation of an activated ring of magnetic scattering in the heavy fermion superconductor URu2Si2. *Physical Review B*, 69(13):132418, April 2004.

[106] C R Wiebe, J A Janik, G J MacDougall, G M Luke, J D Garrett, H D Zhou, Y J Jo, L Balicas, Y Qiu, J R D Copley, Z Yamani, and W J L Buyers. Gapped itinerant spin excitations account for missing entropy in the hidden-order state of URu2Si2. *Nature Physics*, 3(2):96–99, January 2007.

[107] T J Williams, Z Yamani, N P Butch, G M Luke, M B Maple, and W J L Buyers. Neutron scattering study of $URu_{2x}Re_xSi_2$ (x=0.10): Driving order towards quantum criticality. *Physical Review B*, 86(23):235104, December 2012.

[108] W D Wise, M C Boyer, Kamalesh Chatterjee, Takeshi Kondo, T Takeuchi, H Ikuta, Yayu Wang, and E W Hudson. Charge-density-wave origin of cuprate checkerboard visualized by scanning tunnelling microscopy. *Nature Physics*, 4(9):696–699, 2008.

[109] B Wolf, W Sixl, R Graf, D Finsterbusch, G Bruls, B L thi, E A Knetsch, A A Menovsky, and J A Mydosh. Elastic properties of the heavy fermion superconductor URu2Si2. *Journal of Low Temperature Physics*, 94(3-4):307–324, February 1994.

[110] T Yanagisawa, S Mombetsu, H Hidaka, H Amitsuka, M Akatsu, S Yasin, S Zherlitsyn, J Wosnitza, K Huang, M Janoschek, and M B Maple. Hybridization-driven orthorhombic lattice instability in URu_2Si_2. *Physical Review B*, 88(19):195150, November 2013.

[111] T Yanagisawa, H Saito, Y Watanabe, Y Shimizu, H Hidaka, and H Amitsuka. A Study of Elastic Properties of URu 2Si 2in Comparison with the Non-5 fContribution of ThRu 2Si 2. *Journal of Physics: Conference Series*, 391:012079, December 2012.

[112] Tatsuya Yanagisawa. Ultrasonic study of the hidden order and heavy-fermion state in URu 2Si 2with hydrostatic pressure, Rh-doping, and high magnetic fields. *Philosophical Magazine*, 94(32-33):3775–3788, November 2014.

[113] Tatsuya Yanagisawa, Shota Mombetsu, Hiroyuki Hidaka, Hiroshi Amitsuka, Mitsuhiro Akatsu, Shadi Yasin, Sergei Zherlitsyn, Jochen Wosnitza, Kevin Huang, and M Brian Maple. Γ_3-Type Lattice Instability and the Hidden Order of URu_2Si_2. *Journal of the Physical Society of Japan*, 82(1):013601, December 2012.

[114] Z Y Zhao, X M Wang, C Fan, W Tao, X G Liu, W P Ke, F B Zhang, X Zhao, and X F Sun. Magnetic phase transitions and magnetoelectric coupling of $GdFeO_3$ single crystals probed by low-temperature heat transport. *Physical Review B*, 83(1):014414, January 2011.